# High quality 4H-SiC crystal growth and dislocations behavior during solution method

**Xiao Shiyu**

## Contents

**Chapter 1 Introduction .......... 1**

1.1 Green power devices .......... 1
1.2 Power semiconductor devices .......... 1
1.3 Materials for power devices .......... 3
1.4 Properties of SiC .......... 6
1.4.1 SiC structure and their polytypism .......... 6
1.4.2 Polarity of Si face and C face .......... 9
1.4.3 SiC power devices .......... 10
1.5 Growth of SiC single crystal .......... 12
1.5.1 Sublimation recrystallization method .......... 13
1.5.2 Modified physical vapor transport method (M-PVT) .......... 14
1.5.3 Chemical vapor deposition (CVD) .......... 15
1.5.4 Solution growth .......... 15
1.6 Dislocations in SiC .......... 17
1.6.1 Threading screw dislocation .......... 18
1.6.2 Threading edge dislocation .......... 19
1.6.3 Basal plane dislocation .......... 20
1.6.4 Frank-type partial dislocation .......... 21
1.6.5 Dislocations' influence on power device and reduction .......... 21
1.7 Dislocations behavior during solution growth .......... 22
1.8 High-quality SiC solution growth .......... 25
1.8.1 Solvent composition .......... 25
1.8.2 Polytype stability .......... 26
1.8.3 The reduction of dislocations .......... 27
1.9 Objective and contents of this study .......... 29
**Reference** .......... 31

**Chapter 2 SiC growth by TSSG method .......... 38**

2.1 Introduction .......... 38
2.2 The driving force of solution growth .......... 38
2.3 Growth model .......... 40

2.3.1 Spiral growth ........................................ 41
2.3.2 2D nucleation ........................................ 42
2.4 Experiment ........................................ 43
2.4.1 SiC Growth apparatus ........................................ 43
2.4.2 Materials ........................................ 45
2.4.2.1 Raw materials ........................................ 45
2.4.2.2 Crucible, rod and seed crystal ........................................ 46
2.4.2.3 Thermal isolation materials ........................................ 49
2.4.2.4 Atmosphere ........................................ 49
2.4.3 Temperature distribution measurement ........................................ 49
2.4.4 Preparation before growth ........................................ 50
2.4.4.1 Clean of raw materials ........................................ 50
2.4.4.2 Baking crucible ........................................ 50
2.4.4.3 The bonding method between seed and rod ........................................ 51
2.4.5 Growth procedure ........................................ 53
2.4.6 Process after growth ........................................ 53
2.4.6.1 Removing residual Si solvent ........................................ 53
2.4.6.2 Removing rod ........................................ 53
2.4.6.3 Crystal cutting and polish ........................................ 53
2.4.7 Characterization ........................................ 53
2.4.7.1 Differential interference (DIC) contrast microscopy ........................................ 54
2.4.7.2 Confocal laser scanning microscopy ........................................ 54
2.4.7.3 Raman spectroscopy ........................................ 55
2.4.7.4 Molten KOH etching ........................................ 56
2.4.7.5 Synchrotron X-ray topography ........................................ 56
2.4.7.6 Transmission Electronic Microscopy ........................................ 58
2.4.7.7 Scanning transmission electron microscopy ........................................ 59
2.5 Conclusion ........................................ 60
**Reference** ........................................ 61

**Chapter 3 V-shaped defects during 4H-SiC solution growth ........................................ 63**

3.1 Introduction ........................................ 63
3.2 Experiment ........................................ 64
3.2.1 Growth ........................................ 64
3.2.2 Characterization ........................................ 65
3.3 Results and discussion ........................................ 65

3.3.1 V-shaped generated defects ... 66
3.3.2 The Burgers vector of V-shaped defects ... 68
3.3.3 Microstructure of V-shaped defects ... 69
3.3.4 Generated mechanism ... 72
3.4 Conclusion ... 74
**Reference** ... 76

**Chapter 4 TSD conversion behavior on C-face growth ... 78**

4.1 Introduction ... 78
4.2 Experiment ... 78
4.2.1 Growth ... 78
4.2.2 Characterization ... 79
4.3 Results and discussion ... 80
4.3.1 Morphology ... 81
4.3.2 The realization of TSD conversion on C face growth ... 82
4.3.3 Characterization of step structure ... 85
4.3.4 The effect of step structure on TSD conversion ratio ... 86
4.3.5 Partial dislocations in crystal grown from Si-5at%Ti solvent ... 88
4.4 Conclusion ... 92
**Reference** ... 93

**Chapter 5 Increase TSD conversion ratio on C face growth ... 94**

5.1 Introduction ... 94
5.2 Experiment ... 94
5.2.1 Growth ... 94
5.2.2 Characterization ... 95
5.3 Blurred topography images ... 95
5.3.1 The effect of growth time on topography images on C face growth crystal with Si-5at%Ti solvent ... 95
5.3.2 The effect of holding seed method on topography images on C face growth crystal with Si-5at%Ti solvent ... 98
5.4 Reduction of $N_2$ doping concentration from background during growth ... 100
5.5 The TSD conversion ratio dependence of growth thickness ... 103
5.6 Conclusion ... 103
**Reference** ... 104

**Chapter 6 High quality 4H-SiC C face grown crystals ... 105**

6.1 Introduction ........ 105
6.2 Two-step growth ........ 105
6.3 Experiment ........ 107
6.3.1 Growth ........ 107
6.3.1.1 First step growth ........ 107
6.3.1.2 Second step growth ........ 107
6.3.2 Characterization ........ 108
6.4 Results and discussion ........ 109
6.4.1 Grown crystal after the first step growth ........ 109
6.4.2 Grown crystal after the second step growth ........ 111
6.5 Conclusion ........ 112
**Reference** ........ 113
**Chapter 7 Conclusion ........ 114**
**Acknowledgment ........ 117**
**Presented papers ........ 118**

# Chapter 1 Introduction

## 1.1 Green power devices

Nowadays, global warming has become one of the serious problems of the world. From the 18th century to present, the rapid development of the industry is always associated with the large consumption of resources, such as the fossil, coal and so on. The discharge of them like $CO_2$ results in greenhouse effect which threatens the survival of lives seriously.[1-1] In order to protect our world and for the future of mankind, it is urgent and necessary to build the low carbon society all over the world. The United Nations Framework Convention on Climate Change (UNFCCC) was built to the convention have met annually in Conferences of the Parties (COP) to assess progress in dealing with climate change.[1-2] The energy saving and emission reduction have been recognized as the most important mission in the whole world.

In order to realize the energy saving society, the power loss and basic charges of power transformer need to be improved. As the environment friendly movement continues to grow in popularity, the demand for green products will increase.[1-3] As technology becomes green so will devices. The new devices need to be both smart and green. Devices will continue to evolve.

## 1.2 Power semiconductor devices

A power semiconductor device is a semiconductor device used as a switch or rectifier in power electronics; a switch-mode power supply is an example. Such a device is also called a power device or when used in an integrated circuit, a power IC.[1-4] Power semiconductor devices are recognized as a key component for all power electronic systems. [1-5]

Transformers are used to increase (or step-up) voltage before transmitting electrical energy over long distances through wires. Wires have resistance which loses energy through joule heating at a rate corresponding to square of the current. By transforming power to a higher voltage transformers enable economical transmission of power and distribution. All but a tiny fraction of the world's electrical power has passed through a series of transformers by the time it reaches the consumer.[1-6] Therefore in order to realize the reduction of power loss and green society, high performance of power devices are

necessary

Four types of transformer are illustrated in Figure 1.1. Choppers are used to transform constant to variable DC or variable to constant DC as shown in Fig. 1.1 (a). In Fig. 1.1 (b), the inverters transform DC to AC of desired voltage and frequency. Meanwhile, rectifiers which transform AC to DC are shown in Fig. 1.1 (c). Fig. 1.1 (d) shows converters converters which transform AC of desired frequency and/or magnitude from generally line AC.[1-7]

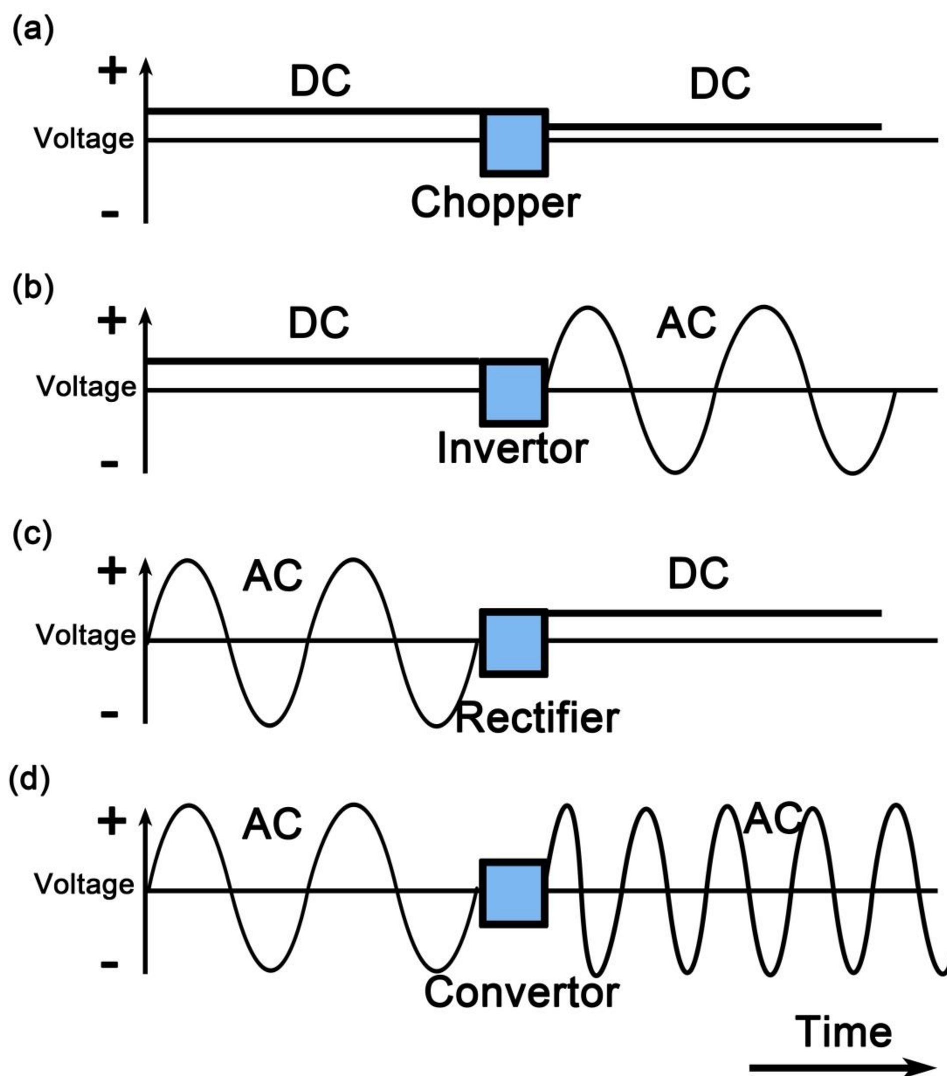


**Fig. 1.1** The illustration of role of each power semiconductor devices: (a) DC/DC regulator; (b) DC/AC invertor; (c) AC/DC rectifier; (d) AC/AC convertor.

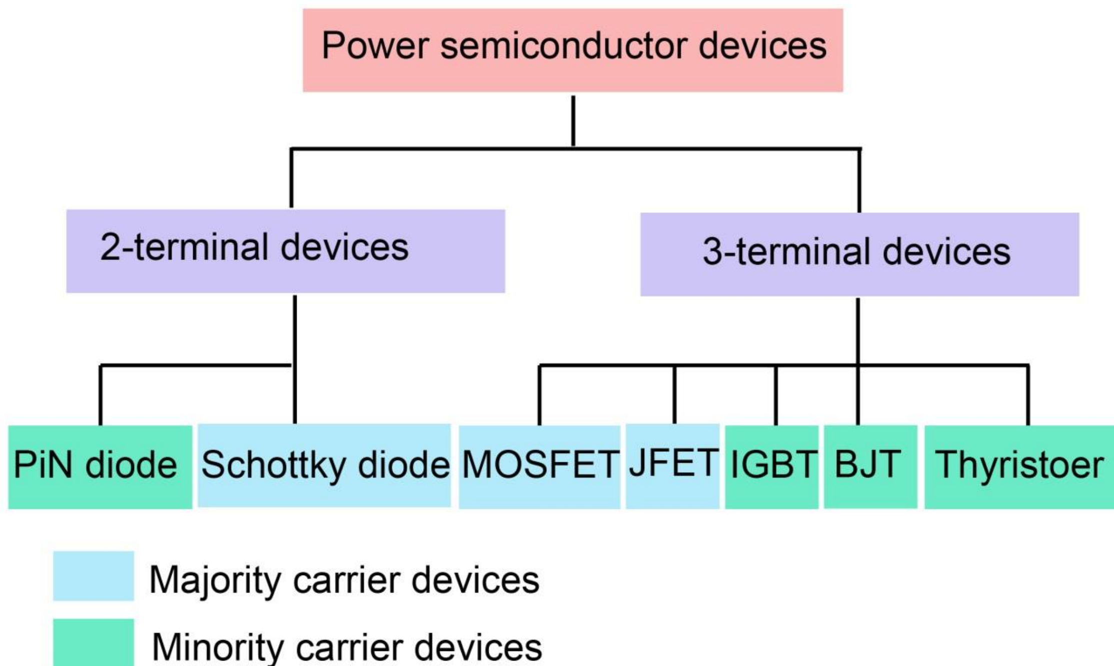


**Fig. 1.2** Classification of power semiconductor devices based on their controllability and other dominant features.

The range of power devices that developed over the last few decades can be represented as a tree as shown in Fig. 1.2 based on their controllability and other dominant features. They can be classified as the following main categories. The first one type is a two-terminal device whose state is completely dependent on the external power circuit to which it is connected. And the other is a three-terminal device whose state is dependent on not only its external power circuit, but also the signal on its driving terminal. Another classification could be based on the device performance: majority carrier devices and minority carrier devices as indicated in different green color.[1-4, 8]

## 1.3 Materials for power devices

Silicon has been widely used as the material for power devices nowadays since the technology of Si single crystal growth such as Czochralski method and Floating Zone method were well developed. Meanwhile, the reduction of dislocation density and co-doping technology has already been realized during Si single crystal growth. [1-9, 10, 11] With the developing of manufacture technology of power devices, the property of Si power devices is greatly improved. However, the Si power device property is thought to be reaching the limit. The physical property of Si is regarded as preventing making

further improvement of power devices properties.

Table 1.1 shows the physical properties of representative semiconductor materials. According to Table 1, the width of band gap of SiC, GaN and diamond is 3 or 5 times larger and the electrical breakdown value is 10-30 times higher than that of Si. [1-12] The wide band gap materials are less influenced to thermal difficulties and usually have high breakdown electric fields which permit for increasing isolation between devices and higher packing densities. [1-13] Thus, the usage of wide band gap materials could realize lower energy loss and higher packing densities at the same time. Meanwhile, the higher saturated electro drift velocity is benefit for increasing switch speed and decreasing switch-loss.

Fig. 1.3 shows the electric field distribution in depletion layer at Schottky diode breakdown of Si and SiC respectively. According to Fig. 1.3 we also could explain the reason why SiC is much more suitable for the high temperature and high frequency power devices than Si. The $E_B$ and $W_M$ indicate the electric field strength and the width of depletion layer respectively. Here the width of depletion layer is the same as the thickness of drift layer. According to equation (1.1), the areas of right-angled triangles are indicted the breakdown voltage $V_B$. [1-14]

$$V_B = \frac{E_B \times W_M}{2} \tag{1.1}$$

As we known, the electrical filed length of SiC is 10 times higher than that of Si. If the power devices which are made from Si and SiC respectively exhibit the same breakdown voltage value, the thickness of drift layer of SiC is 1/10 comparing to Si. Meanwhile, the electrical resistance of the drift layer could be reduced to 1/300-1/500 if the SiC is used instead of Si. Therefore, SiC can reduce energy loss and reduce drift layer thickness obviously comparing to Si.

According to Table 1, the width of band gap and the electric field strength of GaN are similar with that of SiC. Thus, the GaN is also suitable for making the next generation power devices. The Halide vapor phase epitaxy (HVPE) and growth in solution (Ammonothermal) of GaN single crystals are well developed. [1-15] The GaN growth from melt cannot be realized due to its high equilibrium vapor pressure.

The physical property of diamond is extraordinary and has big difference with others. However, comparing to other semiconductor materials it is relatively difficulty to grow diamond single crystal. In nowadays market, the biggest diamond is 1-inch. [1-16]

**Table. 1.1 The physical properties of Si, 4H-SiC, Diamond and GaN**[1-13]

| | Si | 4H-SiC | Diamond | GaN |
|---|---|---|---|---|
| Bandgap (eV) | 1.12 | 3.26 | 5.47 | 3.39 |
| $E_B$ (MV/cm) | 0.3 | 2.5 | 10 | 3.3 |
| $\mu_e$ ($cm^2$/Vs) | 1400 | 1000/850 | 2200 | 900 |
| Saturated electron drift velocity ($\times 10^7$ cm/s) | 1.0 | 2.2 | 2.7 | 2.7 |
| Permittivity | 11.8 | 9.7 | 5.5 | 9 |
| Thermal conductivity (W/cm·K) | 1.5 | 4.9 | 20 | 2.0 |

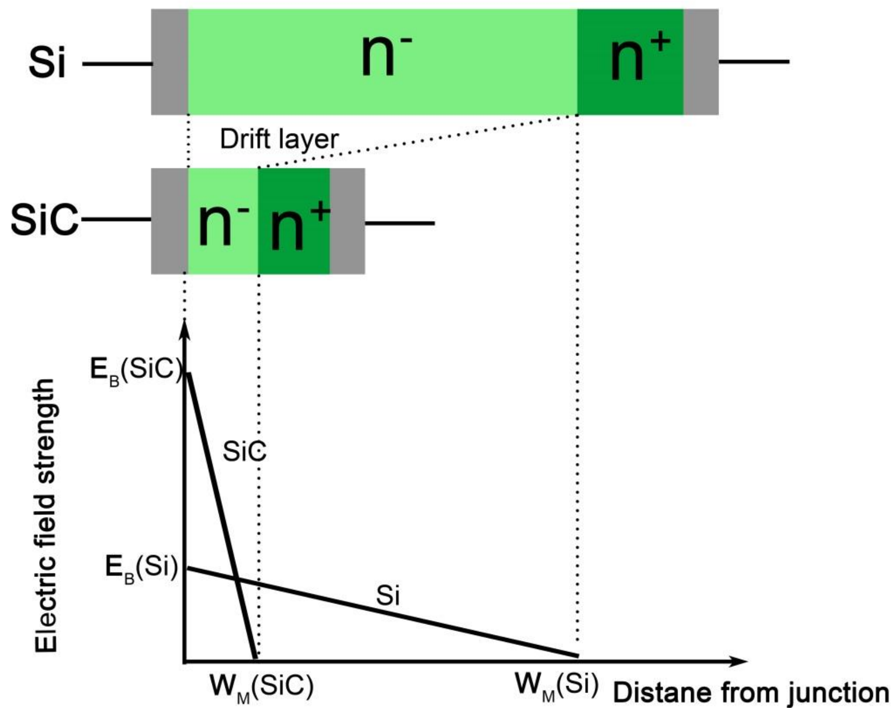


**Fig. 1.3** Electric field distribution in depleted layer of Si and SiC Schottky barrier diode (SBD) at the time of breakdown. The electrical filed length of SiC is 10 times higher than that of Si. If the power devices which are made from Si and SiC respectively exhibit the same breakdown voltage value, the thickness of drift layer of SiC should be 1/10 comparing to Si. Meanwhile, the electrical resistance of the drift layer could be reduced to 1/300-1/500 when the SiC is used instead of Si.[1-14]

## 1.4 Properties of SiC

Based on the discussion above, we know that the SiC power devices could largely decrease energy loss in many fields like the green vehicles. In the green light field, SiC is the best choice for LED due to its low lattice mismatch rate.

### 1.4.1 SiC structure and their polytypism

SiC is binary compound semiconductor which belongs to IV- IV group element. The fundamental structural unit of silicon carbide is a covalently bonded primary co-ordinated tetrahedron as shown in Fig. 1.4. They can be written as either $SiC_4$ or $CSi_4$, Si: C= 1: 1. The bond length between C atoms and neighbors Si atoms is 1.89 Å while the bond length between neighbors C atoms is about 3.08 Å. The length of each bond corresponds to the tetrahedron. The four bonds directed to the neighbors have a nearly purely covalent character. On the other hand, since the C atoms exhibit stronger electronegativity, the Si-C bond exhibits a covalent contribution to the bond of about 88% and an ionic contribution to the bond of about 12%. These can be estimated from Pauling's formula. [1-17]

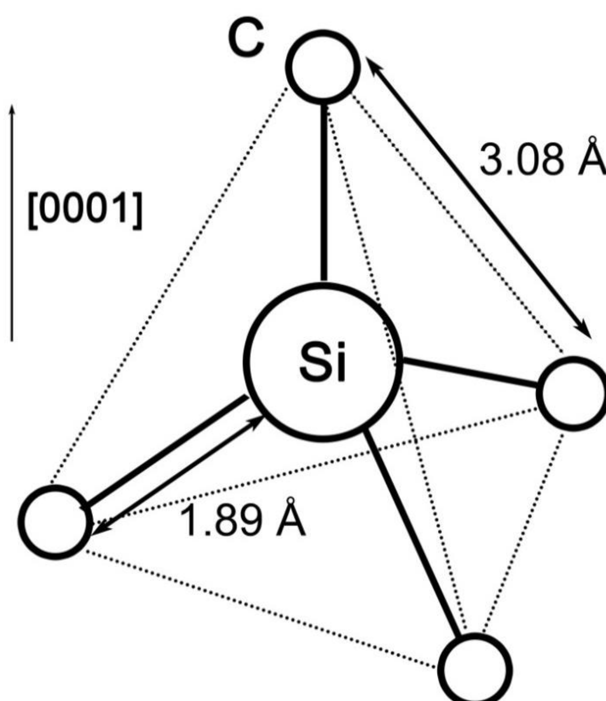


**Fig. 1.4** The fundamental structural unit of SiC structure: the illustration Si-C tetrahedral structure.

Si and C atoms are arranged at the lattice points of the close-packed hexagonal structure (hcp) at the same basal planes. The close-packed atom planes of Si and C atoms stack to each other alternatively along c axis. Each C atom on the same C close-packed plane is bonded with 3 Si atoms on the neighboring Si close-packed plane. Similarly，each Si atom on the same Si close-packed plane is bonded with 3 C atoms on the neighboring C close-packed plane along c axis. The Si atom close-packed layer and neighboring C atom close-packed layer constitute bilayer structure. The distance between them is 0.25 nm. If we regard the Si-C bilayer as a unit, there should be 3 types of stacking sequences along c-axis depending on the stacking positions. [1-17] The 3 kinds of stacking position are shown as Fig. 1.5. Here we named them as A, B and C respectively. According to Fig. 1.5, there are two kinds of stacking positions shown as B and C above A. Similarly, two types of stacking sequences C and A are above the B positions.

The arbitrary permutation and combination of these 3 kinds of stacking sequences could result the polytypism of SiC crystal. There are over 200 SiC polytypes existing. Among them, 3C-, 4H-, 6H- and 2H-SiC are the most commonly available today. The C corresponds to cubic and the H represents to hexagonal. The numbers before the capitals are represent the number of Si-C bilayer per unit cell. For example, there are 3 and 4 bilayers in one unit cell in 3C-SiC and 4H-SiC crystal respectively. The stacking sequence of 2H-, 3C-, 4H- and 6H-SiC are indicated in Fig. 1.6. [1-18, 19] For 2H-SiC, the stacking sequence is as ABABAB…and for 3C-SiC, the stacking sequence is ABCABC…. In 4H-SiC, the stacking sequence is ABCBABCB…. For 6H-SiC, the stacking sequence is ABCACBABC…. Each SiC polytype exhibits different properties such as electrical, optical and thermal properties due to their different stacking sequence. The differences between them are summarized in table 1.2.

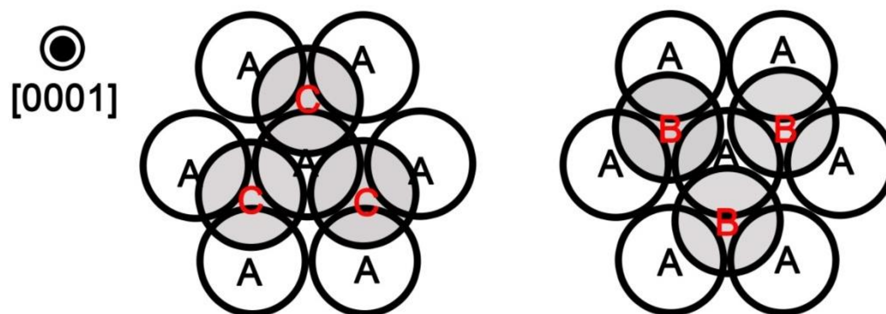


**Fig. 1.5** The arrangement in close-packed structure. There are 3 types of stacking sites A, B, C respectively.

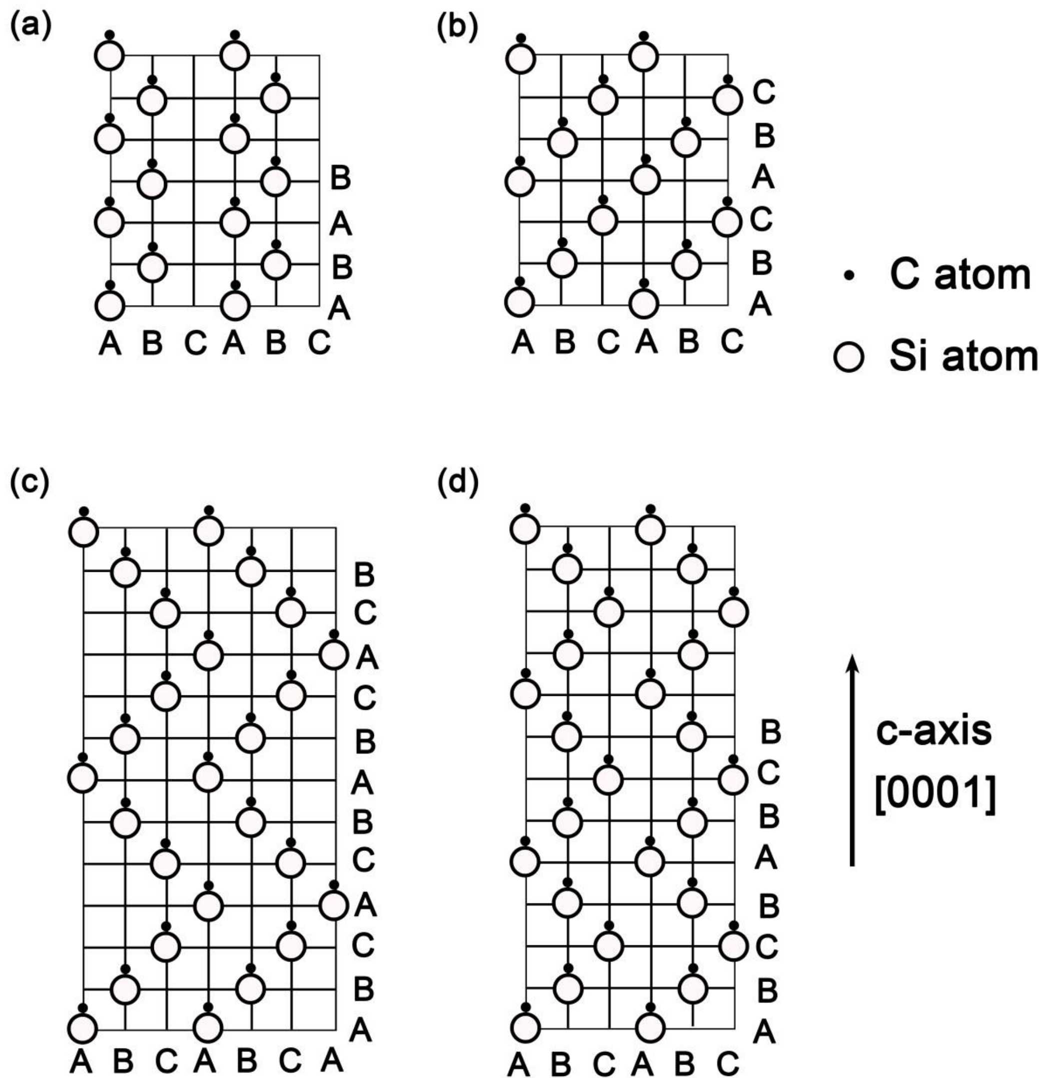


**Fig. 1.6** The illustration of stacking sequence of Si-C bilayers along c-axis of common SiC polytype (a) 2H-SiC (b) 3C-SiC (c) 6H-SiC and (d) 4H-SiC.

**Table 1.2 Physical parameters of some polytypes of SiC crystals** [1-20]

| | 3C-SiC | 4H-SiC | 6H-SiC |
|---|---|---|---|
| Energy gap (eV) | 2.23 | 3.26 | 3.02 |
| Electron field ($MVcm^{-1}$) | 1.5 | 2.0 | 2.4 |
| Electron velocity ($cm^2V^{-1}S^{-1}$) | 1000 | 720 (⊥c)<br>650 (//c) | 370(⊥c)<br>50(//c) |

## 1.4.2 Polarity of Si face and C face

Moreover, since the stacking of Si-C bilayers constitutes the crystal there are always two faces exist. The face which is terminated by Si atoms close-packed plane is called Si-face (0001). On the other hand, the face which is terminated by C atoms close-packed plane is called C-face (000-1). [1-21] The two faces exhibit different polarity which could affect the crystal growth process. The illustration of Si-face and C-face of 4H-SiC crystal is shown in Fig. 1.7. Fig. 1.8 (a) and (b) show the morphology on Si face and C face respectively. Steps on the Si face appear zig-zag shape while steps on C face are relatively smooth. The cross-sectional TEM images of Si and C face are shown in Fig 1.8 (c) and (d). The step height of Si face is 150 nm. Meanwhile, on C face many small steps distributed along the facet of gentle macrosteps. The inset in Fig. 1.8 (d) is the magnification of step facet. The height of small step is 2 nm. [1-22] Our group assumed that different surface morphologies on Si and C face are related to polarity.

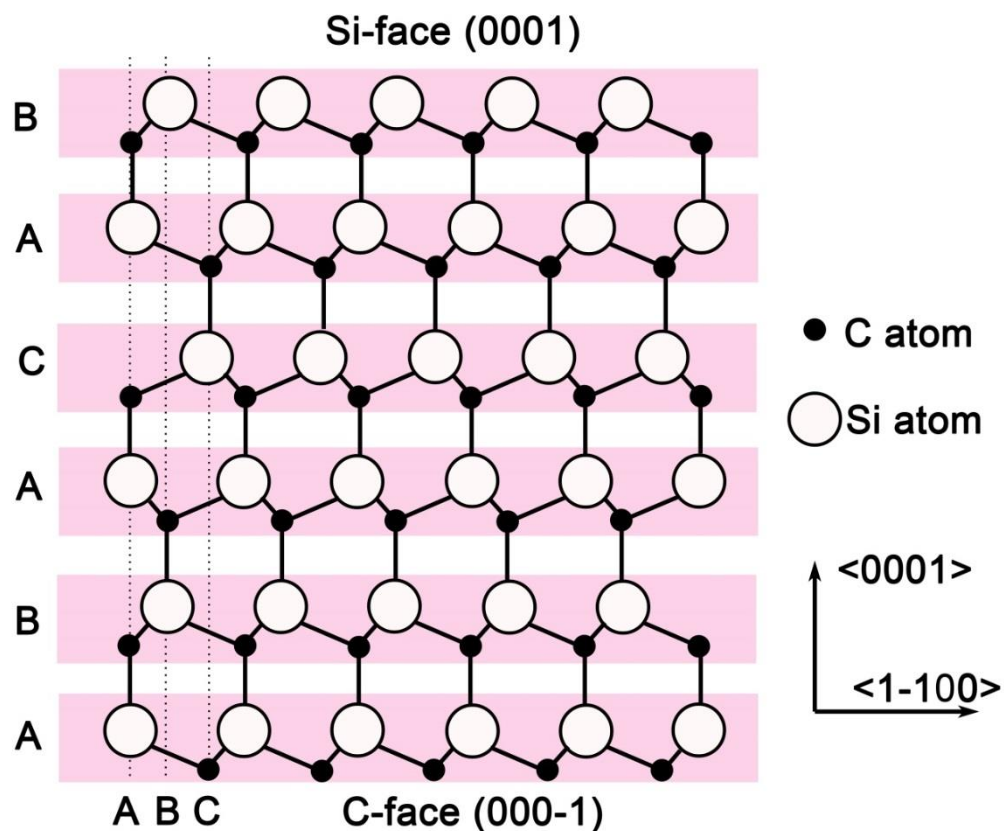


**Fig. 1.7** The illustration of polarity (Si face and C face) in SiC crystals. The face which is terminated by Si atoms close-packed plane is called Si-face (0001). On the other hand, the face which is terminated by C atoms close-packed plane is called C-face (000-1).

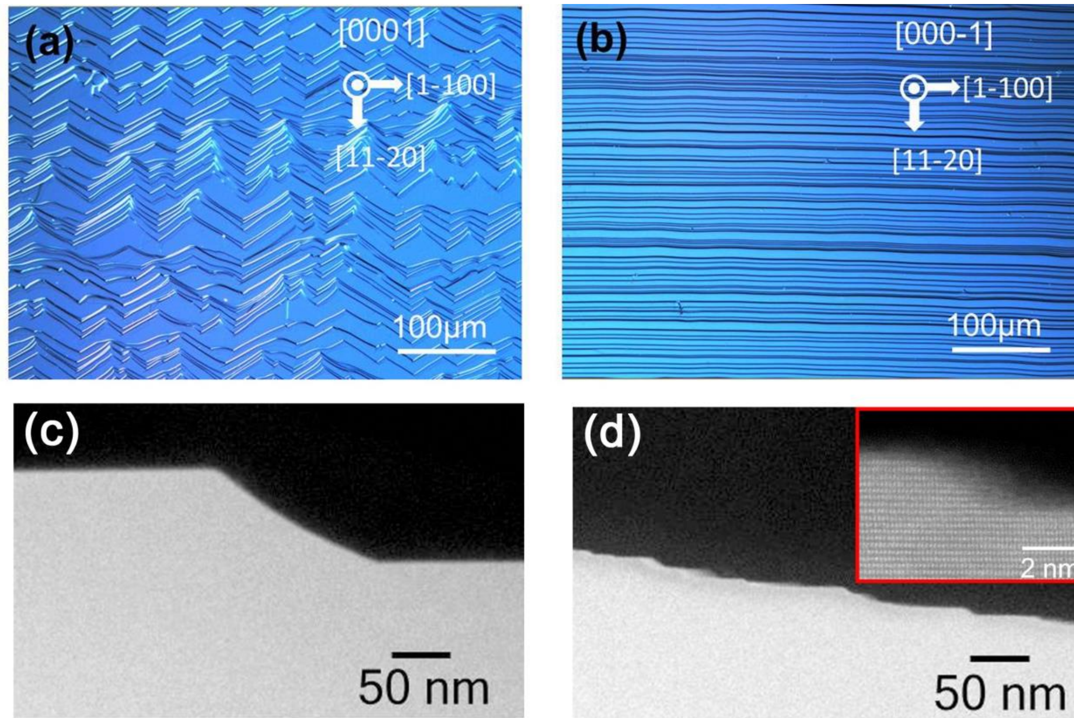


**Fig. 1.8** The morphology of (a) Si-face and (b) C-face grown crystal; The cross-sectional TEM observation of steps structure on (c) Si-face and (d) C-face grown crystal. The magnification is shown in the inset. [1-22]

### 1.4.3 SiC power devices

With the SiC crystal growth technology developed, SiC single crystals are becoming more and more important in the field of electronics. [1-23] Silicon carbide (SiC) has been proved to be a choice of materials for the next-generation power devices, because of its excellent physical properties such as high break down field, wide band gap and high thermal conductivity. In recent years, SiC power devices have developed fast. The on-resistance of SiC Schottky Barrier Diode (SBD) is $10^2$-$10^3$ lower than that of Si. Therefore, the application of SiC SBD could reduce the on-resistance under 2-3KV and realize the unipolar diode within voltage levels mainly include 600-3000V. [1-24] The application of SiC could improve PiN diode greatly comparing to Si since SiC exhibits higher breakdown voltage, band-gap and thermal conductivity which could increase the working temperature, reduce the thickness of drift layer and improve heat dissipation. SiC bipolar device could be applied under 5-10 KV. The most popular SiC power devices for high-current applications are 15 KV Insulated Gate Bipolar Transistors (IGBT) which is developed for smart grid applications. [1-25]

The SiC and Si applications are shown in Fig. 1.9. SiC could be applied to making power devices which are used under high voltage high frequency and high temperature. Nowadays, SiC power device applications have been launched in several developed countries like America and Japan. In 2009, the SiC inverters made by Fuji Electric are10 times smaller than that made from Si under the same power density. Mitsubishi Electric applied SiC inverters to their air conditioners in 2010. The SiC inverters were also applied to the Tokyo Ginza line subway trains in 2012. [1-26] Cree America and ROHM Japan have already started selling SiC SBD and MOSFET. [1-27, 28]

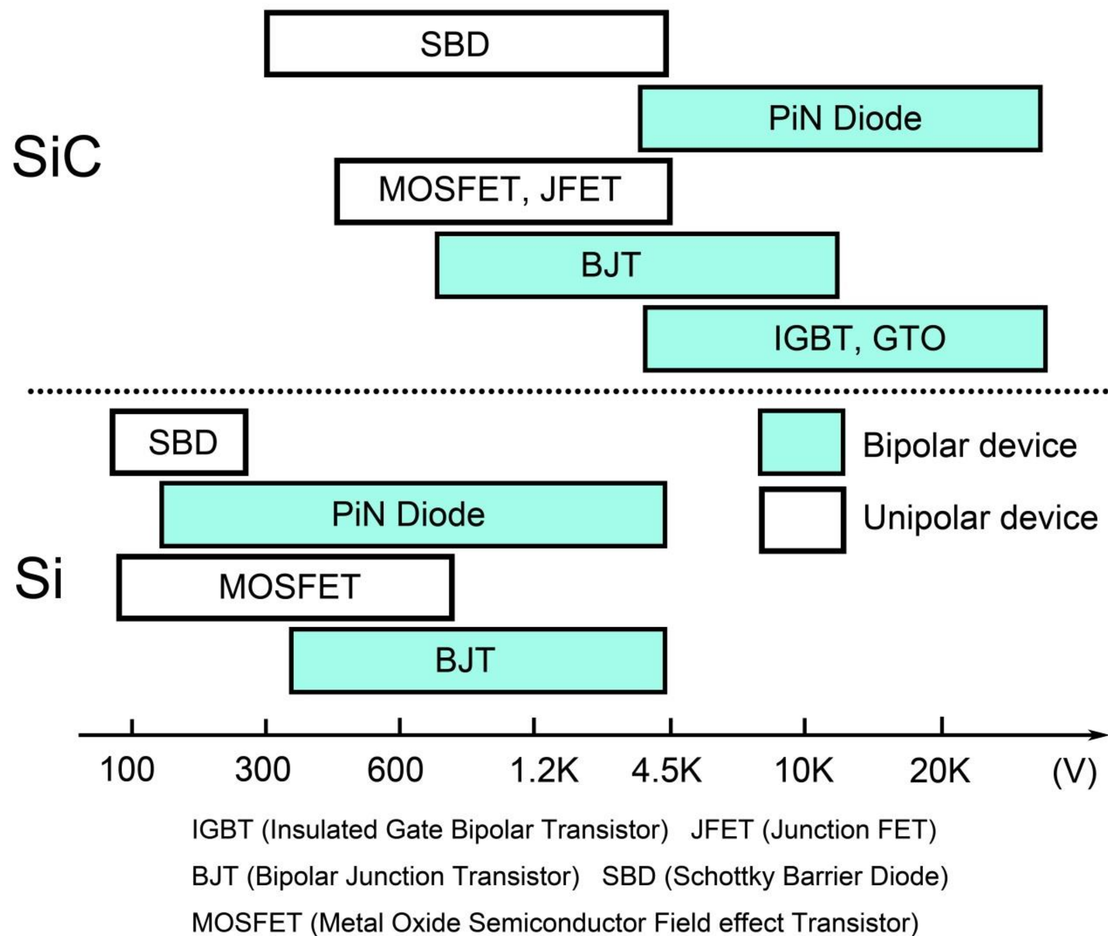


**Fig. 1.9** The varieties of Si and SiC devices and their field of areas of applications.[1-25]

## 1.5 Growth of SiC single crystal

The research of SiC single crystal growth has a long history and could be traced back to the 19th century. [1-29] Berzelius et al. from Karolinska University found a kind of unknown compound which has equal numbers of Si and C atoms. They proposed the Si-C bond could exist stably. This compound is SiC. Usually the high quality crystals are grown from liquid phase. The common semiconductor crystals such as Si, Ge, GaAS and so on could be obtained from melt. [1-23] However, for SiC crystal couldn't be grown from melt since it has extremely high melting point and sublimes before it melts according to the Si-C binary phase diagram (Fig. 1.10). [1-29] Thus, it is not feasible to grow SiC single crystal from the melt using like Bridgman method or Czochralski. The SiC bulk growth method can be classified into two categories as vapor phase growth and liquid phase growth known as solution growth method. The Vapor phase growth includes modified-Lely method and high-temperature chemical vapor deposition (HTCVD). The SiC epitaxial growth includes chemical vapor deposition (CVD), vapor liquid solid (VLS) and liquid phase epitaxy (LPE). The commonly used technique for growing commercial SiC wafers is physical vapor transport (PVT) which is also called as seeded modified Lely growth or sublimation recrystallization method. [1-30]

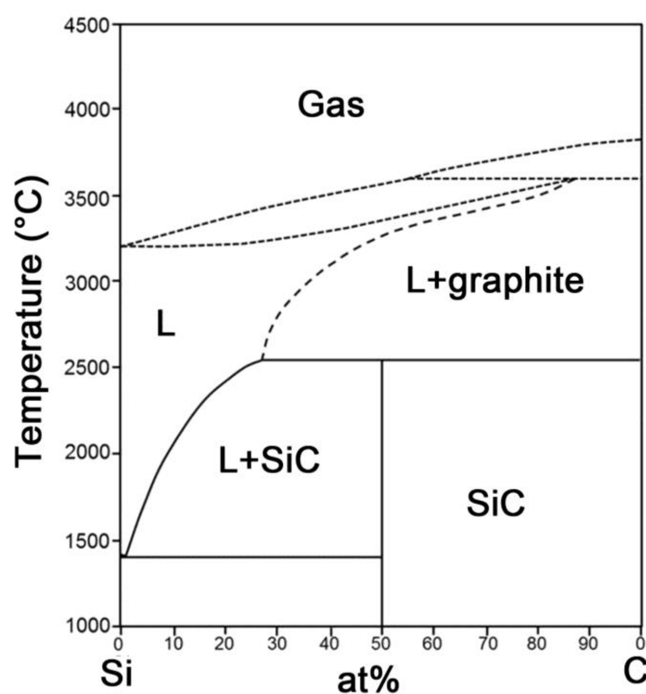


**Fig. 1.10** The phase diagram of the Si-C system at 1 atm.[1-31]

### 1.5.1 Sublimation recrystallization method

In 1955, Lely from Philips Germany obtained SiC single crystal. The SiC powder was putted in a closed graphite crucible and heated to about 2500 °C under Ar atmosphere. The SiC powder sublimed and re-crystallized in the colder zone at a seed. This method is called Lely method. The dislocations density of the grown SiC crystal by this method is about $10^2$-$10^3$ $cm^{-2}$. [1-32] However, it is hard for this method to control the nucleation and restrain the dendritic formation. Tairov and Tsvetkov improved Lely method.[1-33] The improved method is named PVT or Sublimation recrystallization method. In this thesis, we call this method as Sublimation recrystallization method.

The illustration of the Sublimation recrystallization method was illustrated as Fig. 1.11. The SiC powder is putted in graphite crucible and the seed crystal is placed on the inner surface of crucible cover. The growth temperature and temperature gradient is set by the furnace. The SiC powder is heated and sublimate above 2300 °C under Ar atmosphere. The sublimated Si and C gas would recrystallize on the seed crystal surface in the cold zone. By this method the gas transport stability is improved and the nucleation process during initial growth could be better controlled. At present, 6 inch SiC wafers are sold in the market from 2012. The research about enlargement of SiC crystal size is becoming a hot topic.

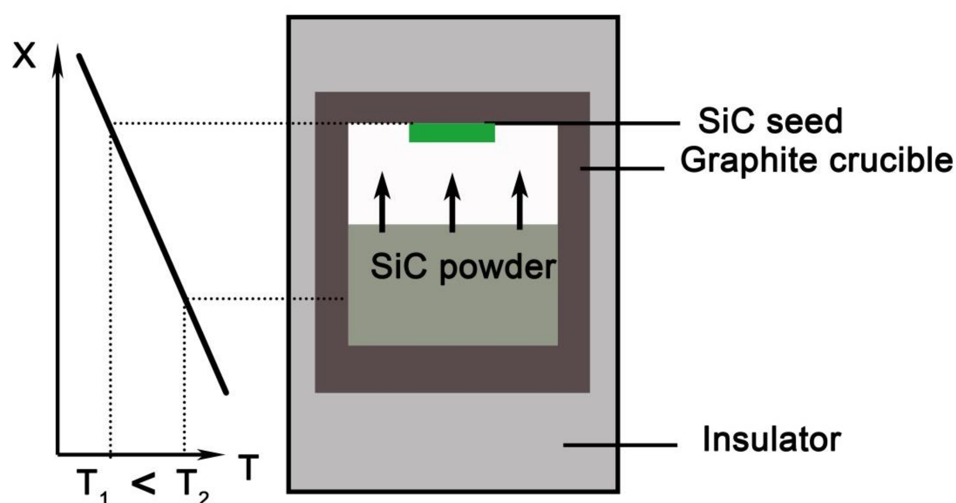


**Fig. 1.11** Schematic illustration of PVT growth of SiC crystal.

## 1.5.2 Modified physical vapor transport method (M-PVT)

In 2002 Strubinger et al. proposed a method which could realize the high density doping and growth at the same time. A piper is inserted into the graphite crucible as shown in Fig. 1.12 (c). For n-type doping, the carrier density of crystals grown by M-PVT increased dramatically comparing to that obtained by PVT. For the crystals grown by M-PVT the carrier density is above $1.0\times10^{20}cm^{-3}$ comparing to $1.0\times10^{19}cm^{-3}$ in PVT grown crystals. Fig. 1.12(a) illustrates the traditional PVT doping furnace set.[1-34,35]

In the case of p-type doping using aluminum, the aluminum-containing source is inserted directly into the SiC powder source material as shown in Fig. 1.12 (b). Since the much higher partial pressure of aluminum than Si and C containing gas, it is hard to control the transport. In order to overcome the poor gas phase composition control, M-PVT is used. The gas containing Al could apply Al source to the growth surface continuously. [1-34,35,36]

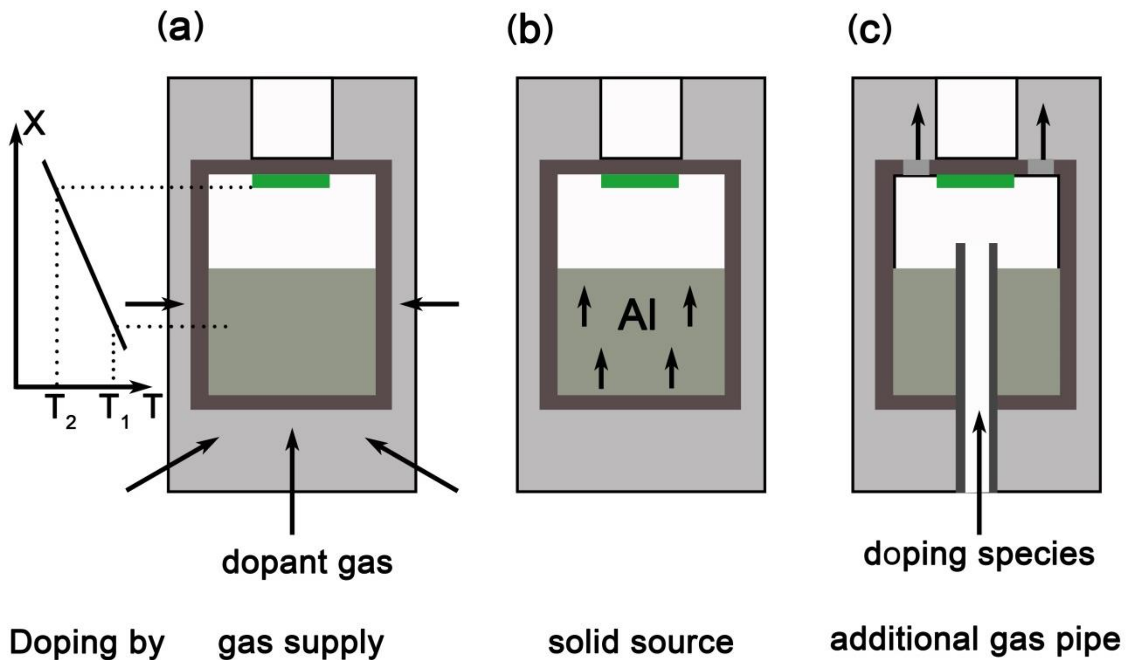


**Fig. 1.12** Sketch of the physical vapor transport (PVT) setup for SiC crystal growth: (a) Conventional PVT configuration and corresponding temperature field; (b) Conventional PVT configuration for doping using solid sources as addition to the SiC source material; (c) Modified PVT configuration using an additional gas pipe for the introduction of doping gases and/or small amounts of C- and Si- containing gases. [1-35]

### 1.5.3 Chemical vapor deposition (CVD)

For SiC epitaxial growth, the commonly technology is CVD method by using $H_2$-$SiH_4$-$C_3H_8$ gas under 1500-1600 °C. The etching would happen when the temperature is above 1600 °C due to the $H_2$ in the carrier gas. [1-37] The growth speed is about several μm per hour. The CVD growth illustration is indicated in Fig. 1.13. The SiC seed crystal is placed on the susceptor and heated to the growth temperature. The SiC epi-layer would form on the SiC substrate by the supply of gas.

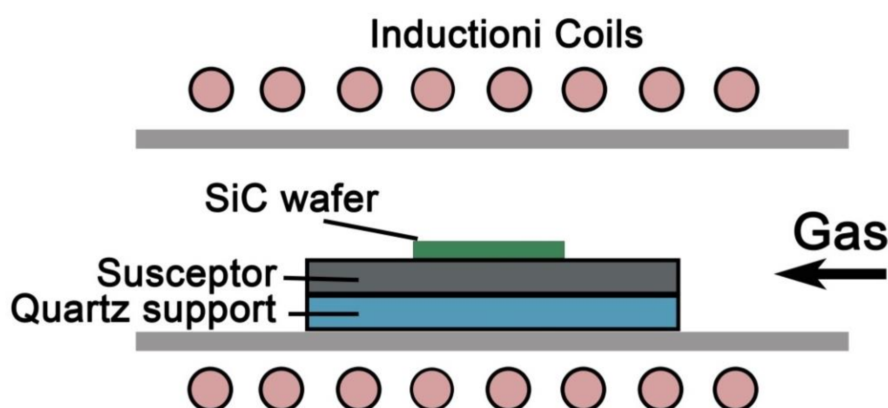


**Fig. 1.13** Schematic illustration of CVD growth of SiC crystal.[1-38]

### 1.5.4 Solution growth

Solution growth has a long history. Form 1960 the solution growth became a main way to grow SiC single crystal. However this method reached a plateau since the sublimation recrystallization method has made significant progress in SiC bulk growth. Recently, the SiC solution growth has attracted more and more attention with the development of crystal growth technology and equipment. In 1990, the micropipes from substrates were observed closed in the grown crystals after solution growth. The dislocation density in grown crystals grown by solution growth was reduced comparing to the substrates in 1998. Comparing to PVT, the quality of grown crystal is higher since the growth conducts closed to the thermal equilibrium. [1-39, 40, 41] The representative solution growth methods are shown in Fig. 1.14.

Slow cooling technique is indicated in Fig. 1.14 (a). The supersaturated solution is prepared and the temperature of the solution is reduced in small step. The solution which is just saturated will become supersaturated solution. Once the supersaturation

achieved, the crystal would crystallized on the seed crystal which is placed in the crucible. The main drawback is the need to use a range of temperature which would result in varies property crystal. [1-42]

The travelling solvent method (TSM) is shown in the Fig. 1.14 (b). The SiC source is placed with the SiC seed crystal and heat to the interface of SiC source melt. The SiC would recrystallize on the seed crystal since the seed crystal is at lower temperature. The crystal grown by the TSM method usually only could achieve several hundred μm due to the limit of the thickness of solvent.[1-43]

The top seeded solution growth (TSSG) method is shown in Fig. 1.14 (c). The Si is placed in the graphite crucible and heated to the growth temperature. The seed crystal is attached to the rod and dipped into the solution during growth. The C source is supplied from the graphite crucible. [1-44]

The illustration of Vapor-liquid-solid method (VLS) is shown in Fig 1.14 (d). The C source is supplied by the Hydrocarbon gas and propane and so on. The dissolved C would react with Si in the solution and crystalize on the seed crystal. The VLS method is mainly used for the epitaxial growth. [1-45]

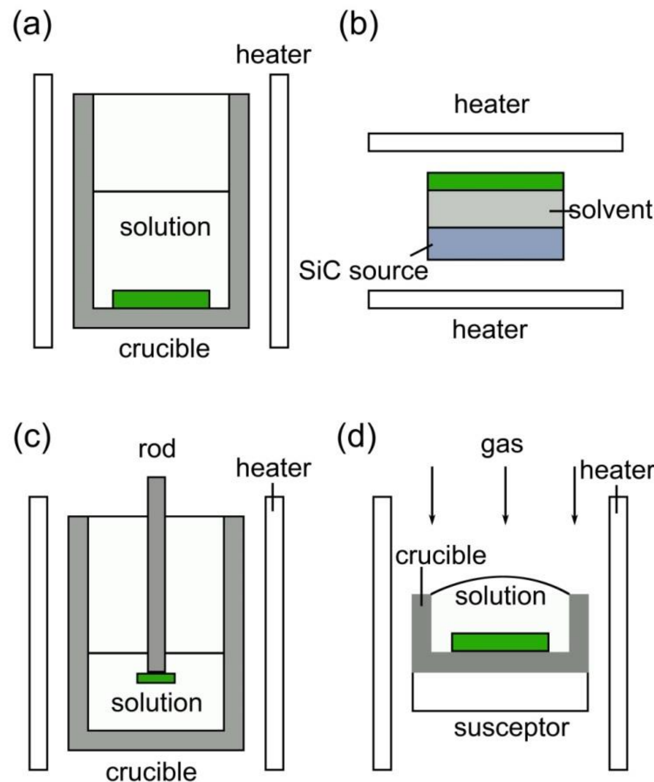


**Fig. 1.14** The illustration of representative solution growth methods: (a) Slow cooling technique (b) Travelling solvent method (c) Top seed solution growth method (d) Vapor-liquid-solid method.[1-46, 47]

## 1.6 Dislocations in SiC

6-inch SiC wafers have been commercially available from 2012. There are several types of dislocations in SiC crystals including threading screw dislocations (TSDs), threading edge dislocations (TEDs) and basal plane dislocations (BPDs). The dislocations density is still high comparing to the other semiconductor materials. Currently, the TSDs, TEDs and BPDs density in commercial wafer is about 300-500 $cm^{-2}$, 2000-5000 $cm^{-2}$ and 500-1000 $cm^{-2}$ respectively. [1-48] Fig. 1.15 shows the schematic of TSDs, TEDs and BPDs in SiC crystal. The characterization of TSDs, TEDs, BPDs and other types of dislocations is listed in Table 1.3. The primary slip plane in SiC is {0001} and the primary slip system is (0001)<11-20>. In this section, the current understanding of dislocations would be introduced in detail.

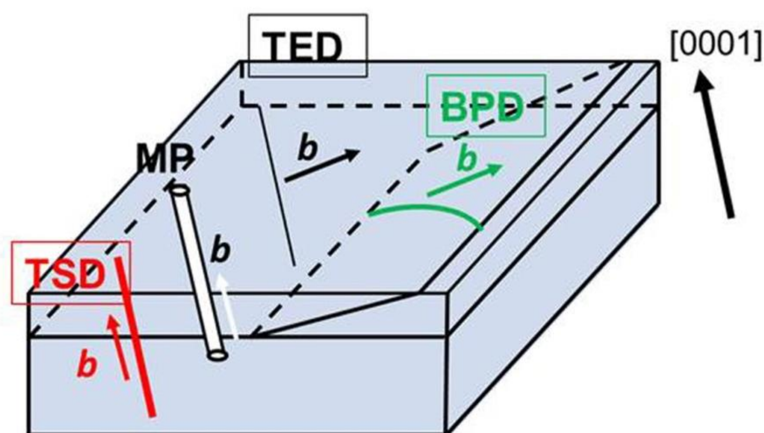


**Fig. 1.15** The illustration of dislocations in SiC wafer.

**Table 1.3 Characters of various dislocations in 4H-SiC**[1-48]

| | Dislocation line (*u*) | ***b*** |
|---|---|---|
| TSD | Roughly // *c*-axis | n<0001> (10.05n Å) |
| TED | Roughly // *c*-axis | 1/3<11-20> (3.08 Å) |
| BPD | // *c*-plane | 1/3<11-20> (3.08 Å) |
| Frank partial dislocation | // *c*-plane | 1/4<0001> (2.51 Å) |
| Shockley partial dislocation | // *c*-plane | 1/3<1-100> (2.51 Å) |

* n is an integer

## 1.6.1 Threading screw dislocation

Assuming the $z$-axis is along the dislocation line $u$. The dislocation lines of TSDs are approximately along $c$-axis and their Burgers vectors are (0001) which is parallel to $c$-axis. The displacement field of theirs has only c-component: [1-49]

$$u_z = (b/2\pi)arctan(y/x) \quad (1.2)$$

where $\boldsymbol{b}$ is the Burgers vector of TSD.

The strain components perpendicular to the surface has to be zero in order to satisfy the free surface condition. Therefore if a TSD is close to the surface an additional in-plane displacement due to the surface relaxation effect should be considered. According to Eshelby and stroh, the additional displacement field of a TSD in an infinite plate with surfaces $z = \pm\, t$: [1-50]

$$u_x = u_\theta(x,y,z)\frac{-y}{\sqrt{x^2+y^2}} \quad (1.3)$$

$$u_y = u_\theta(x,y,z)\frac{x}{\sqrt{x^2+y^2}} \quad (1.4)$$

where

$$u_\theta(x,y,z) = -\frac{b}{2\pi}\sum_{n=0}^{\infty}(-1)^n\left\{\frac{x^2+y^2}{(2n+1)t-z+\sqrt{[(2n+1)t-z]^2+(x^2+y^2)}} - \frac{x^2+y^2}{(2n+1)t+z+\sqrt{[(2n+1)t+z]^2+(x^2+y^2)}}\right\} \quad (1.5)$$

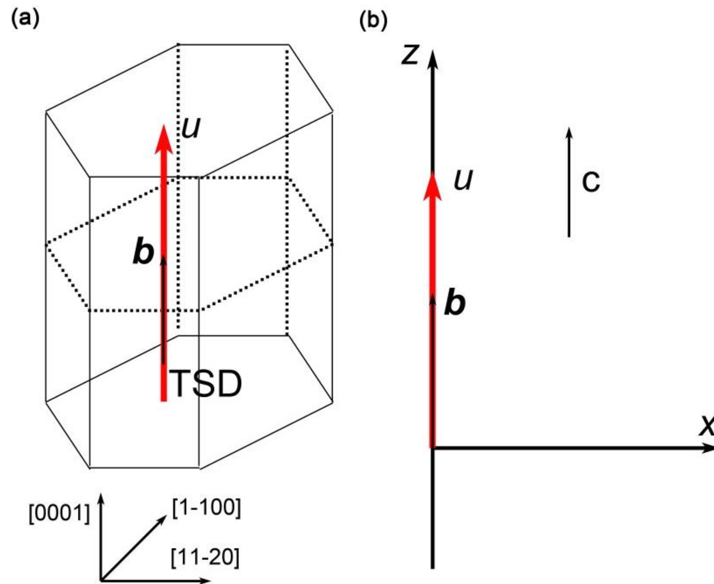


**Fig. 1.16** (a) A TSD in SiC (b) Geometry used in obtaining the displacement field of a TSD.

The additional displacement field associated with the surface relaxation effect influences the topographic images of TSDs in grazing-incidence geometry and it causes the asymmetric contrast in topo images. The TSD sense could be distinguished by those asymmetrical contrasts. [1-51] Recent studies revealed that many TSDs has a Burgers vector of **c**+**a**. They are mixed dislocations instead of pure screw type. [1-48, 52, 53]

## 1.6.2 Threading edge dislocation

Let the dislocation TED line *u* is along *z*-axis, the Burgers vector is at an angle $\theta$ to the *x*-axis as shown in Fig. 1.17. For the hexagonal crystal, we set *x*-axis along [11-20] direction and *y*-axis perpendicular to the *xz*-plane. Therefore, the displacement field is a combination of two components $\boldsymbol{b}_x$ and $\boldsymbol{b}_y$. The displacement associated with the edge component $\boldsymbol{b}_x$ is given by: [1-54]

$$u_x = \frac{b\sin\theta}{2\pi}\left[tan^{-1}\frac{y}{x} + \frac{xy}{2(1-v)(x^2+y^2)}\right] \tag{1.6}$$

$$u_y = -\frac{b\sin\theta}{2\pi}\left[\frac{1-2v}{4(1-v)}ln(x^2+y^2) + \frac{x^2-y^2}{4(1-v)(x^2+y^2)}\right] \tag{1.7}$$

Similarly, the displacement of the other edge component $\boldsymbol{b}_y$ is:

$$u_x = \frac{b\cos\theta}{2\pi}\left[tan^{-1}\frac{-x}{y} + \frac{-xy}{2(1-v)(x^2+y^2)}\right] \tag{1.8}$$

$$u_y = -\frac{b\cos\theta}{2\pi}\left[\frac{1-2v}{4(1-v)}ln(x^2+y^2) + \frac{y^2-x^2}{4(1-v)(x^2+y^2)}\right] \tag{1.9}$$

where the $v$ is the Poisson's ratio.

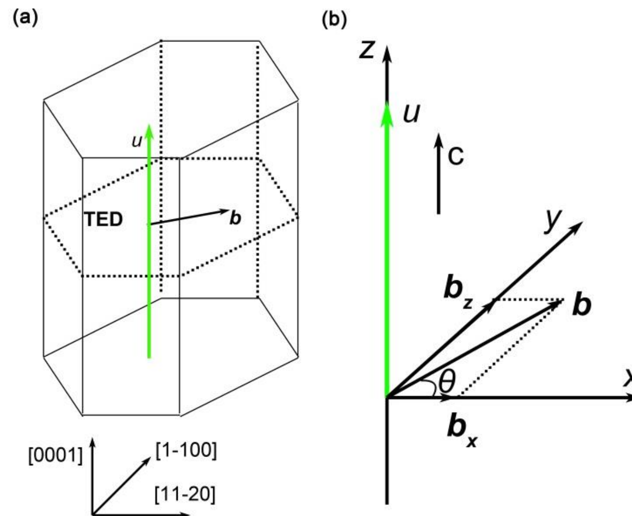


**Fig. 1.17** (a) A TED in SiC (b) Geometry used in obtaining the displacement field of a TED.

The conversion of TEDs to BPDs and BPDs to TEDs are often observed inside the boule crystals. [1-55,56]

## 1.6.3 Basal plane dislocation

Set a BPD line direction along *z*-axis in *c*-plane. The Burgers vector direction is ta angle $\theta$ to the *z*-axis as shown in Fig. 1.18. The *x*-axis is perpendicular to c-axis and the xz plane is parallel to the basal plane. The Burgers vector of a BPD can be break into edge and screw two components. The edge component is along *x*-axis ($\boldsymbol{b}_e = |\boldsymbol{b}|\sin\theta\boldsymbol{i}$) and the screw part is along *z*-axis ($\boldsymbol{b}_s = |\boldsymbol{b}|\cos\theta\boldsymbol{k}$). The displacement field of the screw component which is along *z*-axis is given by: [1-54]

$$u_z = \frac{b\cos\theta}{2\pi} tan^{-1}\left(\frac{y}{x}\right) \tag{1.10}$$

The displacement field of the edge component is given by:

$$u_x = \frac{b\sin\theta}{2\pi}\left[tan^{-1}\frac{y}{x} + \frac{xy}{2(1-v)(x^2+y^2)}\right] \tag{1.11}$$

$$u_y = -\frac{b\sin\theta}{2\pi}\left[\frac{1-2v}{4(1-v)} ln(x^2+y^2) + \frac{x^2-y^2}{4(1-v)(x^2+y^2)}\right] \tag{1.12}$$

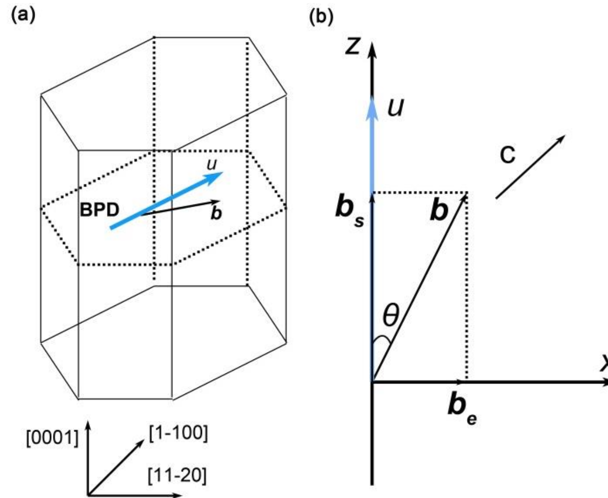


**Fig. 1.18** (a) A BPD in SiC (b) Geometry used in obtaining the displacement field of a BPD with Burgers vector at angle $\theta$ to the line direction.

### 1.6.4 Frank-type partial dislocation

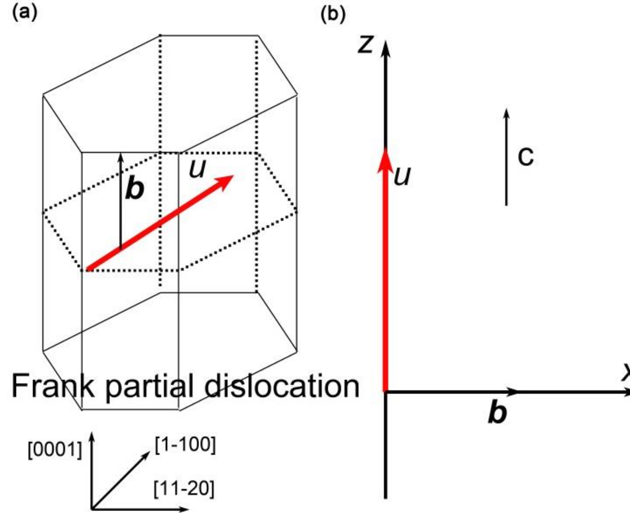


**Fig. 1.19** (a) A Frank-type partial dislocation in SiC (b) Geometry used in obtaining the displacement field of a Frank type partial dislocation.

Frank partial dislocation is the partial dislocation in the basal plane with Burgers vector component out of plane. Tsuchida et al. found a type of Frank partial dislocation in SiC crystal whose line direction is in *c*-plane Burgers vector is 1/4<0001> and they could possibly nucleated with TSDs simultaneously. Tsuchida et al. report that the TSDs converted to Frank-type SFs which composed of 4 extrinsic Frank partial dislocations during solution growth.

Set the line direction is along z-axis and the Burgers vector is along x-axis as shown in Fig. 1.19. The displacement field is given by: [1-57]

$$u_x = \frac{b}{2\pi}\left[tan^{-1}\frac{y}{x} + \frac{xy}{2(1-v)(x^2+y^2)}\right] \tag{1.13}$$

$$u_y = -\frac{b}{2\pi}\left[\frac{1-2v}{4(1-v)}ln(x^2+y^2) + \frac{x^2-y^2}{4(1-v)(x^2+y^2)}\right] \tag{1.14}$$

### 1.6.5 Dislocations' influence on power device and reduction

The dislocations in SiC crystal could influence the performance of various kinds of power devices. [1-58] The micropipes are harmful and would decrease the breakdown voltage of power devices dramatically. TSDs not only reduce breakdown voltage but also the quality of oxidation layer. Meanwhile, the carrier lifetime would be reduced by TEDs. BPDs would affect the quality of oxidation layer and leakage current in the

power devices. [1-59]

Considering the serious effect on the performance of power devices of TSDs and BPDs, lots of effort has been done to reduce their density. So far, the researchers have already made significant progress on the reduction of dislocations density. Dow Coring et al. reported they were successfully reduce the micropipe density down to 0.1 $cm^{-1}$, the TSD density down to 500 $cm^{-1}$ and BPD density between 300-400 $cm^{-1}$ in the 4 inch n-type wafer in 2012. [1-60] Dudley et al. reported they had decreased the BPD density through reducing the stress in the crystal during PVT method. [1-61] Ha et al. observed the BPDs could convert to TEDs which was helpful to the reduction of BPDs density. Nakamura et al. proposed a method called repeated a-face growth that the TSDs density could be reduced dramatically.[1-62] Urakamei et al. reduced the TSD density below 1.3 $cm^{-2}$ by using repeated a-face growth in 2012. [1-63] Kusunoki et al. eliminated BPD by using solution growth by on-axis substrates.[1-64]Yamamoto et al. realized the dramatically reduction of TSD density by utilizing the TSD conversion phenomenon during solution growth. [1-65]

## 1.7 Dislocations behavior during solution growth

Yamamoto et al. reported that the TSDs convert to Frank-type stacking faults (SFs) on the basal plane during solution growth on the Si face. [1-66] Fig. 1.20 (a) and (b) show the topographic images of on-axis Si face substrate and grown layer at the identical position. The white circle contrasts indicated by the red circle in Fig. 1.20 (a) is corresponding to TSD. By a comparison of the topo images of substrate and the grown layer the TSD indicated by the red circle just propagated from the substrate. Moreover, according to the Nomarski image (Fig. 1.20 (c)) at the same position with the topo images the spiral hillock as indicated by the red circle could be observed at the same location with the TSD. The spiral growth is conducted with the TSD as the center. On the other hand, the TSD indicated by the red arrow in Fig. 1.20 (a) converted to defects on basal plane corresponding to knife shaped contrast indicated by the red arrow in Fig. 1.20 (b). By comparing the topo image and the morphology, Yamamoto et al. proposed that the conversion mechanism was related to the step height since the conversion phenomenon only was observed when there was macrostep. Meanwhile, the line contrasts and small white circle contrasts correspond to BPDs and TEDs respectively as shown in Fig. 1.20 (a). [1-66]

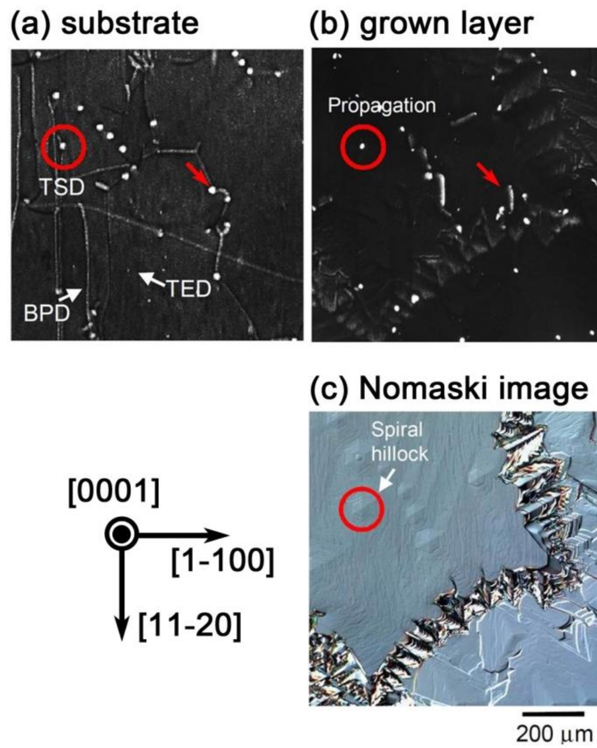


**Fig. 1.20** X-ray topography images of the 4H-SiC (0001) Si-face on-axis (a) seed crystal and (b) grown crystal. (c) Nomarski image of the grown surface taken at the same position. The TSD (as indicated by red circle) in the seed crystal propagated into the grown crystal (red circle in (b)). The spiral hillock (as indicated by red circle in (c)) originated from the TSD (as indicated by red arrow in (b)) was observed. On the other hand, the TSD (indicated by red circle in (b)) was converted to another type of defect (indicated by red arrow in (b)). A spiral hillock was not found at the identical position.

Currently, the off-axis substrates are commonly used for the SiC growth since they favor the polytype stability. The dislocations behavior during off-axis (0001) Si face solution growth is shown in Fig. 1.21. The topo images were taken before (Fig. 1.21 (a)) and after (Fig. 1.21 (b)) growth at the same position. The TSD indicated by the red circle in Fig. 1.21 (a) converted to the knife-shaped contrast corresponding to SF indicated by red ellipse in Fig. 1.21 (b). On the other hand, the small white circle corresponding to TED as indicated by the yellow circle Fig. 1.21 (a) converted to line contrasts corresponding to BPD indicated by the yellow ellipse Fig. 1.21 (b). Harada et al. reported that nearly 100% TSDs could convert to SFs on off-axis (0001) Si face with the growth conducting. [1-66]

However, the dislocations behavior on off-axis (000-1) C face was different from Si face. The TSD indicated by the red circle in Fig. 1.22 (a) propagated to the grown crystal

as shown in Fig. 1.22 (b). No TSD conversion phenomenon was observed on off-axis (000-1) C face with pure Si solvent. The TEDs indicated by the yellow circle in Fig. 1.22 (a) convert to the BPDs indicated by yellow ellipse in Fig. 1.22 (b) just like that on Si face.[1-66]

Ujihara et al. and Harada et al. have already made lots effort to determine the conversion detail and mechanism by using X-ray topography, KOH etching and TEM observation. [1-66, 67, 68] However, the conversion mechanism is still unclear

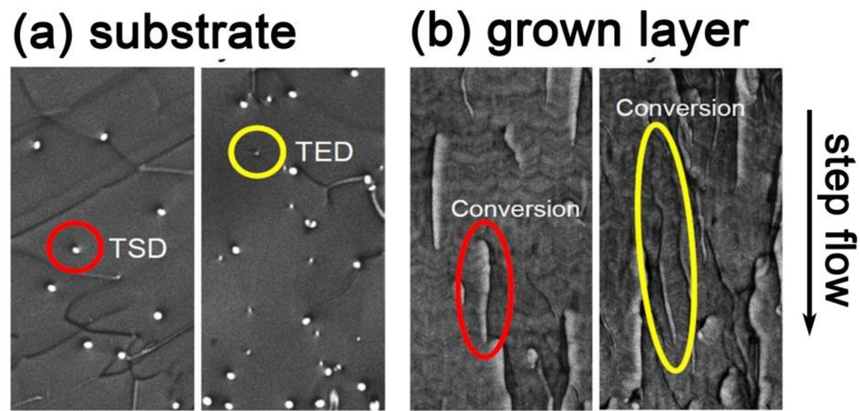


**Fig. 1.21** X-ray topography images of the 4H-SiC (0001) Si-face off-axis (a) seed crystal and (b) grown crystal taken at the same position. The TSD (red circle in (a)) was converted to the defects on basal plane (red ellipse in (b)). On the other hand, the TED (yellow circle in (a)) was converted to the BPD (yellow ellipse in (b)).

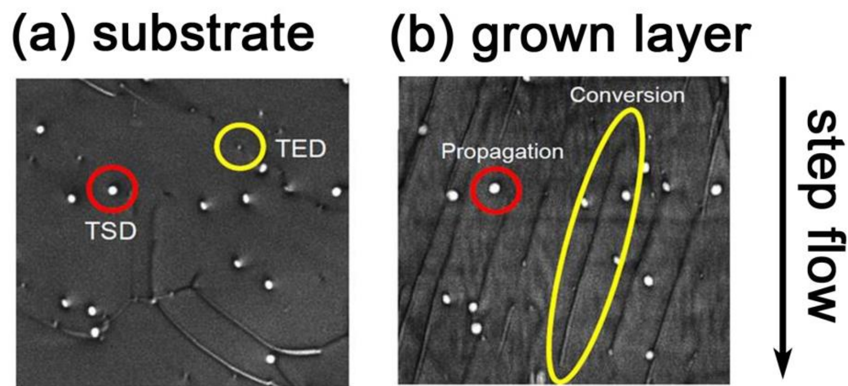


**Fig. 1.22** X-ray topography images of the 4H-SiC (000-1) C-face off-axis (a) seed crystal and (b) grown crystal taken at the same position. Although the TED (as indicated by yellow circle in (a)) was converted to BPD (as indicated by yellow ellipse in (b)). The TSD (as indicated by red circle in (a)) in seed crystal propagated into the grown crystal (as indicated by red circle in (b)).

## 1.8 High-quality SiC solution growth

Currently, SiC solution growth has attracted more and more attention since it is an effective way to obtain high quality crystals. In order to realize the high quality SiC bulk growth, several technical subjects appeared with the rapid development of SiC solution growth. For example, the way how to increase the growth rate, the way how to stable the polytype during bulk growth, the way how to decrease the dislocation density, the way how to control the doping density and the way how to obtain long-size and large diameter crystal and so on. Among them, the most important topic should be the design of solvent composition since the different composition would influence like the morphology, the growth rate, the doping concentration, etc. To achieve large size high quality SiC bulk growth, it is necessary to solve and optimize all the subjects. The present state about these technical subjects would be introduced in this section.

### 1.8.1 Solvent composition

As we know, in solution growth the growth rate depends on the C solubility. In order to raise the growth rate, the addition of some elements which could increase the C solubility into the solvent seems a good choice. The addition elements should be abundant, easy to use and obtain high purity and low solid-solubility. Which element should be chosen and how to determine their component in solvent are still critical topics. Those additional elements in SiC solution growth usually are transitional metal. Many researchers have committed themselves to find the best composition of the solvent. CALculation PHAse Diagram (CALPHAD) has been used extensively in calculating phase diagram for multicomponent system since there is no experimental one. The CALPHAD approach is based on the fact that a phase diagram is a manifestation of the equilibrium thermodynamic properties of the system, which are the sum of the properties of the individual phases. [1-69] The binary or multicomponent system phase diagram could be obtained by the thermodynamic analysis according to the experimental data like pressure, temperature, etc.

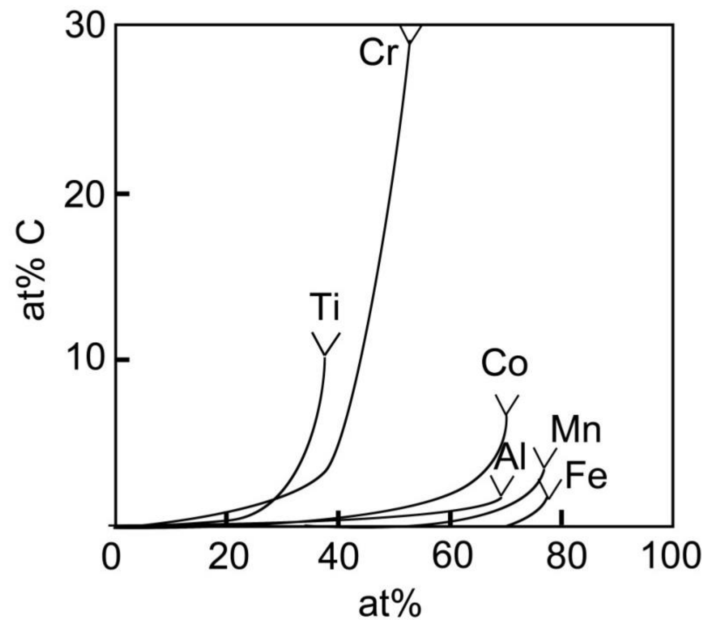


**Fig. 1.23** The graph of the C solubility dependence of the additive component in Si-X-C (X= Ti, Cr, Co, Al, Mn, Fe) solvent.

K. Kusunoki et al. reported the C solubility dependence of the component of several additional elements in Si-C-X ternary system. [1-70] As shown in Fig. 1.23, the addition of Titanium (Ti) and Chromium (Cr) could increase C solubility dramatically comparing to other elements. Therefore, currently titanium (Ti) and chromium (Cr) are widely used as the additional element. [1-71, 72, 73] For the determination of the solvent component, it is crucial to predicate of the phase diagram by calculation. K. Kusunoki et al. determined the component of solvent as $Si_{77}Ti_{23}$ according to their calculated phase diagram. [1-74] Many other research groups chose Cr as the addition elements considering the great C solubility.

## 1.8.2 Polytype stability

As mentioned in 1.4.1, SiC has nearly 200 types of polytype. If the stacking sequence of Si-C bilayer transform during solution growth the stacking faults would generate and then the polytype would change. In PVT and solution growth the polytype transformation is usually with the generation of SFs. In order to realize high-quality SiC bulk crystal growth, it is crucial to keep the polytype stable during solution growth. Theoretically, the Si-C bilayer stacking sequence should be kept exactly the same as the substrate if want to keep polytype stable. The stacking sequence is closely related to the growth mechanism. Spiral growth is usually used in PVT growth to keep the polytype

stable while the step-flow growth is used in CVD and solution growth. However, the morphology becomes rougher and rougher with the growth going on during solution growth by utilizing off-axis seed crystals. [1-75] Therefore it is hard to keep step flow growth and polytype stable for SiC solution bulk growth. On the other hand, 2D nucleation is utilized to conduct hetero-epitaxial growth. It is reported that 3C-SiC and 4H-SiC grown crystal could grow on 6H-SiC substrates. [1-76, 77, 78, 79,80]

So far, there is no report shows the 4H-SiC could be obtained by 2D nucleation mechanism during solution growth. Thus, in order to realize the high quality SiC bulk crystal during solution growth it is crucial to keep the spiral or step flow growth. TSDs are detrimental for the properties of power devices. However, considering that the TSDs play a crucial role to maintain desired polytype by applying spiral step growth, it is necessary for TSDs existing. Thus, it is disadvantage to decrease the TSD density to 0. [1-81]

### 1.8.3 The reduction of dislocations

On-axis substrates are commonly used to decrease BPD density since the BPDs in substrates could be eliminated with the growth process. BPDs were observed convert to TEDs during CVD growth. The BPDs density could be reduced by the converting to less harmful TEDs. Harada et al. reported that nearly 100% TSDs in off-axis substrate converted to defects on basal plane when the growth thickness achieves 10 μm. [1-67] On the other hand, the TSD conversion ratio was under 1% in CVD growth. [1-82] The reason resulting in the different conversion ratio was assumed to be the different step height. Ha et al. proposed that the conversion phenomenon is caused by the image force from the step. [1-62] The step height on the Si face grown crystal grown from solution growth is usually above 100 nm. Meanwhile, the step height on the grown crystal from CVD growth was only about 1 nm. [1-83] Yamamoto et al. proposed that the higher the step was the bigger the image force is. [1-66]

In addition, TEDs convert to BPDs which is helpful for the reduction of TEDs during solution growth. And BPDs on the basal plane would be excluded from the grown crystals with the growth process. Yamamoto et al. proposed a method to obtain ultra-high quality SiC grown crystals by utilizing of the TSD and TED conversion phenomenon as shown in Fig. 1.24. [1-65]

In conclusion, nearly all the TSDs and TEDs convert to defects on basal plane and BPDs during solution growth. Those dislocations on the basal plane would propagate along the basal plane and excluded from the grown crystal with the growth conducted.

As the results, the dislocation density would be reduced as the growth proceeds. Solution growth is an ideal method for high-quality crystal due to the TSDs conversion. However, the conversion phenomenon is only observed on Si face solution growth. How to decrease the TSDs density on C face is still open.

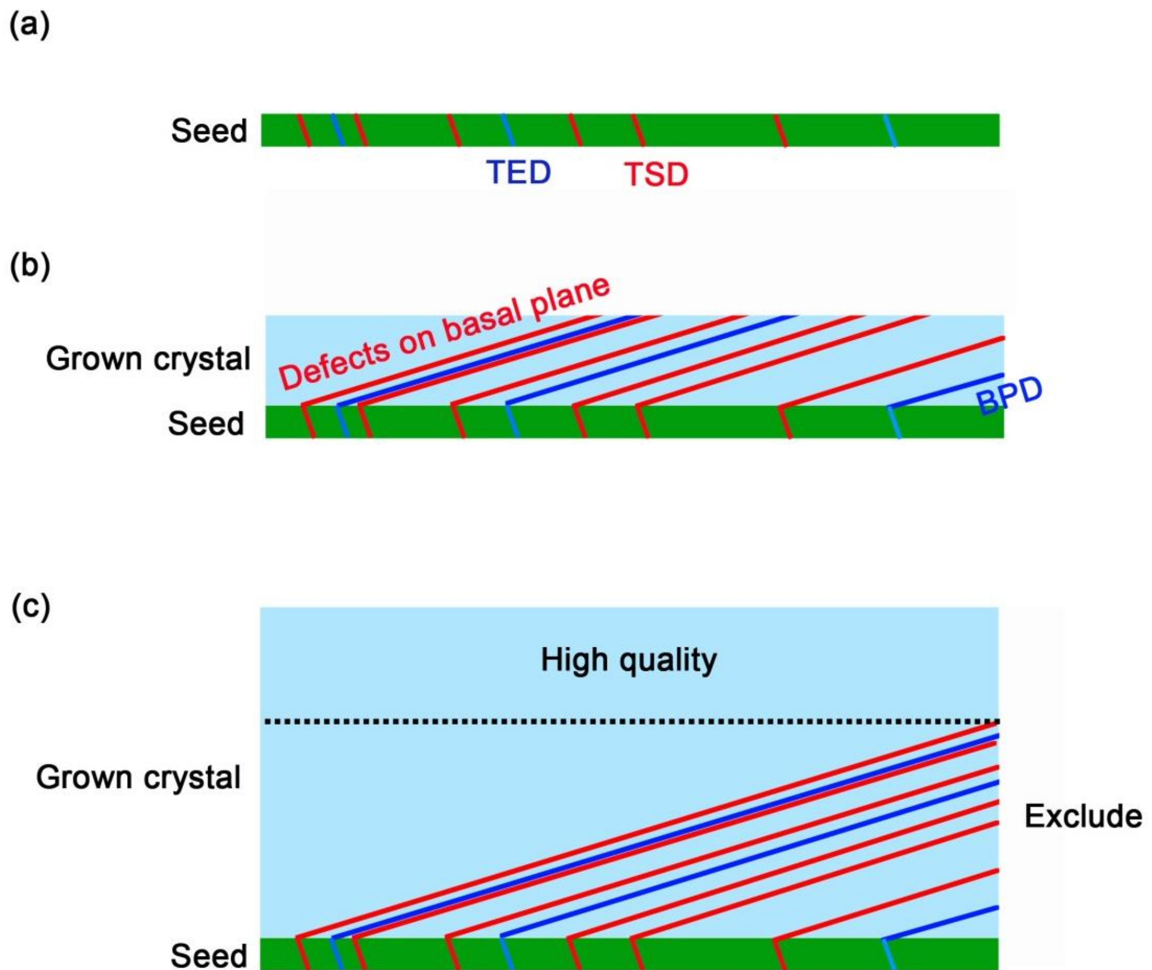


**Fig. 1.24** Schematic illustration of solution growth process on off-axis seed crystal in cross-sectional view. (a) Cross section of off-axis seed crystal and TSDs. (b) TSDs are converted to defects on basal plane during solution crystal by the step flow of macrosteps. (c) As the growth proceeds, defects on basal plane laterally propagate and are excluded from the crystal. A high-quality SiC crystal is obtained.

## 1.9 Objective and contents of this study

As described above, the demand of high quality SiC bulk crystals is becoming more urgent and higher with the development of power devices used under high power, high frequency and high temperature. The quality of grown crystals has been dramatically improved due to the effort for several decades. However, dislocations such as macropipes or TSDs still hamper the realization of high quality SiC crystals. Solution growth is considered as a promising method for high quality SiC crystal growth not only the growth conducted under the condition closed to thermal equilibrium but also the threading dislocation could convert to defects on basal plane. As the growth proceeds, the converted defects on basal plane could be excluded from grown crystals laterally. Therefore, dislocation density could be dramatically decreased by solution growth. However, there are still several problems need to be solved. For example, little research has been done about the generated defects which may hinder the reduction of defects during SiC solution growth. Another example is that the TSD conversion phenomenon has only been observed on Si face growth. That indicates that TSDs density could not be reduced since there is no TSDs conversion on C face growth. Whereas, the C face growth has attracted many attentions due to the difference to the Si face in many aspects and C-face seed crystals are often used for stabling polytype during bulk growth. Therefore the reduction of TSDs during C face growth is crucial.

In this study, in order to realize high quality SiC crystal growth we mainly focused on the reduction of defects during solution growth. The newly generated defects during solution growth and the method to reduce TSDs on C face growth were studied.

Our objective is to realize high quality SiC crystal growth by solution growth.

This thesis is divided into 7 parts. The specific structure and contents are as follow:

1. In chapter 1, the background and the objective of this study is introduced.
2. In chapter 2, the driving force in solution growth, the growth model and the experiment detail are introduced.
3. In chapter 3, the newly generated V-shaped defects are studied. The generation mechanism and the restrain method are proposed.
4. In chapter 4, the TSD conversion phenomenon is realized with additive. The step structure effect on TSD conversion behavior is also discussed.
5. In chapter 5, the TSD conversion ratio is promoted which is beneficial for the high quality SiC growth.
6. In chapter 6, high quality SiC C face grown crystals are obtained by two-step

growth.

7. In chapter 7, the conclusion of this study is described.

# Reference

[1-1] http://www.jccca.org/global_warming/knowledge/kno01.html.

[1-2] http://www.env.go.jp/earth/cop/cop19/index.html.

[1-3] Katsumata, H. The Quarterly MEIJI 51 (2001) pp 38.

[1-4] http://en.wikipedia.org/wiki/Power_semiconductor_device.

[1-5] Baliga, B.J., Fundamentals of power Semiconductor Devices, Springer Science and Business Media, New York, p1.

[1-6] http://en.wikipedia.org/wiki/Transformer.

[1-7] Kusunoki Kazuhiko, D thesis: Nagoya University, 2014, Chapter 1, pp 3.

[1-8] Baliga, B. Jayant., Power Semiconductor Devices. Boston: PWS publishing Company. ISBN 0-534-94098-6.

[1-9] Lal, K. and Bhagavannarayana, G., J. Appl. Cryst, 1989, 22, 209-215.

[1-10] Hoshikawa, K., Jpn. J. Appl. Phys., 1982, 21, L145-L547.

[1-11] Lan, C.W. and Kou, S., J. Cryst. Growth, 199, 108, 351-366.

[1-12] T. Shinohe, Toshiba review, 1982, 53, 49-53.

[1-13] Kumar, A. and Aspalli, M.S., IJRET, eISSN: 2319-1163/pISSN: 2321-7308.

[1-14] Tolbert, L.M.; Ozpineci, B.; Islam, S.K.; Chinthavali, M.S., Semiconducters, 2003, 1, 3.

[1-15] Hasegawa, F.; Minami, M.; Sunaba, K. and Suemasu, T., Jpn. J. Appl. Phys, 1999, 38, L 700-L 702.

[1-16] Yamada, H.; Chayahara, A.; Mokuno, Y.; Umezawa, H.; Shikata, S.; Fujimori, N., Appl. Phys. Express , 2010, 3, 051301.

[1-17] Knippenberg, W. Growth Phenomena in Silicon Carbide, Philips Research Report, 1963, 18, 161.

[1-18] Boulle, A.; Dompoint, D.; Galben-Sandulache, I. and Chaussende, D. Physcal Review B, 2013, 88(2), 024103.

[1-19] Castillo-Rodríguez, M.; Lara, A.; Munoz, A. and Domínguez-Rodríguez, A. J. AM. Ceram, Soc., 2013, 96(9), 2921-2925.

[1-20] Qteish, A.; Heine, V. and Needs J.R. Physcal Review B, 1992, 45(12), 6534.

[1-21] Stein, R.A.; Lanig, P.; Leibenzeder, S., Mat. Sci. Eng. B-Solid, 1992, 11, 67-71.

[1-22] Harada, S.; Yamamoto, Y.; Xiao, SY.; Tagawa, M.; Ujihara, T. Mater. Sci. Forum. 2014, 778, 67-70.

[1-23] Powell, A.; Jenny, J.; Muller, S.; Hobgood, H.McD.; Tsvetkov, V.; Lenoard, R. and Jr. Carter, C. International Journal of High Speed Electronics and systems, 2006, 16, 751-777.

[1-24] Shur, M.; Rumyantsev, S.L.; Levinshtein, M.E. SiC Materials and Devices, Vol. 2, Singapore: World Scientific, 2007.

[1-25] Kadavelugu, A.; Bhattacharya, S., IEEE Applied Power Electronics Conference and Exposition, 2014, ISSN 1048-2334, 1494-1501.

[1-26] Seki, K. Control of Polytype and Double Position Defects during the Solution Growth of 3C-SiC, Nagoy : Nagoya University Ph. D. Thesis, 2013.

[1-27] http://www.symmetron.ru/suppliers/rohm/handbook_power_device-e.pdf

[1-28] http://www.yole.fr/iso_upload/mag/powerdev_april2013_ir.pdf

[1-29] Chaussende, D.; Wellmann, P.J. and Pons M., J. Phys. D: Appl. Phys. 2007, 40, 6150-6158

[1-30] Kusunoki Kazuhiko, D thesis: Nagoya University, 2014, Chapter 1, pp 13.

[1-31] Tairov, Y.M.; Tsvetkov, V., Semiconductor Compounds Aiv Biv, Handbook on Electrotechnical mterials., 1988, 3: 446-471.

[1-32] Lely, J.A., Ber. Deut. Keram. Ges., 1955, 32, 229-236.

[1-33] Tairov, M.Yu. and Tsvetkov, V.F., J. Cryst, Growth, 1977, 43, 209-212.

[1-34] Staubinger, T.L.; Wellmann P.J. and Winnnacker, A., Mater. Sci. Forum, 2011, 353-356, 33-36.

[1-35] Wellmann, P.; Desperrier, P.; Muller, R.; Straubinger, T.; Winnacker, A.; Baillet, F.; Blanquet, E.; Dedulle, J.M. and Pons, M., J. Cryst. Growth, 2005, 275, e555-e560.

[1-36] Straubinger, T.L.; Bickermann, M.; Weingaertner, R.; Wellmann, P.J.; and Winnacker, A. J. Cryst. Growth, 2002, 240, 177-123.

[1-37] Kushibe, M.; Ishida, Y.; Okumura, H.; Takahashi, T.; Masahara, K.; Ohno, T.; Suzuki, T.; Tanaka, T.; Yoshida, S. and Arai, K., Mater. Sci. Forum, 2000, 338-242, 169-172.

[1-38] Powell, J.A., Petit, J.B., Matus, L.G., NASA Technical Memorandum 104410, p.3.

[1-39] Yakimova, R.; Tuominen, M.; Bakin, A.S.; Fornall, J.O.; Vehanen, A. and Janzen, E., Inst, Phys, Conf. Ser., 1996, 142, 101-104.

[1-40] Rendakova, S.V.; Nikitina, I.P.; Stregubova, A. and Dmitriev, V.A., J. Electronic Materials, 1998, 27, 292-295.

[1-41] Elwell, D. and Scheel, H.J., Crystal from High-Temperature Solutions (New York: Academic), 1975.

[1-42] Kusunoki, K.; Munetoh, S.; Kamei, K.; Hasebe, M.; Ujihara, T. and Nakajima, K., Mater. Sci, Forum, 2004, 45, 123-126.

[1-43] Nishitani, S.R. and Kaneko, T., J. Cryst. Grwoth, 2008, 310, 1815-1818.

[1-44] Ikeda, M.; Hayakawa, T.; Yamagiwa, S.; Matsunami, H. and Tanaka, T., J. Appl. Phys. 1979, 50, 8215-8225.

[1-45] Ferro, G. and Jacquier, C., New J. Chem., 2004, 28, 889-896.

[1-46] Shinya, N., Hamaguchi, Y.; Yamagata, N.; MinowaT., Method for growing silicon carbide crystal, US20150159299 A1, 2015.

[1-47] Kusunoki Kazuhiko, Ph. D thesis: Nagoya University, 2014, Chapter 1, p. 31.

[1-48] Kimoto, T., Prog. Cryst. Growth CH., 2016, 62, 329-351.

[1-49] Hirth, J.P. and Lothe, J., Theory of Dislocations, 2nd Edition, John Wiley & Sons Publicaiotn, New York, 1982, pp. 60.

[1-50] Eshelby, J.D. and Stroh, A.N., Phil. Mag., 1951, 42, 1401-1405.

[1-51] Yi Chen, Defects Structures in Silicon carbide bulk crystals, epilayers and devices: Stony Brook University, 2008, pp. 17-21.

[1-52] Wu, F.; Dudley, M.; Wang, H.; Byrappa, S.; Sun, S.; Raghothamachar, B.; Sanchez, E.K.; Chung, G.; Hansen, D.; Mueller, S.G. and Loboda, M.J., Mater. Sci. Forum, 2013, 740-742, 217.

[1-53] Dudely, M.; Wu, F., Appl. Phys. Lett, 2011, 98, 232110.

[1-54] Hirth, J.P. and Lothe, J., Theory of Dislocations, 2nd Edition, John Wiley & Sons Publicaiotn, New York, 1982, pp. 78.

[1-55] Ohtani, N.; Katsuno, M.; Tsuge, H.; Fujimoto, T.; Nakabaashi, M.; Yashiro, H.; Sawamura, M.; Aigo, T. and Hoshino, T., J. Cryst. Growth, 2006, 286, 55-60.

[1-56] Nakamura, D.; Yamaguchi, S.; Gunjishima, I.; Hirose, Y. and Kimoto, T., J. Cryst. Growth, 2007, 304, 57-63.

[1-57] Tsuchida, H. Kamata, I. and Nagono, M., J. Cryst. Growth, 2007, 306, 254.

[1-58] Matsuhata, H.; Yamaguchi, H. and Ohno, T., Philosophical Magazine, 2012, 92, 4599-4617.

[1-59] Muzykov, P.; Bolotnikov, A. and Sudarshan, T., Solid-state Electronics, 2009, 53(1), 14-17.

[1-60] Muller, St.G.; Sanchez, E.; Hansen, D.M.; Drachev, R.D.; Chung, G.; Thomas, B.; Zhang, J.; Lobada, M.J.; Dudley, M.; Wang, H.; Wu, F.; Byrappa, S.; Raghothamachar, B. and Choi, G., J. Cryst. Growth, 2012, 352, 39-42.

[1-61] Dudley, M.; Byrappa, S; Wang, H.; Wu, F.; Zhang, Y.; Raghothamachar, B.; Choi, G.; Sanchez, E.; Hansen, D.; Drachev, R. and Loboda, M., MRS Proceedings, 2012, 29-34.

[1-62] Ha, S.; Mieszkowski, P.; Skowronski, M. and Rowland, L.B., J. Cryst. Growth, 2002, 244, 257-266.

[1-63] Nakamura, D.; Gunjishima, I.; Yamaguchi, S.; Ito, T.; Okamoto, A.; Kondo, H.; Onda, S. and Takatori, K., Nature, 2004, 430(7003), 1009-1012.

[1-64] Kusunoki, K.; Kamei, K.; Yashiro, N. and Hattori, R., Mater. Sci. Forum, 2009, 615-617, 137-140.

[1-65] Yamamoto, Y.; Harada, S.; Seki, K.; Horio, A.; Mitsuhashi, T.; Koike, D.; Tagawa, M. and Ujihara, T., Appl. Phys. Express , 2014, 7, 065501.

[1-66] Yamamoto, Y.; Harada, S.; Seki, K.; Horio, A.; Mitsuhashi, T. and Ujihara, T., Appl. Phys. Express , 2012, 5, 115501.

[1-67] Harada, S.; Yamamoto, Y.; Seki, K.; Horio, A.; Mitsuhashi, T.; Tagawa, M. and Ujihara, T., APL Mater., 2013, 1, 022109.

[1-68] Ujihara, T.; Kozawa, S.; Seki, K.; Alexander,; Yamamoto, Y. and Harada, S., Mater. Sci. Forum, 2012, 717-720, 351-354.

[1-69] https://en.wikipedia.org/wiki/CALPHAD.

[1-70] Kusunoki, K.; Kamei, K.; Okada, N.; Moriguchi, K. and Okada, N., Mater. Sci. Forum, 2011, 679-680, 36-39.

[1-71] Kusunoki, K.; Munetoh, S.; Kamei, K.; Hasebe, M.; Ujihara, T. and Nakajima, K., Mater. Sci. Forum, 2004, 45, 123-126.

[1-72] Danno, K.; Saitoh, H.; Seki, A.; Daikoku, H.; Fujiwara, Y.; Ishii, T. Sakamoto, H. and Kawai, Y., Mater. Sci. Forum, 2010, 645-648, 13-16.

[1-73] Daikoku, H.; Kado, M.; Sakamoto, H.; Suzuki, H.; Bessho, T.; Kusunoki, K.; Yashiro, N.; Okada, N.; Moriguchi, K. and Kamei, K., Mater. Sci. Forum, 2012, 717-720, 61-64.

[1-74] Kusunoki Kazuhiko, D thesis: Nagoya University, 2014, Chapter 1, p. 33.

[1-75] Kamei, K.; Kusunoki, K.; Yashiro, N.; Okada, N.; Tanaka, T. and Yauchi, A., J. Cryst. Grwoth, 2009, 311, 855-858.

[1-76] Dmitriev, V. and Cherenkov, A., J. Cryst. Growth, 1993, 128, 343-348.

[1-77] Tanaka, T.; Yashiro, N.; Kusunoki, K.; Kamei, K. and Yauchi, A., Mater. Sci. Forum, 2009, 600-603, 191-194.

[1-78] Seki, K.; Alexander; Kozawa, S.; Ujihara, T.; Chaudouet, P.; Chaussende, D. and Takeda, Y., J. Cryst, Growth, 2011, 335, 94-99.

[1-79] Kusunoki, K.; Kamei, K.; Okada, N.; Moriguchi, K. and Okada, N., Mater. Sci. Forum, 2011, 679-680, 36-39.

[1-80] Vodakov, Y.A.; Mokhov, E.N.; Roenkov, A.D. and Anikin, M.M., Sov. Tech. Phys. Lett., 1979, 5, 147.

[1-81] Harada, S.; Yamamoto, Y.; Seki, K. and Ujihara, T., Mater. Sci. Forum, 2013, 740-742, 189-192.

[1-82] Kusunoki Kazuhiko, D thesis: Nagoya University, 2014, Chapter 1, p. 38.

[1-83]Harada, S.; Yamamoto, Y.; Xiao, S.Y.; Tagawa, M.; Ujihara, T. Mater. Sci. Forum. 2014, 778, 67-70.

# Chapter 2 SiC growth by TSSG method

## 2.1 Introduction

In this chapter the mechanism and experiment details of TSSG method would be introduced. At first, the growth driving force and growth model are presented. Then, the growth apparatus and the growth process of TSSG method are described. Last, we would introduce the characterization techniques of SiC grown crystal.

In this research, SiC grown crystals were grown by TSSG method. The morphology of grown crystals was characterized by differential interference contrast microscope (DIC) and confocal laser scanning microscope (CLSM). Raman was used to identify the polytype of grown crystals. The dislocations behaviors were characterized by Synchrotron X-ray topography, Transmission Electronic Microscopy (TEM) and KOH etching.

## 2.2 The driving force of solution growth

Solution growth has long history and wide application. The basic mechanism is to dissolve the solute into solvent and make it achieve supersaturation. Then the crystal would recrystallize from the solvent. The solution is composed of solute, solvent and impurity. During the solution growth, the solvent is as the growth media and the solute is as the growth material. The solute dissolves into the solvent as molecules or atoms. Then the crystal with certain structure and properties would recrystallize from the solution. The solution usually include aqueous solution, melt or organic of inorganic solvent. When the material of crystal solubility is extremely low or the saturated vapor pressure is quite high, the addition of cosolvent could be helpful to control the solubility of the solute. [2-1]

Suppose there are element A and element B which would combine into compound AB. The chemical potential of A, B and AB in the solution are $\mu_A^L$ ,$\mu_B^L$ and $\mu_{AB}^S$ respectively.

The chemical potential is indicated as follow:

$$\mu_A^L = \mu_A^0 + kT \ln a_A \tag{2.1}$$

$$\mu_B^L = \mu_B^0 + kT \ln a_B \tag{2.2}$$

$$\mu_{AB}^S = \mu_{AB}^0 + kT \ln a_{AB} \tag{2.3}$$

where $\mu_A^0$, $\mu_B^0$ and $\mu_{AB}^0$ are the chemical potential (J/mol) of A, B and AB under standard condition respectively, the *k* is Boltzmann constant, the T is the temperature (K) and the *a* is activity (mol/L).

When the system is in equilibrium, there is formula (2.4):

$$\mu_A^L(a_{e,A}) + \mu_B^L(a_{e,B}) = \mu_{AB}^S \quad (2.4)$$

where $a_e$ is the activity in equilibrium system, $\mu_{AB}^S$ is the chemical potential of AB in solid.

When compound AB is produced, the chemical potential difference $\Delta\mu$ is written as:

$$\Delta\mu = \left(\mu_A^L(a_A) + \mu_B^L(a_B)\right) - \mu_{AB}^S \quad (2.5)$$

Substitute (2.4) into (2.5):

$$\Delta\mu = \left(\mu_A^L(a_A) + \mu_B^L(a_B)\right) - \mu_A^L(a_{e,A}) + \mu_B^L(a_{e,B}) = kT\ln\frac{a_A}{a_{e,A}} + kT\ln\frac{a_B}{a_{e,B}} \quad (2.6)$$

The activity of constituent $a_i$ is related to the mole fraction $x_i$ as:

$$a^i = \gamma_i x_i \quad (2.7)$$

Where, $\gamma_i$ is the activity coefficient.

If $\gamma_i$=1, the constituent should obey Raoult rule. In ideal solvent, both of the solute and solution should obey Raoult rule which means that $\gamma_A$=1 and $\gamma_B$=1. Then formula (2.6) could be expressed as:

$$\Delta\mu = kT\ln\frac{x_A}{x_{e,A}} + kT\ln\frac{x_B}{x_{e,B}} \quad (2.8)$$

We replaced the mole fraction with component concentration $C_i$, and the formula (2.8) could be written as:

$$\Delta\mu = kT\ln\frac{C_A}{C_{e,A}} + kT\ln\frac{C_B}{C_{e,B}} \quad (2.9)$$

where $C_i$ is the actual concentration of the solvent and $C_e$ is the equilibrium concentration. Both their units are mol/L.

For SiC solution growth, the solute is C and the solvent is Si. C dissolved into Si solvent and form solution. Thus, we could see Si as element A, C as element B and SiC as AB in formula (2.3).

The C solubility in pure Si solvent is proved to be below 0.01% which is small. [2-2] The Si solvent could be considered as infinite dilution which means that $x_{Si} \approx 1$. The change of Si solvent concentration could be ignored since that its change is really small. Therefore, formula (2.9) could be approximately written as: [2-3, 4]

$$\Delta\mu = (\mu_{Si}^L + \mu_C^L) - \mu_{SiC} = kT\ln\frac{C_C}{C_{e,C}} + kT\ln\left(1 + \frac{C_C - C_{e,C}}{C_{e,C}}\right) = kT\ln(1+\sigma) \approx kT\sigma$$

(2.10)

According to formula (2.10), $\sigma$ indicates the supersaturation and it could be written as:

$$\sigma = \frac{C_C - C_{e,C}}{C_{e,C}} = \frac{\Delta C}{C_{e,C}} \tag{2.11}$$

According to (2.11) we could see that in supersaturation solution $\sigma > 0$. Combining formula (2.10) $\Delta\mu > 0$ which means the crystal would grow. $\Delta\mu$ is as the driving force for the crystal growth. If the supersaturation of solution is higher the driving force $\Delta\mu$ would be greater.

## 2.3 Growth model

It is well know that steps as the incorporation sites for growth units are required by the crystal growth. In crystal growth, there are two kinds of step sources: spiral growth and 2D nucleation as shown in Fig. 2.1 (a) and (b) respectively. In Fig. 2.1 (a) if the screw dislocation intersects the crystal surface the discontinuous change in displacement would result in a step on crystal surface. The step would provide a preferred incorporation site for growth unit to bond. Considering that the step is immobile at the screw dislocation it would moves around the screw dislocation in a spiral form. [2-5] 2D nuclei also could apply steps for the growth as shown in Fig. 2.1 (b). When the critical nucleation size is achieved, the 2D nucleation can form and grow on crystal surface. There are steps could be applied around the 2D islands for crystal growth.

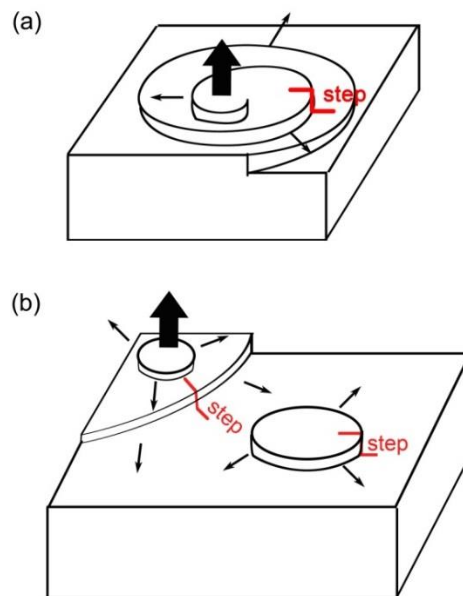


**Fig. 2.1** The step source from (a) spiral growth and (b) 2D nucleation.

## 2.3.1 Spiral growth

Fig 2.2 shows the spiral growth by threading screw dislocation. If the end of the screw dislocation is intersected with the crystal surface, a discontinuous displacement (step) would extend to the edge of crystal. The growth units attach to the kinks of the step and it will move to the right site as shown in Fig. 2.2(a). The step will curve around the emergency point of the threading screw dislocations with crystal surface shown as Fig. 2.2(b). As the growth continuing, the step would wind up into a spiral since the center (threading screw dislocation) is immobile Fig. 2.2 (c).

The spiral growth speed during solution growth would be discussed in this section. Here, ρ is the radius of curvature and the distance between step and step on the spiral is Λ. Λ is written as: [2-6]

$$\Lambda = 19\rho_C \tag{2.12}$$

where $\rho_C$ equals to the critical radius of 2D nuclei. Equation (2.2) is given by Cabrera and Levine by using approximate shape of spiral. When the spiral is the spiral of Archimedes there is:

$$\Lambda = 4\pi\rho_C \tag{2.13}$$

The vertical growth speed $R^{SP}$ could be written as:

$$R^{SP} = A\frac{\sigma^2}{\sigma_C}\frac{1}{\ln\left[\frac{d}{\pi a}\frac{\sigma_C}{\sigma}sinh\left(\frac{\sigma}{\sigma_C}\right)\right]} \tag{2.14}$$

$$\sigma_C = \frac{19\chi a^2}{\pi nkTd} \tag{2.15}$$

where $A$ is the rate constant, $d$ is the diffusion distance and $n$ is the numbers of threading dislocations. Formula (2.14) is the growth speed by spiral growth. When under low supersaturation ($\sigma \gg \sigma_C$) there is:

$$R^{SP} = A\frac{\sigma^2}{\sigma_C}\frac{1}{\ln\left[\frac{d}{\pi a}\right]} \propto \sigma^2 \tag{2.16}$$

On the other hand, when the high supersatruation ($\sigma \ll \sigma_C$) there is:

$$R^{SP} = A\sigma \propto \sigma \tag{2.17}$$

Which indicates that the speed of spiral growth is proportion to the square of $\sigma$ when $\sigma \gg \sigma_C$ while to $\sigma$ when $\sigma \ll \sigma_C$ is satisfied.

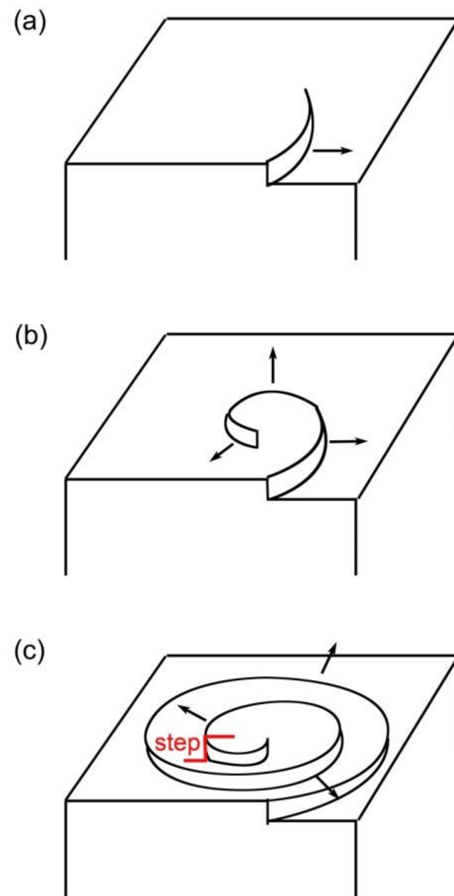


**Fig. 2.2** The spiral growth around threading screw dislocation. The end of the screw dislocation is intersected with the crystal surface; a discontinuous displacement (step) would extend to the edge of crystal. The growth units attached to the kinks of the step and it will move to the right site as shown in Fig. 2.2(a); The step will curve around the emergency point of the threading screw dislocations with crystal surface shown as Fig. 2.2(b). As the growth continuing, the step would wind up into a spiral since the center (TSD) is immobile Fig. 2.2 (c).[2-6]

## 2.3.2 2D nucleation

When the supersaturation reached to certain value, the atoms on the crystal surface would assemble together. When the critical 2D nuclei radius is achieved or over the 2D nucleation would form. The 2D nucleation is a kind of step source as we showed in section 2.3.1. In this section, we assume the situation is homogeneous nucleation. The change of critical energy of 2D nucleus formation is written as: [2-8]

$$\Delta G_2^* = \frac{\pi \chi^2 s_c}{\Delta \mu} \tag{2.18}$$

$$r_2^* = \frac{\chi^2 s_c}{\Delta\mu} \tag{2.19}$$

where $r_2^*$ is the critical radius of 2D nuclei, $\chi$ is the edge energy and $s_c$ is the area an atom occupied. $\Delta\mu$ is the difference of chemical potential when the crystal crystalize. Moreover, the rate of 2D nucleation $J_2$ is written as: [2-9]

$$J_2 = \omega_2^* \Gamma_2 C exp\left(-\frac{\Delta G_2^*}{kT}\right) \tag{2.20}$$

where $C$ is the density of saturated adsorption molecular, $\Gamma_2$ is Zeldovich factor.
Here,

$$\Gamma_2 = \frac{s_C}{\pi}\left(\frac{\Delta\mu}{s_C\chi}\right)^2\left(\frac{\Delta G_2^*}{4\pi kT}\right)^{\frac{1}{2}} \tag{2.21}$$

where $\omega_2^*$ is the frequency of attachment of molecules to the critical nucleus, formula (2.22) would be written as:

$$\omega_2^* = 2\pi\frac{s_c\chi}{a\Delta\mu} vCv_c exp\left(\frac{\Delta U}{kT}\right) \tag{2.22}$$

where $v$ is a frequency factor, $\Delta U$ is the energy of desolvation. The value of $\Delta G_2^*$ increases under low supersaturation. Thus the rate of nucleation $J_2$ becomes small and it is hard to nucleation. The nucleation would form once over the supersaturation. The growth rate of 2D nucleation $R^{nucl}$ is written as: [2-6]

$$R^{nucl} \cong a(J_2 v_\infty^2)^{\frac{1}{3}} \tag{2.23}$$

where $a$ is constant.

## 2.4 Experiment

In this section the experimental apparatus, raw materials, crucibles, rods, seed crystals, thermal isolation materials and atmosphere for SiC TSSG would be introduced. Then the temperature gradient measurement and experimental procedure would be described in details. Last the characterization methods would be presented.

### 2.4.1 SiC Growth apparatus

4H-SiC crystals were grown in an induction-heating furnace (NEV-SC35 Nisshin-Giken and NEV-SC100XY Nisshin-Giken) by the top-seeded solution growth method. The appearance of the induction-heating furnace (NEV-SC100XY Nisshin-Giken) and the illustration of the growth setup are shown in Fig. 2.3 (a) and (b)

respectively. The heating mode is high frequency induction heating. The frequency is during 15-50 kHz. The temperature distribution is determined by the relative position of crucible and coil and the temperature is controlled by power. The rotation patterns of upper rod and lower rod are CW, CCW and ACRT (Accelerated crucible rotation technique). The rotation speed could reach to 300 rpm max. The upper rod could move not only vertical direction but also horizontal direction. The cooling system is connected with stainless and indirectly cools the graphite rod.

Moreover, the furnace (NEV-SC35 Nisshin-Giken) and its illustration are shown in Fig. 2.4 (a) and (c) respectivly. The inner of the furnace is shown in Fig. 2.4 (b). The temperature is controlled by the thermal couple in the lower rod and the temperature distribution in crucible is changed by the susceptors. The different numbers of susceptor under crucible would results in different temperature distribution in the crucible. The rotation speed could reach to 200 rpm max. There are two thermal couples. One is inserted into the upper graphite rod to measure the solvent temperature. The other is inserted into the lower graphite rod and attached to the bottom of crucible. The upper rod and lower rod only could move vertical direction. The cooling system is connected with stainless and indirectly cools the graphite rod.

(a) Appearance

(b) Illustration

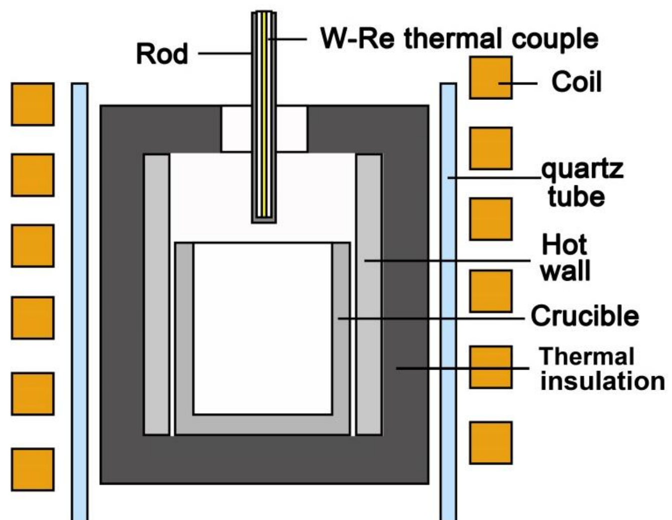


**Fig. 2.3** The furnace (NEV-SC100XY Nisshin-Giken) for SiC crystal high temperature solution growth (a) digital photography of appearance and (b) illustration of the inside view of furnace.

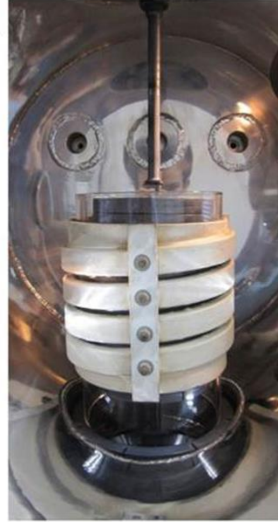


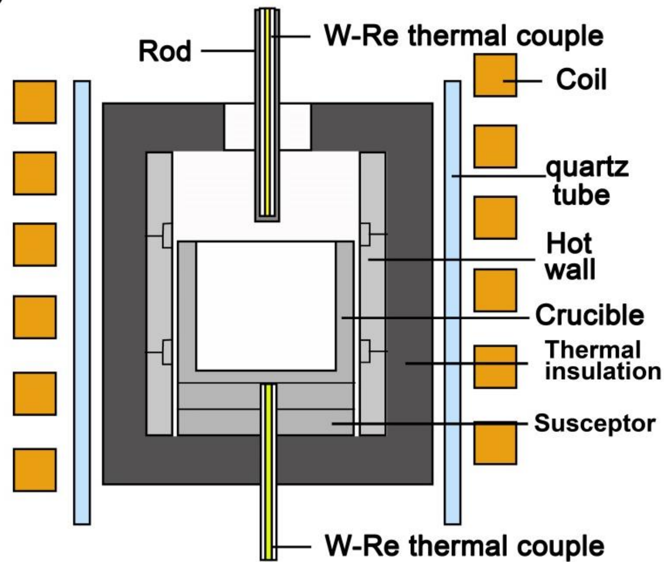


**Fig. 2.4** The furnace (NEV-SC35 Nisshin-Giken) for SiC crystal high temperature solution growth (a) digital photography of appearance and (b) inside view. (c) The illustration of the inside view of furnace.

## 2.4.2 Materials

### 2.4.2.1 Raw materials

Silicon (Si): In this study, chuck Si (polycrystal) with 11N (99.999999999%) is used

as raw materials for growth. They are made by Mitsubishi material. Si is putted in crucible and melted as the solution.

Titanium (Ti): The purity is 99.95% with Φ8-20 mm. They are made by Rare Metallic CO., LTD.

Aluminum (Al): The purity is 99.999%. They are made by NILACO CO., Ltd.

Chromium (Cr): The purity is 99.99% with Φ4-8 mm. The maker is Japan Metal Service.

### 2.4.2.2 Crucible, rod and seed crystal

(a) Crucible

Fig. 2.5 shows the sketch of graphite crucible which is used as container for Si and other additive. The inner radius is 45mm. The crucible material satisfies IGS-743KII (Nippon Techno-Carbon Co., Ltd). Crucibles supply C as source.

(b) Outer crucible with susceptor

Fig. 2.6 shows the illustration of graphite outer crucible which is used to apply susceptor for fix crucible since the crucible could not be used in furnace (NEV-SC100XY Nisshin-Giken). The outer crucible material satisfies IGS-743KII (Nippon Techno-Carbon Co., Ltd).

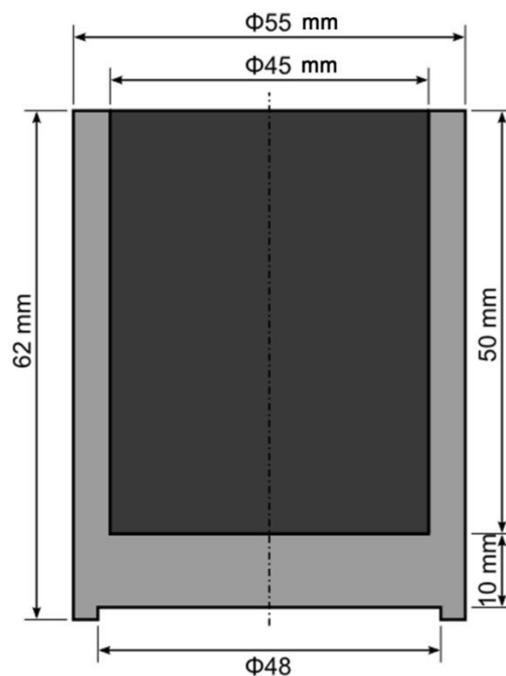


**Fig. 2.5** The illustration of graphite crucible.

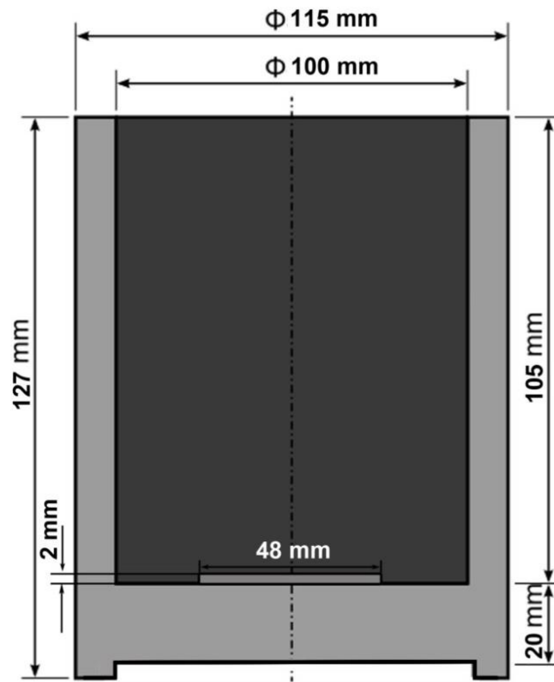


**Fig. 2.6** The illustration of outer graphite crucible with susceptor.

(c) Graphite rod

The sketch of graphite rod is shown in Fig. 2.7. The rod material satisfies IGS-743KII (Nippon Techno-Carbon Co., Ltd). Seed crystal would be attached with the end of the rod.

(d) Graphite adapter

In order to attach seed and rod together, graphite adapter was used. The graphite adapter material satisfies IGS-743KII (Nippon Techno-Carbon Co., Ltd). The graphite adapter was cut into the same size with seed crystal (10×10 mm).

(e) Seed crystal

3-inch 4H-SiC wafers (made by SiCrystal company German) made by sublimation method were used as seed crystals in this study. 2° and 4° off-axis wafers were used. The size of seed crystal is 10×10 mm. Both Si face and C were conducted CMP process. The thickness of seed crystal was about 0.35-0.36 mm.

(f) Three arms holder

Except attaching seed crystal to rod directly, three arms holders also were used as seed holder in this study. The sketches of arm and holder are shown in Fig. 2.8 (a) and (b) respectively. The graphite parts satisfy IGS-743KII (Nippon Techno-Carbon Co., Ltd).

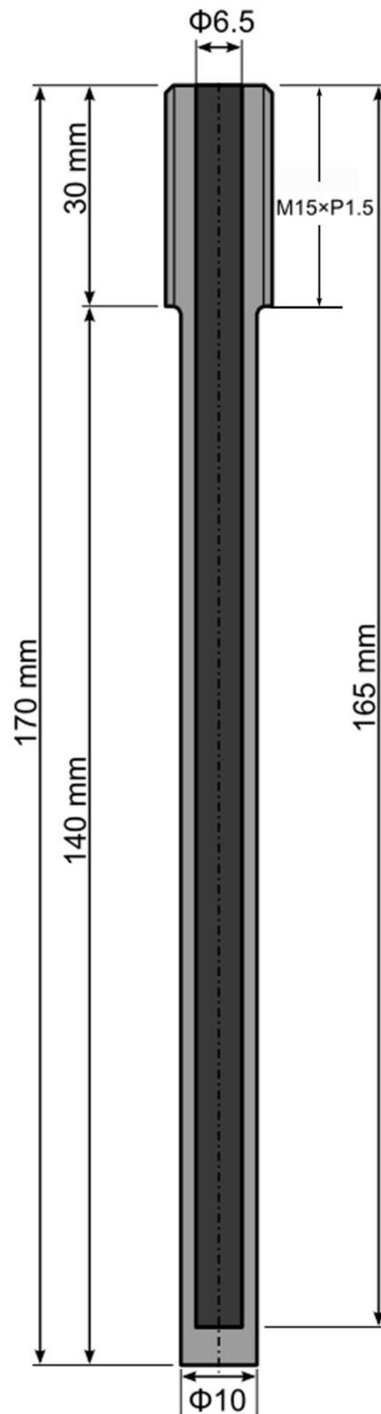


**Fig. 2.7** The illustration of graphite rod used in experiment.

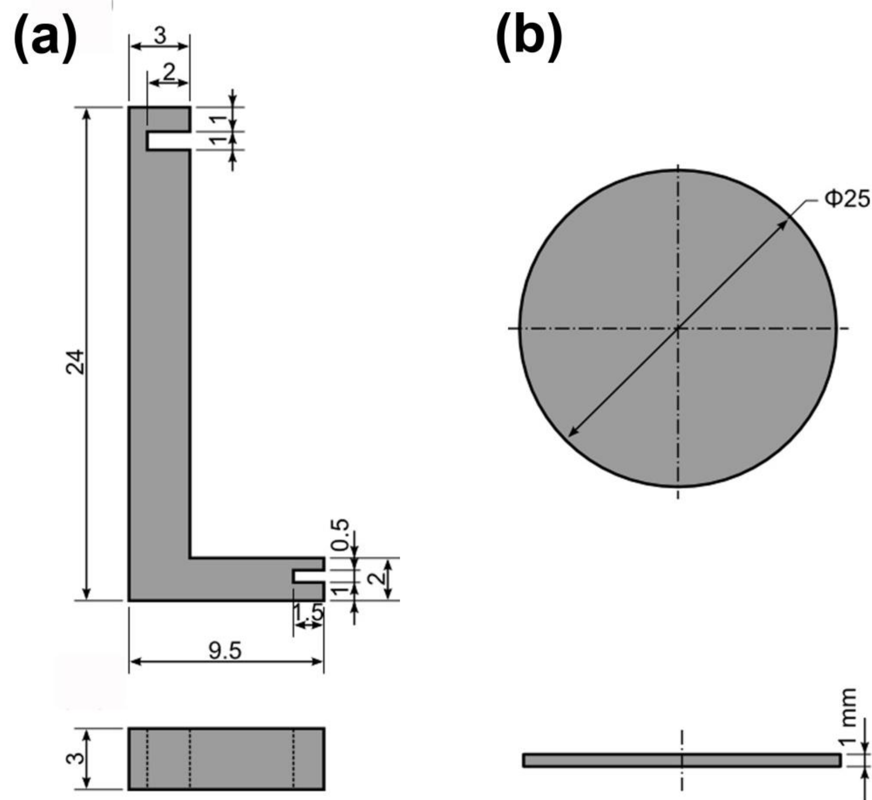


**Fig. 2.8** The illustration of parts which comprise 3 arms holder: (a) arm and (b) round graphite plate.

### 2.4.2.3 Thermal isolation materials

In this study, carbon thermal isolation materials were used to assist controlling temperature distribution in crucible. Thermal isolation materials were located between hot wall and crucible. Thermal isolation materials are sponge carbon (DON1000、Sankyou Carbon Co. Ltd).

### 2.4.2.4 Atmosphere

During growth helium (He) (99.999995%) (Japan Fine Products Co. Ltd) is full of chamber.

## 2.4.3 Temperature distribution measurement

The temperature distribution measurement was conducted before growth. The

temperature distribution was measured with Pure Si solvent. Clear Si was putted into a crucible and set into furnace. 3.0 mol Si (about 84.27g) was used. The temperature in Si solvent was measured by the upper thermal couple. The measured position was along the center of crucible with vertical direction at several spots.

### 2.4.4 Preparation before growth

#### 2.4.4.1 Clean of raw materials

In order to remove the oxide layer or organic contamination on raw materials or seed crystals surface, cleaning before growth is crucial. The detail is described as below:

(1) Clean raw materials or seed crystals by ultrasonic cleaning with deionized water (18MΩ•cm) for 1 min;

(2) Clean raw materials or seed crystals by ultrasonic cleaning with methanol (99.8%) for 1 min;

(3) Clean raw materials or seed crystals by ultrasonic cleaning with acetone (99.7%) for 1 min;

(4) Clean raw materials or seed crystals by ultrasonic cleaning with methanol (99.8%) for 1 min;

(5) Repeat step 1 to 4 once respectively;

(6) Immerse raw materials (except Ti) or seed crystals in to hydrofluoric acid (HF) (46%) for 20s;

(7) Flush raw materials or seed crystals with deionized water (18MΩ•cm) for 5 min;

(8) Dry raw materials or seed crystals with $N_2$.

(9) Preserve raw material and seed crystals under vacuum condition until conducting growth.

#### 2.4.4.2 Baking crucible

In order to remove the impurity, crucibles should be baked before growth. Put crucibles into furnace and evacuate the chamber below 2 Pa. Fill furnace chamber with Ar and heat it to 1800 °C. Keep 1800 °C for 1h and cool down to room temperature.

### 2.4.4.3 The bonding method between seed and rod

Two methods were used in this study to bond seeds and rods during growth as shown in Fig. 2.9 (a) and (b). Carbon adhesive (ST-201、Nisshinbo) was used in this study. Two bonding method was described as below:

1. Bonding directly as shown in Fig. 2.9 (a):
   a. Apply carbon adhesive on the end of rod and paste a seed adapter (10×10 mm) on it.
   b. Apply carbon adhesive on the seed adapter and paste a carbon plate (10×10×1 mm) on the seed adapter.
   c. Apply carbon adhesive on the carbon plate and paste another seed adapter on the carbon plate.
   d. Apply carbon adhesive on the seed adapter and paste the seed crystal on the seed adapter. Push seed crystal for better bonding and excluding bubble in the adhesive by Teflon tweezers.
   e. Put the rod on hot plate and heat to 60 °C in 30 min and keep for 5h. Then increase temperature to 120 °C in 30 min and keep for 2h. Increase temperature to 160 °C in 30 min and keep for 2h. Increase temperature to 200 °C in 30 min and keep for 2h. Increase temperature to 250 °C in 30 min and keep for 5h. Increase temperature to 300 °C in 30 min and keep for 5h. At last cool down to room temperature.

2. Three arm holders as shown in Fig. 2.9 (b):
   a. Assemble 3 arms and a round carbon plate shown in Fig. 2.8 (a) and (b) respectively to the structure as illustrated in inset lower left corner in Fig. 2.9 (b). Bond all these parts with carbon adhesive.
   b. Apply carbon adhesive on the end of rod and paste the 3 arms holder on it. Push them tightly together until exclude bubbles out.
   c. Put the rod on hot plate and heat to 60 °C in 30 min and keep for 5h. Then increase temperature to 120 °C in 30 min and keep for 2h. Increase temperature to 160 °C in 30 min and keep for 2h. Increase temperature to 200 °C in 30 min and keep for 2h. Increase temperature to 250 °C in 30 min and keep for 5h. Increase temperature to 300 °C in 30 min and keep for 5h. At last cool down to room temperature.

   Before growth, 3 arms holders need to be baked. The baking procedure is the same as crucible baking which is described in section 2.4.4.2.

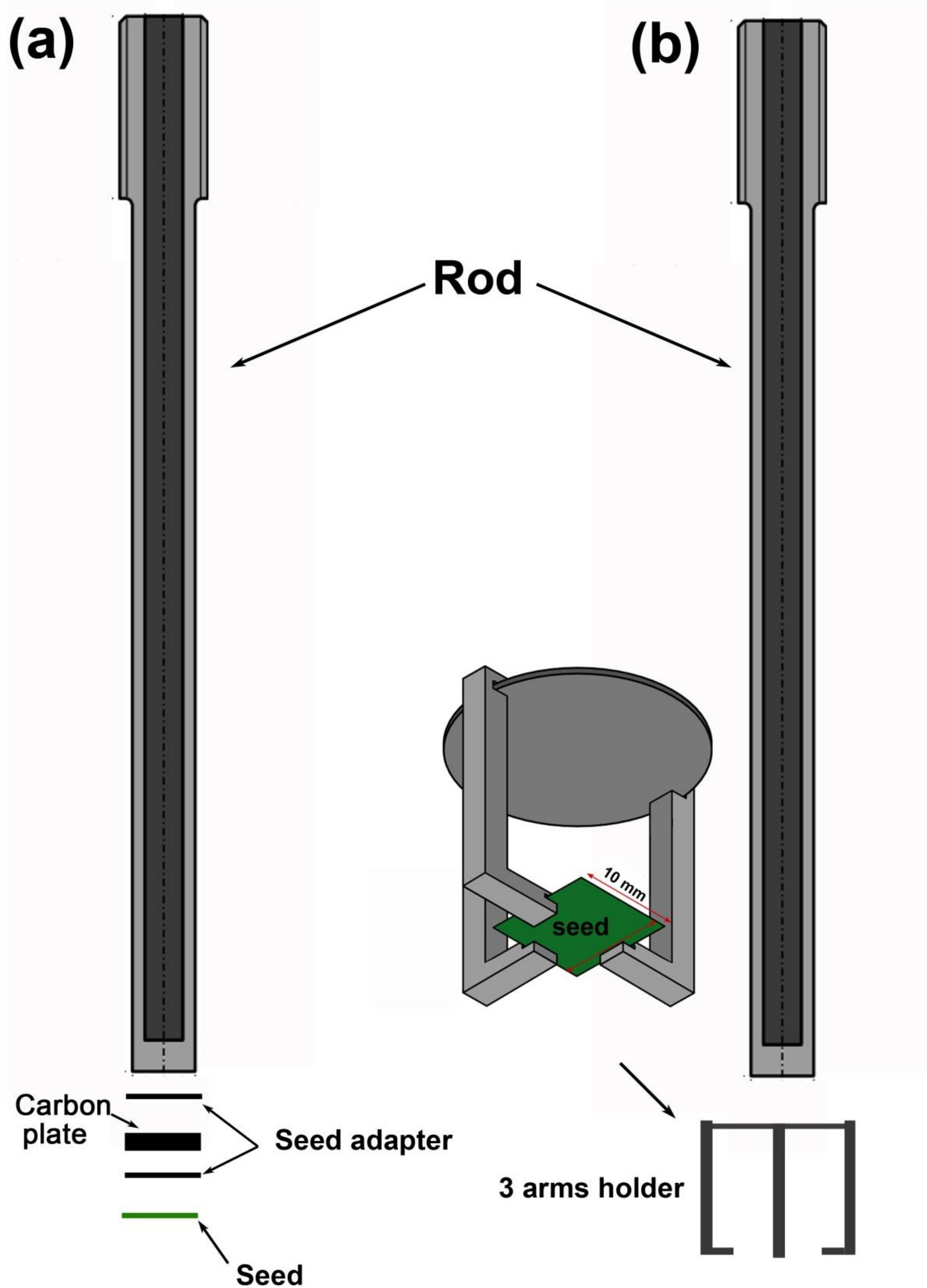


**Fig. 2.9** Two methods were used in this study to bond seed and rod during growth. (a) Attaching seed crystal to rod directly: Bond seed crystal, seed adapters, carbon plate and rod according to the sequence as shown in (a); (b) 3 arms holder: Assemble parts in Fig. 2.8 as the inset in (b) and attach it to the rod.

### 2.4.5 Growth procedure

Clear Si were putted into a crucible and set into furnace. 3.0 mol Si (about 84.27g) or other solvent component was used for growth or temperature distribution measurement. The rod was located at the upper rod of furnace. Evacuate the furnace chamber till below $1\times10^{-2}$ Pa. Then fill the chamber with He. The growth program could start. The detail of growth program is described in each chapter respectively.

### 2.4.6 Process after growth

#### 2.4.6.1 Removing residual Si solvent

In order to remove residual Si solvent on the grown crystal surface, immerse grown crystals into acid solvent (HF: $HNO_3$= 1: 2) for 12h. Then flush them with water for at least 6h.

#### 2.4.6.2 Removing rod

After removing residual Si solvent on the grown crystal, cutter (MC-201Y、Maruto instrument Co. LTD) was used to cut the rod to shorter length. Then put crystals into electric furnace (NHK-170、Nittokagaku Co. LTD) and heat to 1000 °C for 10h. After heating, there should be oxide layer on crystals surface. Immerse grown crystal into HF for 1min to remove the oxide layer and flush it for 5-7 min.

#### 2.4.6.3 Crystal cutting and polish

In order to observe the grown layer, polishing is necessary. At first, micro-cutter is used (MC-201Y、Maruto instrument Co. LTD) to cut the crystal into several mm pieces. Polish the cross-sectional face from #400 or #1000 diamond pad. Then diamond pad with 9 μm, 3 μm, 1 μm and 0.25 μm are used in order to conduct polish. After one side finished, turn over the sample and polish the other side with the same order. Polish the sample until the thickness decreases to about 200 μm. By using optical microscopy the seed crystal layer and grown layer could be identified. Moreover, the polytype could also be identified by different color.

### 2.4.7 Characterization

### 2.4.7.1 Differential interference (DIC) contrast microscopy

Differential interference contrast (DIC) microscopy (Leica, DM4000 M) is used to observe surface morphology and topography images of grown crystals in this study. It is also known as Nomarski interference contrast or Nomarski microscopy. [2-10] DIC works on the principle of interferometry to gain information about the optical path length of the sample. A polarized light source is separated by DIC into two orthogonally polarized mutually coherent parts which are spatially displaced (sheared) at the sample plane, and recombined before observation. By adding an adjustable offset phase determining the interference at zero optical path difference in the sample, the contrast is proportional to the path length gradient along the shear direction, giving the appearance of a three-dimensional accurate image. [2-11]

### 2.4.7.2 Confocal laser scanning microscopy

Confocal laser scanning microscopy (CLSM), is an optical imaging technique for increasing optical resolution and contrst of a micrograph by means of adding a spatial pinhole placed at the confocal plane of the lens to eliminate out-of-focus light. [2-12] It enables the reconstruction of three-dimensional structures from the obtained images by collecting sets of images at different depths within a thick object. The principle of confocal microscopy is shown in Fig. 2.10. In this study, CLSM was used to obtain step profile of grown crystals.

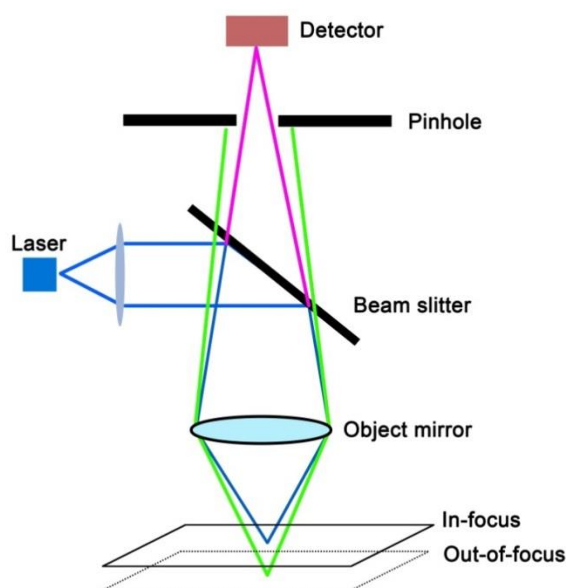


**Fig. 2.10** The principle drawing of Laser Microscropy

### 2.4.7.3 Raman spectroscopy

As we mentioned in the introduction, SiC exists in about 250 crystalline forms. Raman is the most effective way to identify the polytype of grown crystals. The illustration of Raman is shown in Fig. 2.11. When exiting light with frequency ν irradiates on the materials, the light would be scattered. The scattered light is composed of Rayleigh scattering with frequency ν which is the same as the exiting light and the Raman scattering. The frequency difference of Raman scattering and exiting light is the frequency of molecular vibration. [2-13] The method of determination of materials structure by analyzing the Raman scattering spectrum is called Raman spectroscopy.The illustration of Raman spectroscopy is shown in Fig. 2.11.

The Raman frequencies of the folded modes for 3C-SiC, 4H-SiC, 6H-SiC and 15R-SiC are shown in Table 2.1. [2-16] The FTA, FTO (Folded Transversal Optical), FLA and FLO (Folded Longitudinal Optical) modes are shown in Table 2.1.

In this study, Raman spectroscopy (in Via Raman microscope, Renishaw) was used to identify polytype of grown crystals. The wavelength is 532 nm and the power is 10 mW. The diameter of laser spot is 10 μm. During measurement, the center of Raman shift. was set to 1000 $cm^{-1}$ and the measuring range was from 40 $cm^{-1}$ to 1830 $cm^{-1}$. Usually, the characteristic peaks were used to identify polytypes. For 4H-SiC the characteristic peak is 204 $cm^{-1}$ and 610 $cm^{-1}$. For 6H-SiC the characteristic peak is 150 $cm^{-1}$ and for 15R-SiC is 173 $cm^{-1}$.

**Table 2.1The peak of Raman shift of the different SiC polytpes.**[2-16]

| Polytype | $x = q/q_B$ | Raman Shift [$cm^{-1}$] | | | |
|---|---|---|---|---|---|
| | | FTA | FTO | FLA | FLO |
| 3C-SiC | 0 | - | 796 | - | 972 |
| 4H-SiC | 0 | - | 796 | - | 964 |
| | 2/4 | 196, 204 | 776 | - | - |
| | 4/4 | 266 | - | 610 | 838 |
| 6H-SiC | 0 | - | 797 | - | 965 |
| | 2/6 | 145, 150 | 789 | - | - |
| | 4/6 | 236, 241 | - | 504, 514 | 889 |
| | 6/6 | 266 | 767 | - | - |
| 15R-SiC | 0 | - | 797 | - | 965 |
| | 2/5 | 167, 173 | 785 | 331, 337 | 932, 938 |
| | 4/5 | 255, 256 | 769 | 569, 577 | 860 |

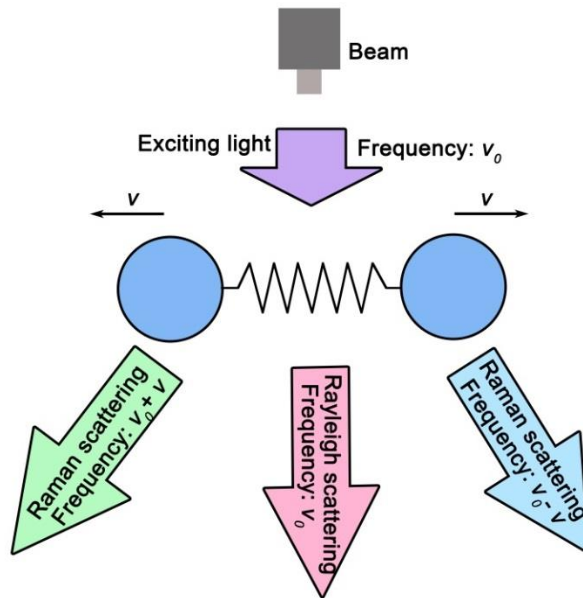


**Fig. 2.11** The principle drawing of Raman scattering**.**

### 2.4.7.4 Molten KOH etching

Defect selective etching by molten KOH is widely uses for the defect characterization of SiC single crystal. [2-17] In this study KOH etching was used to identify the location of defects in grown crystal. The procedure is described as follows:

1. Put 15g Potassium hydroxide (KOH) (purity 85%) into nickel crucible.
2. Put the crucible into electric furnace (MCK10-570、Motoyama Co. LTD) and heat it to about 520 °C. The temperature is measured by K-type thermocouples.
3. Put crystal into platinum (Pt) net and make sure the etching surface up.
4. Wait the temperature stable and put the Pt net into molten KOH for several minutes. The appropriate etching time should be investigated before etching samples by using substrates.

### 2.4.7.5 Synchrotron X-ray topography

Synchrotron x-ray topography in our studies was done at the High Energy Accelerator Research Organization (KEK) Japan (beamline BL-3C and BL-20B) and Aichi Synchrotron Radiation Center Japan (beamline BL8S2). Monochromatic x-ray topography was carried out. The X-ray beam from storage ring is monochromatized by two cooled parallel Si (111) crystals. The schematic experimental setting-up is shown in

Fig.2. 12. [2-18]

Commonly, there are three types of geometries are used for x-ray topography. The illustrations of the three geometries are shown in Fig. 2.13. Grazing-incidence (as shown in Fig. 2.13 (a)) is widely used in our studies due to the low penetration depth of x-ray beam, which is beneficial for the study of grown layer. The estimated penetration depth for the 1.50 Å is about 26 μm when the applied **g** vector equals to 11-28. Transmission geometry (also called Laue geometry) as illustrated in Fig. 2.13 (b) was also used in our studies to investigate the defects behavior in crystals. In the transmission mode, the x-ray beam passes through crystals and topography images would recorded on x-ray films. Fig. 2.13 (c) shows the back-reflection geometry. A large Bragg angle is used in this geometry. The back-reflection geometry is not used in our studies. The appearance of x-ray topography apparatus is shown in Fig. 2.14.

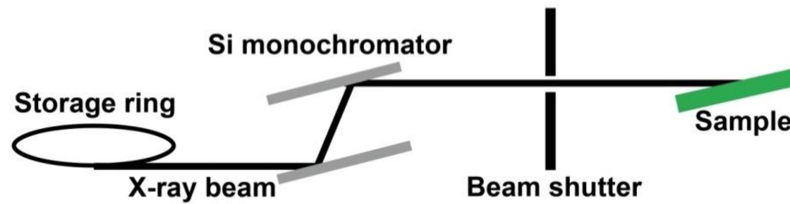


**Fig. 2.12** Schematic showing the experiment setting-up of synchrotron X-ray topography.

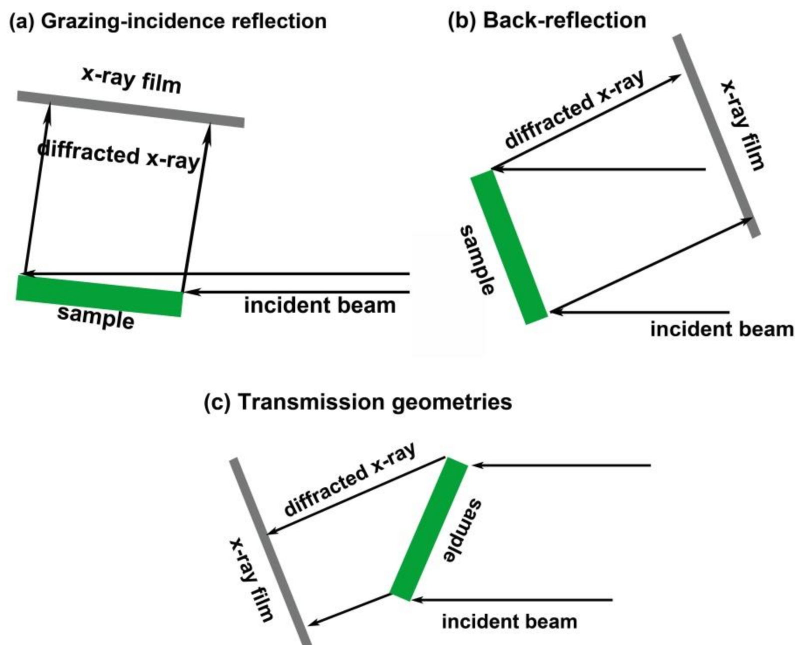


**Fig. 2.13** The illustration of (a) grazing-incidence reflection, (b) back-reflection and (c) transmission geometries used in this experiment.

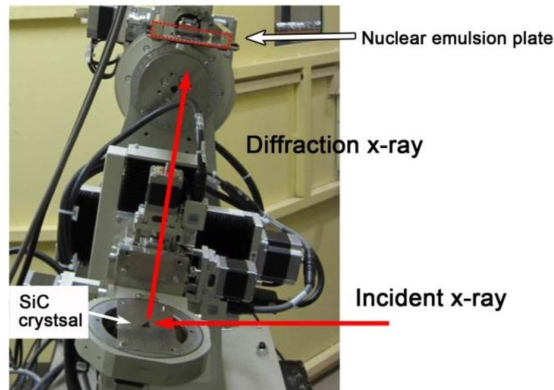


**Fig. 2.14** The appearance of working stage setup at BL15C in the Photon Factory, JAPAN.

## 2.4.7.6 Transmission Electronic Microscopy

Transmission electron microscopy (TEM) is a microscopy technique in which a beam of electrons is transmitted through an ultra-thin specimen, interacting with the specimen as it passes through it. An image is formed from the interaction of the electrons transmitted through the specimen. Then image is magnified and focused onto an imaging device. [2-19] The schematic of TEM is shown in Fig. 2.15.

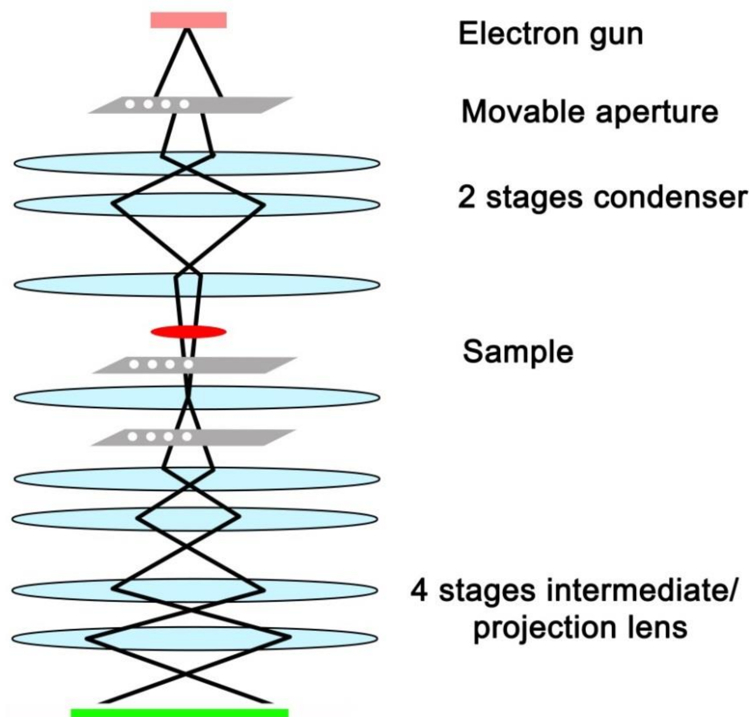


**Fig. 2.15** The principle drawing of Transmission electron microscopy (TEM).

The TEM observation samples were fabricated by Focused Ion Beam (FIB) and Ion milling. FIB (FB-2100, Hitachi) used in this study belongs to High voltage electron microscope laboratory Nagoya University. TEM (H-800, Hitachi) also belongs to High voltage electron microscope laboratory Nagoya University. The observation was conducted by accelerate voltage 200 kV.

### 2.4.7.7 Scanning transmission electron microscopy

A scanning transmission electron microscope (STEM) is a type of transmission electron microscope (TEM). However, STEM is distinguished from conventional transmission electron microscopes by focusing the electron beam into a narrow spot which is scanned over the sample in a raster. The rastering of the beam across the sample makes these microscopes suitable for analysis techniques such as energy dispersive x-ray (EDX) spectroscopy and annular dark-field imaging (ADF). All these information could be obtained simultaneously allowing direct correlation of image and quantitative data. [2-20, 21]

In this study, the step structure on crystal surface and SF atomic structure observation was conducted by JEOL EM-10000BU which belongs to High voltage electron microscope laboratory Nagoya University

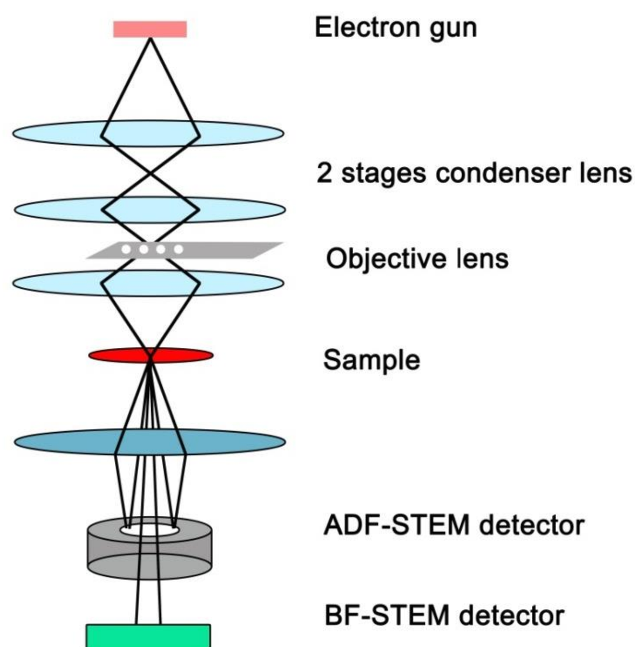


**Fig. 2.16** The principle drawing of scanning transmission electron microscope (STEM).

## 2.5 Conclusion

In this chapter, at first we introduced about the driving force of solution growth. Supposing melt Si as solvent, the difference between the solubility of solute C and dissolved C (as called supersaturation) becomes the driving force of SiC solution growth. During solution growth, both spiral growth and 2D nucleation could apply steps for growth. The growth rate of spiral growth and 2D nucleation was introduced.

The details of TSSG solution growth was introduced in this chapter, including the growth apparatus, the preparation before growth, the growth procedure, the process after growth and the characterization methods.

# Reference

[2-1] Smith, P.E. and Mazo, R.M., J. Phys. Chem. B, 2008, 112(26), 7875-7884.

[2-2] Yanaba, K.; Akasaka, M.; Takeuchi, M.(zhu 132)

[2-3] Markov. I.V., CRYSTAL GROWTH FOR BEGINNERS (World Scientific, Singapore, 2nd Edition, 2003) Chapter 1.

[2-4] Berg, W.F., Proceedings of the royal society A, 1938, 164, 79-95.

[2-5] Frank, F.C., Discuss. Faraday Soc., 1949, 5, 48-54.

[2-6] Seki K., Control of polytype and double position defect during the solution growth of 3C-SiC, Ph. D thesis: Nagoya University, 2013.

Nagoya: Nagoya University Ph. D. Thesis. 2013.

[2-7] Markov, I.V., CRYSTAL GROWTH FOR BEGINNERS (World Scientific, Singapore, 2nd Edition, 2003) Chapter 3..

[2-8] Nehrke, G., Nucleation and growth of crystals from solution, 2007, Chapter 2, pp. 11-14.

[2-9] I. V. Markov, CRYSTAL GROWTH FOR BEGINNERS (World Scientific, Singapore, 2nd Edition, 2003) Chapter 2.

[2-10] Rosenberger, H., Differential Interference Contrast Microscopy, Springer, 1977, 19-104.

[2-11] https://en.wikipedia.org/wiki/Differential_interference_contrast_microscopy.

[2-12] https://en.wikipedia.org/wiki/Confocal_microscopy.

[2-13] Colthup, N.B.; Daly, H.L.; Wiberley, S.E., Introduction to infrared and Raman spectroscopy (Academic press, New York, 1975) Chapter 1.

[2-16] S. Nakashima and H. Harima, Phys. stat. sol. (a), 1997,162 , 39.

[2-17] Katsuno, M.; Ohtani, N.; Takahashi, Jun; Yashiro, H. and Kanaya, M., Jpn. J. Appl. Phys., 1999, 38, 4661-1665.

[2-18] Yi Chen, Defects Structures in Silicon carbide bulk crystals, epilayers and devices: Stony Brook University, 2008, pp. 25.

[2-19] https://en.wikipedia.org/wiki/Transmission_electron_microscopy.

[2-20] https://en.wikipedia.org/wiki/Scanning_transmission_electron_microscopy.

[2-21] http://www.nanoscience.co.jp/knowledge/TEM/knowledge01.html.

# Chapter 3 V-shaped defects during 4H-SiC solution growth

## 3.1 Introduction

It is well-known that defects in SiC have various deleterious effects on power device performances. [3-1, 2, 3] In order to realize the full potential of SiC power devices, the reduction of defects density becomes extremely crucial. Although many efforts have been done to decrease the density of defects, the dislocation density of thousands cm$^{-2}$ still exist in SiC grown crystals by PVT and CVD growth. [3-4, 5, 6, 7, 8]

Solution growth is a potential method to produce high quality crystals because the growth proceeds under the condition close to thermal equilibrium. [3-9] BPD density is markedly reduced by using on-axis seed crystal during solution growth. [3-10] The MPs exist in the seed crystal is terminated by utilizing solution growth. [3-11] In our previous researches, TSDs can be dramatically reduced by the conversion of the TSDs to defects on basal plane due to the overgrowth of macrosteps on the TSDs. As the growth proceeds, the defects on the basal planes are excluded due to extending along in-plane direction and consequently the ultrahigh-quality SiC grown crystals can be obtained. [3-12, 13, 14, 15, 16] Dislocations in seed crystals can be reduced by utilizing threading dislocation conversion behavior during solution growth.

On the other hand, there is little research about defects generated during growth. Micropipes were reported generated due to second phase generation especially C related inclusions during PVT growth. [3-17] Ohno et al. reported BPDs generation under high growth rate during CVD growth. [3-18] Defects on basal plane were observed generated as pair in CVD growth grown crystal. [3-19] Izumi et al. found in-grown stacking faults nucleated near the substrate/epilayer interface and area with increasing epilayer thickness in a triangular shape. [3-20]

Recently we discovered unidentified defects corresponding to V-shaped contrasts in X-ray topographic images of the crystals grown by 4H-SiC solution growth which may hamper the reduction of dislocations density. Moreover, we made clear that the new V-shaped defects are different from similar V-shaped defects in CVD layers. [3-21, 22, 23] In this chapter, we characterized the newly discovered V-shaped defects peculiar to the solution growth by synchrotron X-ray topography and transmission electron

spectroscopy (TEM) observation. To the best of our knowledge, this is the first report on the present type of defects which appearing the V-shaped topography contrasts during the 4H-SiC (0001) solution growth.

## 3.2 Experiment

### 3.2.1 Growth

Fig. 3.1 shows the cross-sectional view of the crucible and the temperature distribution profile. The experiments in this section were conducted by furnace (NEV-SC35 Nisshin-Giken). The temperature of the crucible bottom is higher than the solution surface and the temperature distribution is as shown in Fig. 3.1. Thus, the C is supplied by the crucible at the higher temperature part. The growth position is 2mm under solution surface. The $\Delta T$ was the temperature between the seed crystal and the crucible bottom. The temperature was controlled by the thermal couple which attached with the crucible bottom. The temperature distribution was measured with Pure Si solvent. The measured position was along the center of crucible with vertical direction. The red dash line indicates the temperature around the crucible bottom and they are obtained by extrapolation instead of measurement. Because it was dangerous to move the thermal couple in upper rod so close to the crucible bottom. Along the red dash line we assumed that the temperature distribution was constant even the temperature changed. The temperature at the growth position (2 mm below the solution surface) was 1700°C controlled by the lower thermal couple. Fig. 3.2 shows the growth sequence. The seed crystal was dipped into the solvent and keep at 10 mm under solvent surface to conduct the melt back process. After 10 min melt back process, the seed crystal would be pulled up to the position 2 mm under the solvent surface. The growth was conducted with pure Si solvent at 1700°C. The accelerated crucible rotation technique (ACRT) was used. Both the rotation speed of upper rod and crucible was 20rpm. After growth, the upper rod would be pulled up until disconnecting to the solvent. The temperature would decrease to 700°C in 1 hour and then cooling down to room temperature. The residual solvent was removed in HF and $HNO_3$ solution (HF: $HNO_3$ = 1: 2).

4H-SiC (0001) Si-face and (000-1) C-face (10 mm ×10 mm) crystals were used as seeds. The off angle was 4° and the off direction was [11-20]. The growth time was 10 min, 30 min and 60 min respectively. The atmosphere was high-purity (>99.9999 vol%) helium gas flow. The growth temperature was 1700°C and the temperature distribution at the growth position is 20°C/cm.

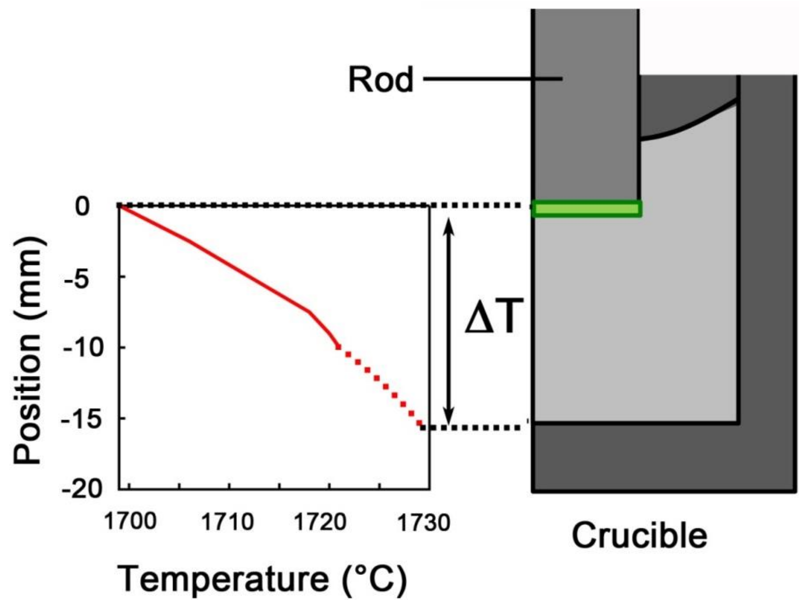


**Fig. 3.1** The illustration of temperature distribution of experiments in this section.

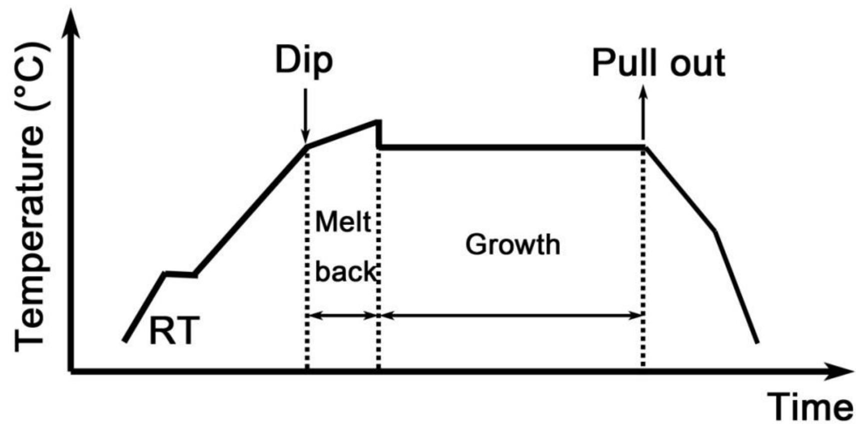


**Fig. 3.2** The growth procedure of experiment in this section.

### 3.2.2 Characterization

The morphology of grown crystals was observed by Nomarski microscopy. The defects were characterized by X-ray topography and KOH etching. The cross-sectional TEM samples were fabricated by Focus Ion Beam. The cross-sectional TEM observation was conducted by Hitach H-800 along the [11-20] direction.

## 3.3 Results and discussion

### 3.3.1 V-shaped generated defects

The in-plane X-ray topographic images taken from Si face grown crystal (60 min growth) is shown in Fig. 3.3. The knife shaped contrasts corresponding to defects on basal plane which were converted from TSDs in seed crystal were indicated by the green arrows. The blue arrows indicated the BPDs corresponding to oblique line contrasts. The BPDs were converted from TEDs in the seed crystal. The observation was consistent with our results before. [3-13] Moreover, two V-shaped contrasts indicated by the red arrows were observed. The magnified image of these two V-shaped contrasts was shown in Fig. 3.4 (b). Fig. 3.4(a) shows the identical position of seed crystal with (b).

Figure 3.4 shows in-plane X-ray topographic images recorded in grazing incidence g= 11-28 from the seed crystal (a) and the grown crystal (b) on the Si face. The white arrows at the upper left-hand side indicated projected directions of the vectors of incident X-ray on the crystal surface. The large white circular contrasts (A), relatively smaller circular white contrast (B) and line contrast (C) in Fig. 3.4 (a) corresponded to TSDs, TED and BPD, respectively. Magnified view of boxed area containing the TED (B) in Fig. 3.4 (a) is shown in the inset. The defects on basal plane (A') corresponding to asymmetric knife-shaped contrast extended from the position of the TSDs (A) in the seed crystal as shown in Fig. 3.4 (a). The TED (B') was propagated from the site (B) of the seed crystal. These behaviors of TSDs and TEDs are consistent with our previous studies.13 V-shaped contrasts of interest as indicated by D and E in Fig. 3.4 (b) was observed. Each of these V-shaped configurations comprised two symmetric line contrasts. The apexes of the V-shaped contrasts located at the up step direction and the "V" always open up towards the down step direction of the grown layer. By a comparison of Fig. 3.4 (a) and Fig. 3.4 (b), no defects were observed at the positions of the seed crystal corresponding to the apexes of the V-shaped defects. Therefore, it is sensible to assume the V-shaped defects are newly generated during the 4H-SiC solution growth instead of propagating or converting from defects in substrates.

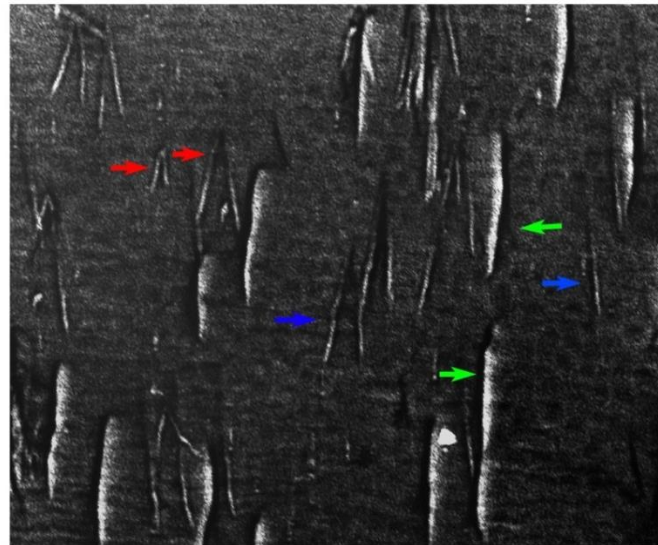


**Fig. 3.3** The in-plane X-ray topography of Si-face grown crystal. The red arrows indicated V-shaped defects. Defects on basal plane corresponding to knife shaped defects were indicated by green arrows. The blue arrows indicated basal plane dislocations corresponding to line contrasts.

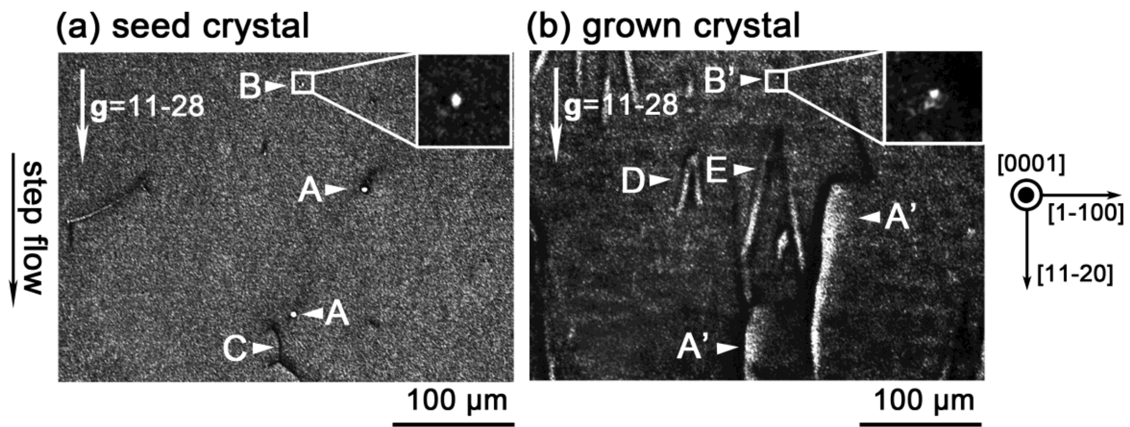


**Fig. 3.4** X-ray topographic images of the (a) seed crystal Si-face and (b) the crystal grown for 60 minutes taken at the identical position. Magnified view of boxed areas containing TED (B) and (B') in (a) and (b) is shown in the insets respectively.

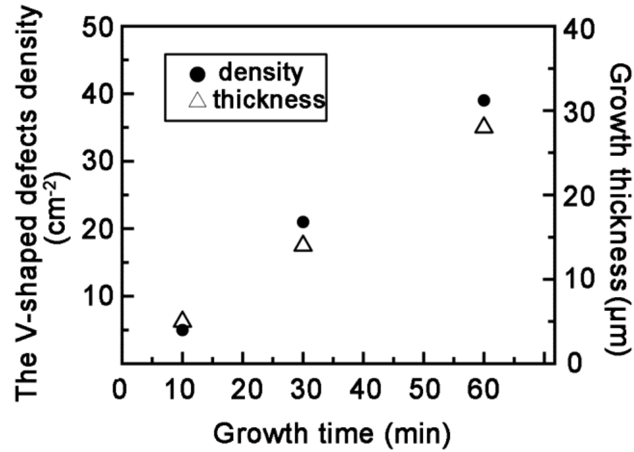


**Fig. 3.5** The growth time dependence of the V-shaped defects density and growth thickness**.**

The number of V-shaped defects was counted in whole area of each sample and the density of them was calculated. Fig. 3.5 summarizes the growth time dependence of the newly generated V-shaped defects density and growth thickness. The growth rate is almost the same since all the growth experiments were conducted under the same condition. The V-shaped defects density increased with the growth time on Si face growth. The linear increase of the density with time indicated that their generation rate was almost the same in each sample and they intermittently generate during growth process.

## 3.3.2 The Burgers vector of V-shaped defects

In order to identify the Burgers vectors of two branches of the V-shaped defects, X-ray topography images of the 10 minutes growth sample were taken at different Bragg conditions. Fig. 3.6 (a) and Fig. 3.6 (b) show the X-ray topography images of the grown crystal on Si face taken at different Bragg conditions **g**= 11-28 and 1-108 respectively. The white arrows in the upper-left-hand corners indicate the direction of the projection of the incident X-ray wave vectors onto the observed surface. When the conditions **g**·**b**=0 are satisfied, the contrasts of dislocations disappear. Here, **b** is the Burgers vectors of dislocations. Line contrasts corresponding to BPDs (B) in Figure 3.6 (a) with Burgers vector parallel to the [11-20] direction became invisible under the 1-108 reflection condition as indicated by B' in Figure 3.6 (b). The contrast of the V-shaped defects could be seen at the position of A as shown in Figure 3.6 (a), whereas the V-shaped defect contrast disappeared in the 1-108 reflection in Figure 3.6 (b).

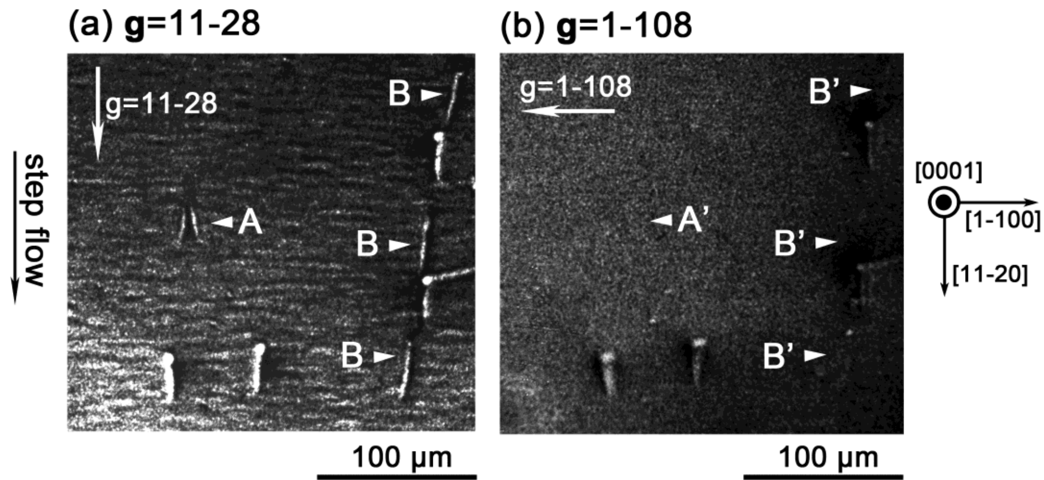


**Fig. 3.6** X-ray topography images of the grown crystal Si-face for 10 min taken at Bragg conditions: (a) g= 11-28 and (b) 1-108.

Disappearance of the contrast at the position of A' indicated that the V-shaped defect have Burgers vector parallel to the [11-20] direction, since it satisfied the condition $\mathbf{g}\cdot\mathbf{b}=0$. It was observed that two branches of each V-shaped contrast tilted counterclockwise and clockwise from step-flow direction respectively with certain angles. The BPDs deflecting direction from step flow direction were decided by their Burgers vectors properties. [3-21, 22] The burgers vectors must sum to zero if several branches of dislocations are connected to the same node in the crystal. Therefore it is reasonable to infer that two arms of each V-shaped defect has the same value and opposite direction burgers vectors. In addition, Zhang et al. reported that the tilt angles from step flow direction were affected by the $N_2$ doping concentration and the tilt angle increased with the $N_2$ doping concentration in CVD growth. In our case, the average tilt angle from [11-20] direction for each arm of V-shaped defects was about 8.5° and the $N_2$ doping concentration from background was $1.35\times10^{18}$ $cm^{-3}$ evaluated from the LOPC mode of Raman spectrum. These data were consistent with the results in the literature. [3-22] We concluded that the Burgers vector b of newly generated V-shaped defects was parallel to [11-20].

## 3.3.3 Microstructure of V-shaped defects

Similar V-shaped contrasts in X-ray topographic images also were reported by other researchers in 4H-SiC CVD growth. It is emphasized that all these V-shaped defects in the CVD crystal contain stacking faults between two branches of "V".[3-18, 19, 20] In order to characterize the newly discovered V-shaped defects in our case, TEM studies had

been conducted using [11-20] cross-sectional specimens. Firstly, a topographic image was obtained by incidence X-ray topography using 11-28 diffraction. Then etch pits were formed at the defects on 4H-SiC Si face by KOH etching at 520 °C for 3 minutes to identify the defects position. The etching pattern consisting of two shell-like shape pits indicated by white arrows were observed to be associated with the sites where the V-shaped defect intersected the surface as shown in Fig. 3.7 (b). The projected "height" d (shown as Fig. 3.7 (c)) of each V-shaped defects contrasts measured along the off-cut direction corresponds to the depth of the generation position. The distance d was estimated by the calculation as $d=L\times\tan\theta$, where $\theta$ was off-angle of the substrate and L was the length of contrasts along [11-20] direction as shown in Fig. 3.7 (a). In this case, the off angle θ was 4° and the length L of contrast was about 150 μm. According to calculation its generated position was about 10.5 μm under surface. FIB micro sampling technique was subsequently applied to prepare the TEM specimens for extracting the area between two branches of contrasts. The position of the FIB sample is shown as the white rectangle in Fig. 3.7 (a). The distance of the FIB sampling position was located at 70 μm from the end of the V-shaped branches. According to geographic analysis, if SFs were formed between the two branches of the V-shaped defect, we could observe any contrast at the depth of 5 μm from the surface in TEM image. The cross-sectional TEM image of FIB sample is shown in Fig. 3.7 (d). In the cross-sectional TEM image, no contrast is observed at the position about 5 μm under the surface. TEM results completed the data obtained by X-ray topography that there is no SF between two arms of the V-shaped defects. The microstructure of the newly generated V-shaped defects in our case was different from the V-shaped defects in the CVD crystals reported as Ref. 3-19 and 3-20 even they appearing similar topographic contrasts.

The illustrations of the V-shaped defects studied by other groups and us are summarized in Figure 3.8. One kind of the V-shaped defect mentioned was comprised of one or more overlapping Frank-type staking faults in the CVD layers. They were constituted of two partial dislocations with c-components of Burgers vector and the Frank-type staking faults as shown in Figure 3.8 (a). These V shaped defects were inferred to be generated by repetitive 2D nucleation of a single SiC bilayer at different atomic layers during epitaxial growth. The stacking sequence was distorted when steps overcame the 2D nucleation. [3-19] Another type of V-shaped defects is also observed in the CVD growth. [3-20] The threading portion of a once deflected threading dislocation in the substrate became the nucleation site of SF at the substrate/epilayer interface as illustrated in Fig. 3.8 (b). The formation mechanism was proposed on the basis of the overgrowth of the surface spiral steps associated with the surface intersections of

threading dislocations. They assumed that the nucleation site of V shape SF at the epilayer/substrate interface was the threading portion of a once deflected threading dislocation in the substrate. [3-20] The illustration of the V-shaped defects nucleated during the solution growth is shown in Fig. 3.8 (c). The newly generated V-shaped defects in our case were composed of two dislocations with Burgers vector parallel to [11-20] and no SF was observed between them. They were different from other V-shaped defects reported in the case of CVD growth. Considering that the both branches are generated from a same point suddenly, each V-shaped defect consists of a pair of defects on basal plane with opposite Burgers vector which generated simultaneously during the solution growth.

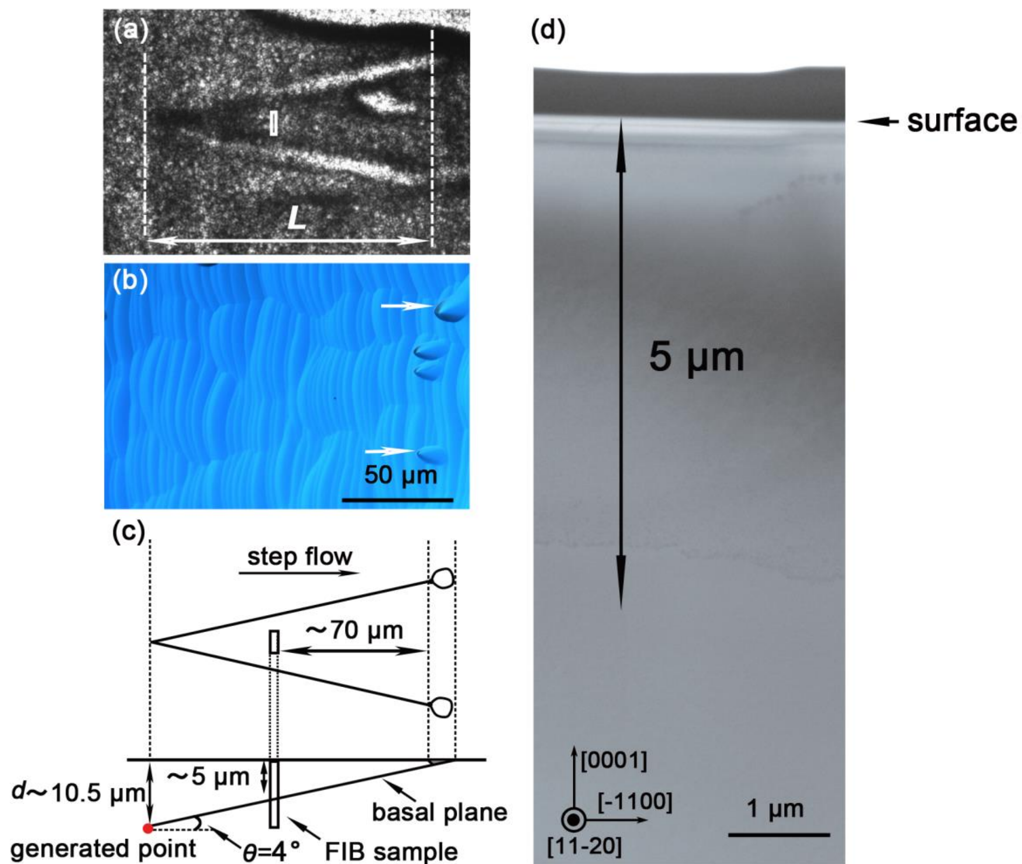


**Fig. 3.7** (a) In-plane X-ray topographic image and (b) optical microscopy image after KOH etching obtained from same areas on Si face. The FIB fabrication position is shown as white rectangle in (a). Two oval shaped etch pits indicated by white arrows in (b) correspond to the surface intersections of the two arms of V-shaped defects. (c) The geographic analysis model of FIB sample and schematic of etch pits shapes on an off-axis surface. The depth of the starting point of the defect is defined as $d=L\times\tan\theta$. (d) The cross-sectional TEM image of FIB sample.

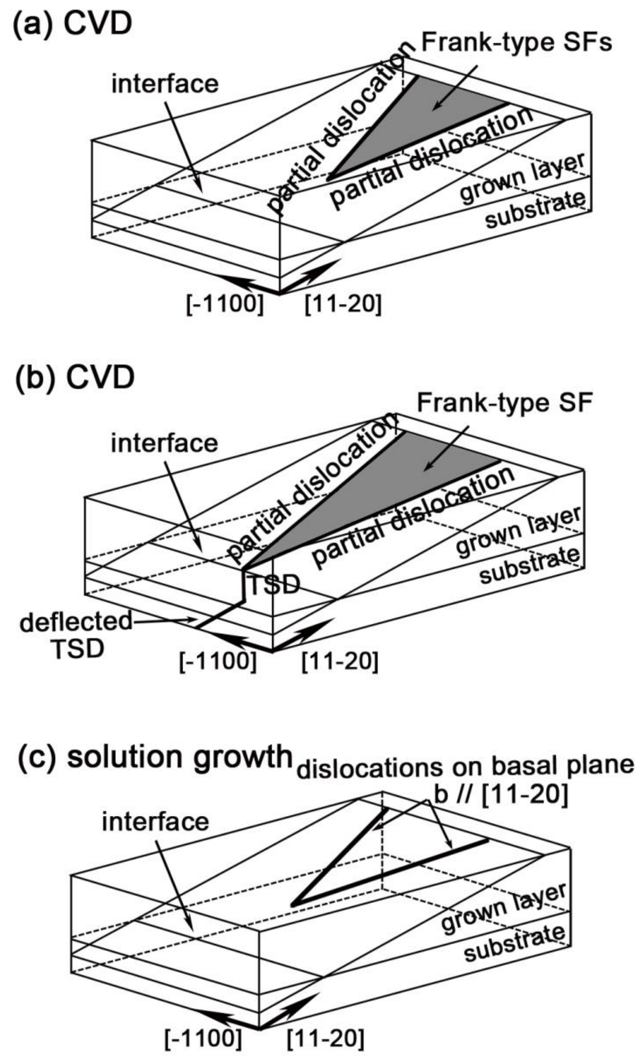


**Fig. 3.8** Illustrations of microstructure of V-shaped defects observed in (a) (b) CVD growth[19, 20] and (c) solution growth.

## 3.3.4 Generated mechanism

Fig. 3.9 shows the low magnification topographic image of C face grown crystal. No knife shaped contrasts corresponding to defects on basal plane which converted from TSDs in seed crystal were observed. The green circles indicated TSDs propagated from the seed crystal. Blue arrows indicated BPDs converted from TEDs in seed crystal. These results were consistent to our report before. [3-13] On the other hand, no V-shaped contrasts were observed on C face. The different polarity was assumed to result in the different defects behavior.

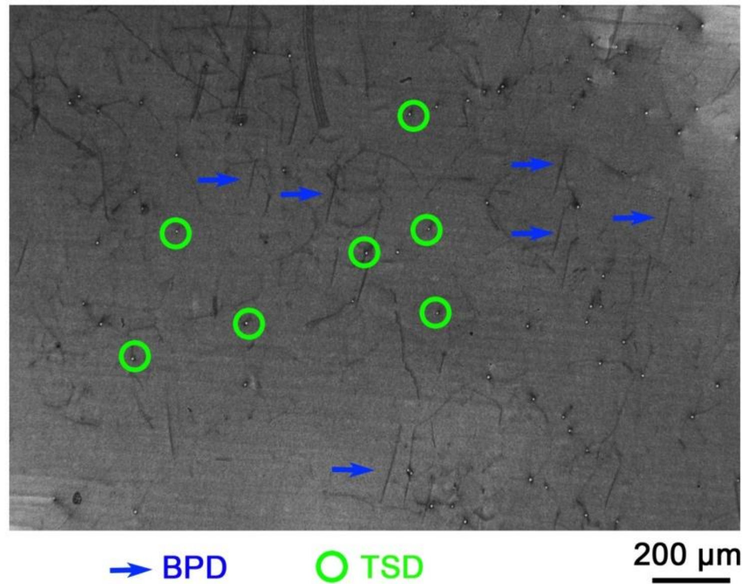


Fig. 3.9 The in-plane X-ray topography of C-face grown crystal. The green circles indicated TSDs propagated from seed crystal. No defects on basal plane corresponding to knife shaped defects were observed. The blue arrows indicated basal plane dislocations corresponding to line contrasts.

The formation mechanism of the present V-shaped defects was considered to be similar to the defect formation phenomenon in sublimation method reported by Sanchez et al.. They proposed that the nucleation of 2D islands during sublimation growth is responsible for the generation of threading dislocations. [3-23] They observed that threading edge dislocations were nucleated as pairs with opposite burgers vectors. A possible model for the V-shaped defects generation during solution growth was described as below. In this study, wide terraces were frequently observed on Si-face growth. When the supersaturation reached certain value it became easy for 2D nucleation to occur. Pairs of treading dislocations with same value but opposite direction burgers vectors would generated due to 2D islands. Threading dislocations would convert to dislocations on the basal plane appearing V-shaped contrasts just right after the formation due to macrosteps as our research before. [3-15] The converted BPDs would deflect and extend opposite side with each other from step-flow direction due to their opposite burgers vectors.

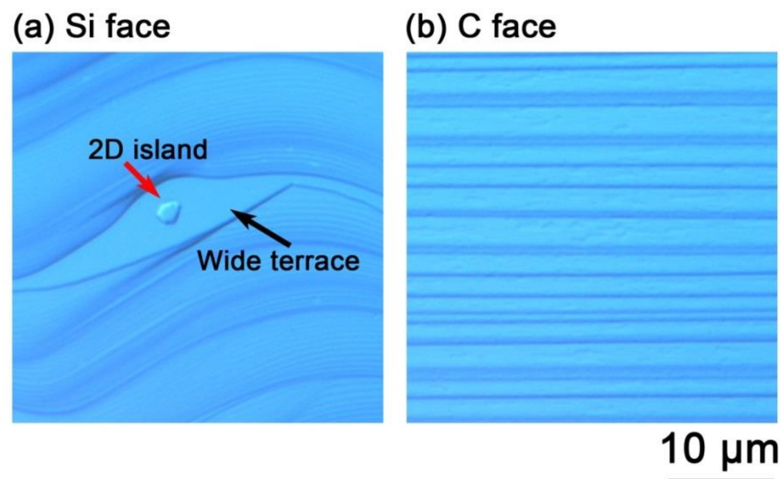


**Fig. 3.10** Nomarski images of the grown crystal surface on (a) Si face and (b) C face for 60 minutes growth. The white arrow indicates 2D island.

Fig. 3.10 shows morphology of grown crystal on (a) Si and (b) C face for 60 minutes growth. In Fig. 3.10 (a), the zigzag-shaped macrosteps were observed on the Si-face grown surface. Meanwhile, wide terraces can be observed on the crystal surface, most of them have the width about 10 μm. A 2D island on the wide terrace is indicated by arrow in Fig. 3.10 (a). On the other hand, we noted that no V-shaped defect was observed on the C face grown crystal. The grown morphology on C face (Fig. 3.10 (b)) is different from Si face. The C-face growth surface consisted of the ordered step trains and wide terrace like Si-face grown crystal surface were rarely observed. Based on our observation, 2D islands were rarely observed on C-face grown crystals. Therefore, it is also reasonable to attribute 2D islands to the formation of V-shaped defects. The C face growth can restrain the generations of V-shaped defects, which is benefit for the reduction of dislocations density.

## 3.4 Conclusion

X-ray topography revealed an unidentified defect during Si-face solution growth. This kind of defects appeared V-shaped contrasts in topography images. Topography contrasts analysis and cross-sectional TEM observation were conducted to determine the micro-structure of such kind of V-shaped defects and the probably mechanism was discussed. The conclusion is as follows:

- The V-shaped defects are comprised of a pair of dislocations on the basal plane. Each pair of dislocations with the opposite Burgers vector parallel to [11-20] direction was

proved to generate simultaneously.

- They are different from the V-shaped defects in CVD growth.
- A mechanism of generation of the V-shaped defects is proposed on a basis of the 2D nucleation islands on terrace.
- So far they only can be observed on Si face grown crystal during solution growth. Therefore, the C face growth can restrain the generation of V-shaped defects.

# Reference

[3-1] Matsunami, H.; Kimoto, T. Mater. Sci. Eng. R. 1997, 20, 125-166.

[3-2] Benamara, M.; Zhang, X.; Skowronski, M.; Ruterana, P.; Nouet, G.; Sumakeris, J. J.; Paisley, M. J.; O'Loughlin, M. J. Appl. Phys. Lett. 2005, 86, 021905.

[3-3] Yamashita, T.; Matsuhata, H.; Sekiguchi, T.; Momose, K.; Osawa, H.; Kitabatake, M. J. Cryst. Growth 2015, 416, 142-147.

[3-4] Skowronski, M.; Ha, S. J. Appl. Phys. 2006, 99, 011101.

[3-5] Senzaki, J.; Kojima, K.; Kato, T.; Shimozato, A.; Fukuda, K. Appl. Phys. Lett. 2006, 89, 022909.

[3-6] Yamamoto, K.; Nagaya, M.; Watanabe, H.; Okuno, E.; Yamamoto, T.; Onada, S. Mater. Sci. Forum 2012, 717, 477-480.

[3-7] Miyazawa, T.; Tsuchida, H. ECS J. Solid State Sci. Technol. 2013, 2, N3036-N3040.

[3-8] Shenai, K.; Dudley, M.; Davis, R. F. ECS J. Solid State Sci. Technol. 2013, 2, N3055-N3063.

[3-9] Tsuge, H.; Ushio, S.; Sato, S.; Katsuno, M.; Fujimoto, T.; Yano, T. Mater. Sci. Forum 2013,740, 7-10.

[3-10] Müller, St. G.; Sanchez, E. K.; Hansen, D. M.; Drachev, R. D.; Chung, G.; Thomas, B.; Zhang, J.; Loboda, M. J.; Dudley, M.; Wang, H.; Wu, F.; Byrappa, S.; Raghothamachar, B.; Choi, G. J. Cryst. Growth 2012, 352, 39-42.

[3-11] Quast, J.; Hansen, D.; Loboda, M.; Manning, I.; Moeggenborg, K.; Mueller, S.; Parfeniuk, C.; Sanchez, E.; Whitely, C. Mater. Sci. Forum 2015, 821, 56-59.

[3-12] Dost, S.; Lent, B. Single Crystal Growth of Semiconductors from Metallic Solutions; Elsevier: Amsterdam, 2007; pp 15-18.

[3-13] Yamamoto, Y.; Harada, S.; Seki, K.; Horio, A.; Mitsuhashi, T.; Ujihara, T. Appl. Phys. Express 2012, 5, 115501.

[3-14] Ujihara, T.; Kozawa, S.; Seki, K.; Alexander; Yamamoto, Y.; Harada, S. Mater.

Sci. Forum 2012, 717, 351-354.

[3-15] Harada, S.; Yamamoto, Y.; Seki, K.; Horio, A.; Mitsuhashi, T.; Tagawa, M.; Ujihara, T. APL Mater. 2013, 1, 022109.

[3-16] Harada, S.; Yamamoto, Y.; Xiao, S. Y.; Tagawa, M.; Ujihara, T. Mater. Sci. Forum 2014, 778, 67-70.

[3-17] Yamamoto, Y.; Harada, S.; Seki, K.; Horio, A.; Mitsuhashi, T.; Koike, D.; Tagawa, M.; Ujihara, T. Appl. Phys. Express 2014, 7, 065501.

[3-18] Yamashita, T.; Matsuhata, H.; Miyasaka, Y.; Odawara, M.; Momose, K.; Sato, T.; Kitabatake, M. Mater. Sci. Forum 2013, 740, 585-588.

[3-19] Wu, F. Z.; Wang, H. H.; Raghothamachar, B.; Dudley, M.; Chung, G.; Zhang, J.; Thomas, B.; Sanchez, E. K.; Mueller, S. G.; Hansen, D.; Loboda, M. J.; Zhang, L. H.; Su, D.; Kisslinger, K.; Stach, E. J. Electron. Mater. 2015, 44, 1293-1299.

[3-20] Wang, H. H.; Wu, F. Z.; Byrapa, S.; Yang, Y.; Raghothamachar, B.; Dudley, M.; Chung, G.; Zhang, J.; Thomas, B.; Sanchez, E. K.; Mueller, S. G.; Hansen, D.; Loboda, M. J. Mater. Sci. Forum 2014, 778, 332-337.

[3-21] Harada, S.; Yamamoto, Y.; Seki, K.; Horio, A.; Mitsuhashi, T.; Tagawa, M.; Ujihara, T. Acta Mater. 2014, 81, 284-290.

[3-22] Zhang, X.; Nagano, M.; Tsuchida, H. Mater. Sci. Forum 2012, 717, 335-338.

[3-23] Sanchez, E. K.; Liu, J. Q.; Graef, M. De; Skowronski, M.; Vetter, W. M.; Dudley, M. J. Appl. Phys. 2002, 91, 1143-1148.

# Chapter 4 TSD conversion behavior on C-face growth

## 4.1 Introduction

Recently, 4H-SiC C face bulk growth has attracted many attentions due to the difference to the Si face in many aspects such as doping efficiency, interfacial properties with other materials, electrical properties and so on.[4-1, 2, 3] C-face seed crystals are often used for stabling polytype during bulk growth. K. Kusunoki et al. reported the over 3 inch grown crystal was successfully obtained by SiC C face growth. [4-4] T. Mintani et al. also realized 2 inch grown SiC with 20mm thickness by utilizing C face growth. [4-5] Daikoku et al. successfully grown a 1-in. diameter 4H-SiC crystal with 30 mm thickness. [4-6] Moreover, as we discussed in chapter 3 C face growth was beneficial to reduce V-shaped defects generating during growth. We have reported a marked reduction of TSD density in 4H-SiC Si face grown crystal by utilizing high TSD conversion phenomenon during solution growth. [4-7] During SiC solution growth, TSDs in seed crystals would convert to defects on basal plane. Those defects on basal plane converted from TSDs in seed crystals are excluded from grown crystals due to extending along in plane direction as the growth proceeds. As a consequence, the ultrahigh quality SiC grown crystals can be obtained. However, the TSD density cannot be decreased on C face by utilizing TSD conversion phenomenon like Si face does during solution growth. The absence of macrosteps is attributed to the rare conversion phenomenon on C face growth. Thus the reduction of TSD density on C face growth is still a challenge. In addition, it is well known that the addition of Ti has been proved to increase step bunching process. [4-8] In this chapter, TSD conversion was realized by the formation of macrosteps on C face with Ti addition. Moreover, influence factor of the TSD conversion behavior were investigated in this chapter. At last, unidentified black line contrasts corresponding to partial dislocations were reported.

## 4.2 Experiment

### 4.2.1 Growth

The crystal growth was conducted with induction-heating furnace (NEV-SC35 Nisshin-Giken) as shown in section 2.4.1. Off-axis 4H-SiC (000-1) C-face and (0001)

Si-face (10 mm ×10 mm) crystals were used as seeds. The off angle was 2° and 4° and the off direction was [11-20]. Solvent pure Si, Si-1at%Ti, Si-5at%Ti and Si-20at%Ti were used as solvents respectively. 2° off substrates were used to obtain C-face grown crystals while 4° off substrates were used for Si-face growth. A graphite crucible was used to contain the solvent and as carbon source. The temperature at the seed crystal and the bottom of the crucible was measured by thermal couples. The growth temperature gradient was controlled by the relative position of crucible and the heat coil. The temperature gradient distribution is shown as in Fig. 4.1. Growth experiments were performed by keeping the seed crystal at 2 mm below the solvent surface under a high-purity (>99.9999 vol%) helium gas flow, where the temperature was at 1750 °C and the temperature gradient is about 20 °C /cm. The growth time was 1 hour. The Si for the solvents in experiments possesses a purity of 11N. The seed crystal was inserted into the 3 arms holder and attached to the end of a graphite rod. The growth procedure is described in Fig. 4.2. The crucible was maintained at 1750 °C for 1h to homogenize the raw material with the rotation of crucible. The crucible rotation speed is 20rpm. The seed crystal was dipped into the solvent and keep at 10 mm under solvent surface to conduct the melt back process. After 10 min melt back process, the seed crystal would be pulled up to the position 2 mm under the solvent surface. The growth was conducted at 1750°C. The accelerated crucible rotation technique (ACRT) was used. Both the rotation speed of upper rod and crucible was 20rpm. After growth, the upper rod would be pulled up until disconnecting to the solvent. The temperature would decrease to 700°C in 1 hour and then cooling down to room temperature. The residual solvent was removed in HF and $HNO_3$ solution (HF: $HNO_3$ = 1: 2).

### 4.2.2 Characterization

Synchrotron X-ray topography was carried out at the high-resolution X-ray diffraction station BL3C in the Photon Factory at the High-Energy Accelerator Research Organization and BL8S2 in Aichi Synchrotron Radiation Center, Japan. The monochromatic X-ray wavelength was 1.50 Å and the applied incident **g** vectors were {11-28}. Moreover, transmission geometry as indicated in Fig. 2.13 (c) section 2.4.7.5. The X-ray wavelength for transmission geometry was 0.87 Å and the applied **g** vectors were 11-20 and 1-100. The topography images were recorded on Ilford L4 nuclear emulsion plates. Transmission geometry was also used in this section. Specimens for cross-sectional TEM were prepared by ion milling except the crystal from Si-5at%Ti solvent which is not appropriate for ion milling due to the relatively low step density on

the surface. The specimen of grown crystal with Si-5at%Ti for cross-sectional TEM observation is fabricated by the Focus Ion Beam (FIB). In order to protect the surface from tungsten deposition during FIB fabrication, carbon coating was conducted before FIB fabrication. The cross-sectional TEM observation was conducted by JEOL EM-10000BU along the [1-100] direction. High-angle Annular Dark Field Scanning (HAADF) images were taken for TEM samples fabricatedts by ion-milling. Bright field images were taken for the FIB samples since the light emitted from the tungsten deposition layer would affect observation under dark field condition. Surface morphologies were observed with a differential interference contrast (DIC) microscope Leica DM4000M using a Nomarski-type prism.

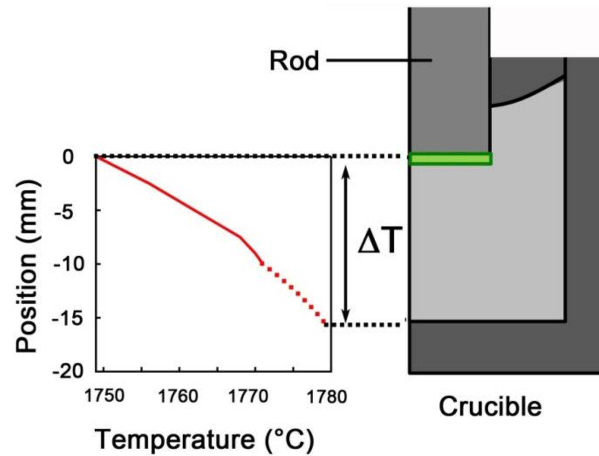


**Fig. 4.1** The illustration of temperature distribution of experiments in this section.

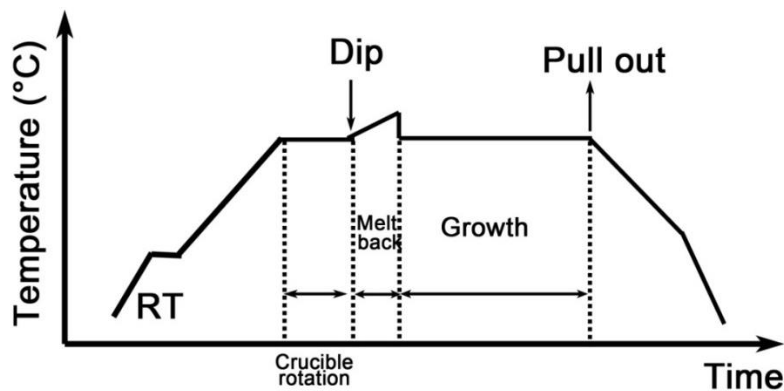


**Fig. 4.2** The growth procedure of experiment in this section.

## 4.3 Results and discussion

## 4.3.1 Morphology

Figure 4.3 shows Nomarski images and step profile of each SiC crystals grown from several solvents. The grown surface morphology indicated that SiC crystals grew via step-flow growth due to off axis seed crystals.

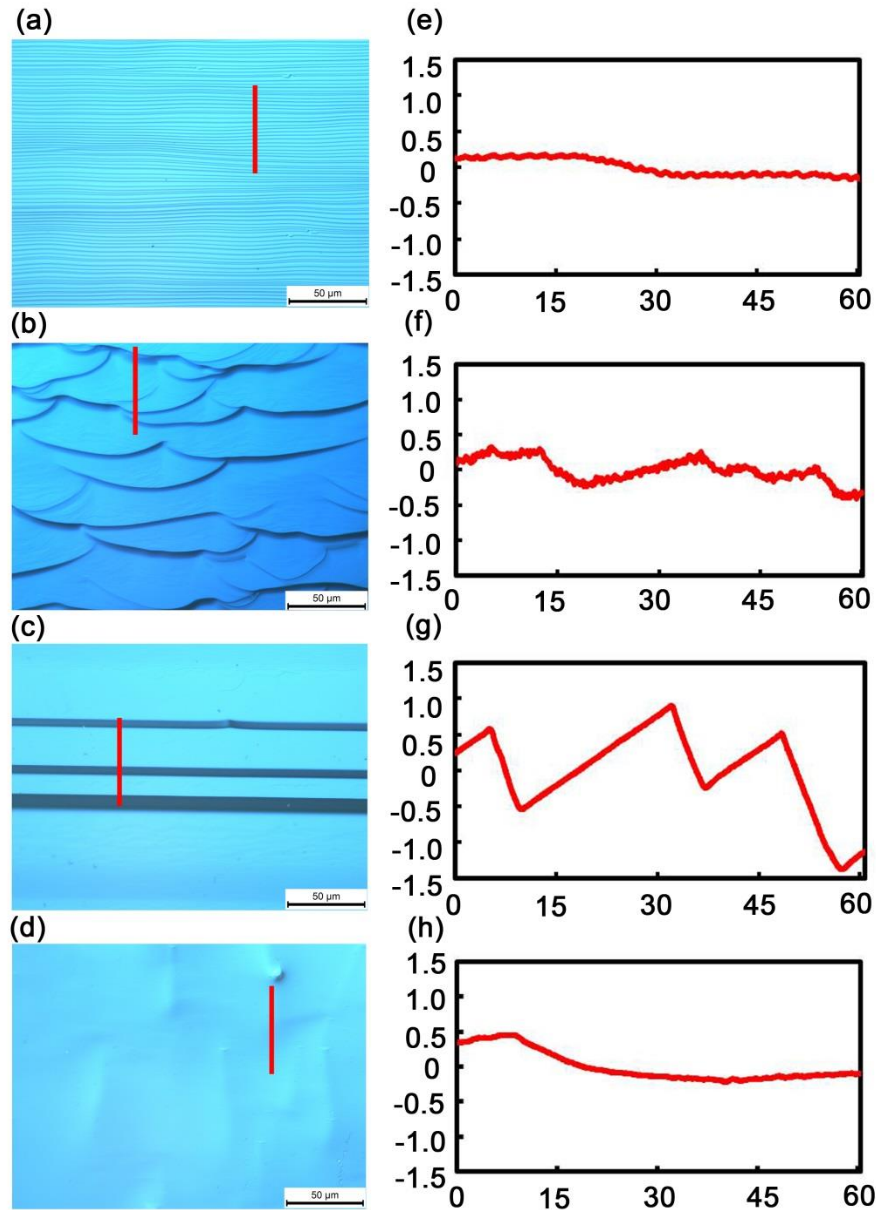


**Fig. 4.3** The Nomarski images of crystals grown with (a) pure Si (b) Si-1at%Ti solvent (c) Si-5at%Ti solvent and (d) Si-20at%Ti solvent. (e) (f) ( g) and (h) show step profiles conducted along the red lines in each corresponding Nomarski images at left side.

Figure 4.3 (a), (b), (c) and (d), clearly show that surface morphology of grown crystals depend on the concentration of Ti. The step bunching process increased with the addition of Ti. When the Ti addition reached to 5at%, wide terrace and straight steps were formed as shown in Fig. 4.3. The morphology profiles along the red line in Fig. 4.3 (a), (b), (c) and (d) are shown in (e), (f), (g) and (h) respectively. The step bunching process was promoted by the addition of Ti. When 1atTi% was added into the solvent, straight steps just became wondering. Giant macrosteps were observed when the addition of Ti from 0 to 5at%. The steps height was about above 1 μm. The giant steps disappeared and the surface became smoother than crystal grown from Si-5at%Ti solvent when 20at%Ti was added. Macrosteps were observed on the crystal grown from the solvent with Ti addition which is beneficial for the TSD conversion occurring.

### 4.3.2 The realization of TSD conversion on C face growth

Fig. 4.4 shown the topographic images of grown crystal with (a) pure Si, (b) Si-1at%Ti, (c) Si-5at%Ti and (d) Si-20at%Ti solvent. Knife shaped contrasts corresponding to defects on basal plane as indicated by red arrows were observed in Fig. 4.4 (c). The defects on basal plane were converted from TSDs in seed crystal as our reported before. [4-7] That indicated that TSDs conversion to defects on basal plane behavior were realized on C face growth.

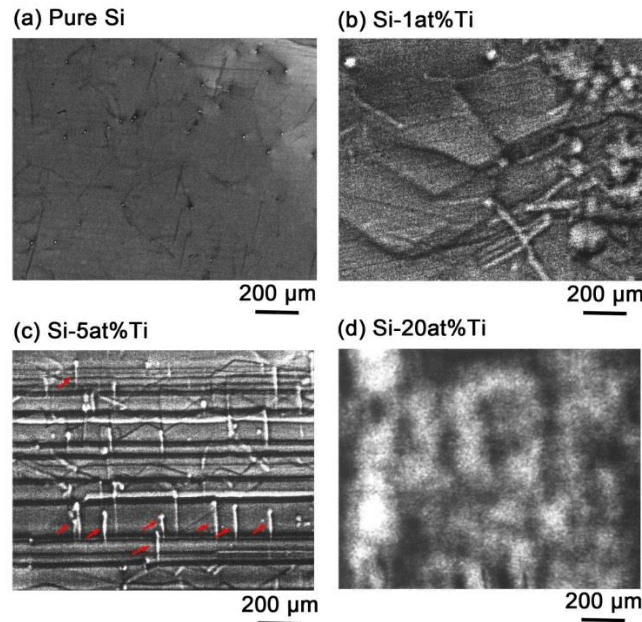


**Fig. 4.4** The in-plane X-ray topography of C-face crystals with (a) pure Si (b) Si-1at%Ti solvent (c) Si-5at%Ti and (d) Si-20at%Ti solvent.

On the other hand, no conversion was observed on samples grown with pure Si and 1at%Ti addition as shown in Fig. 4.4 (a) and (b). In addition, the topography image of crystal grown with Si-20at%Ti solvent was blurred. There was no valid information can be obtained.

Fig. 4.5 shows X-ray topography images of the 4H-SiC (000-1) C-face on the (a) (c) seed crystal and grown crystal with (b) pure Si and (d) Si-5at%Ti-C solvent at the identical position respectively. The large circular bright contrasts in topographic images correspond to TSDs. By a comparison of Fig. 4.5 (a) and (b), TSDs were still observed which indicated that TSDs propagated from substrate after growth with pure Si solvent. Contrary to this, knife-shaped contrasts (A') corresponding to SFs in Fig. 4.5 (d) extended from the positions of TSDs (A) in the seed crystal (Fig. 4.5 (c)), which indicated that TSDs converted to SFs after growth. The SFs contrasts align on the edge of the advancing steps which appeared as the black horizontal line contrasts in Fig. 4.5 (d). This indicated that the SF contrasts are extended by steps advancing. The TSD conversion was realized on C-face growth. This result convinces us that TSDs can be converted to SFs due to the formation of macrosteps.

We also noticed that TSDs indicated by B' in Fig. 4.5 (d) propagated from the substrate (Fig. 4.5 (c) B) instead of conversion to SFs. Harada et al. reported that nearly 100% TSDs in off-axis Si face substrate convert to SFs when the growth thickness achieves 10 μm during solution growth.[4-9] The numbers of TSD before and after growth was counted respectively and TSD conversion ratio was calculated for each sample.

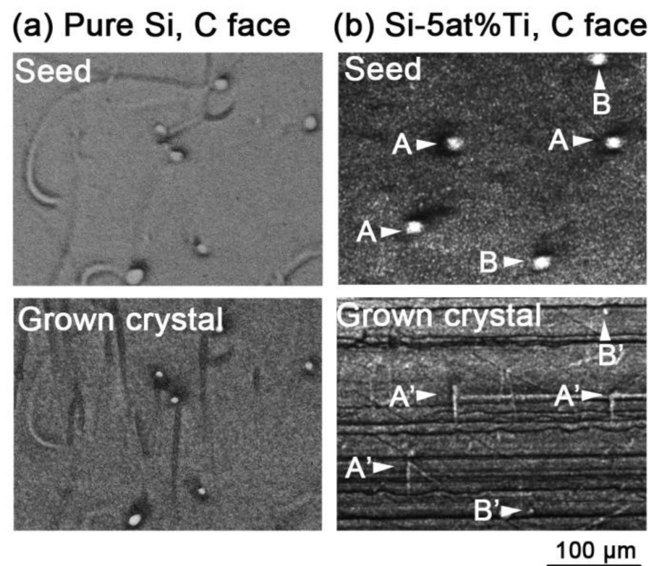


**Fig. 4.5** X-ray topography images of the 4H-SiC (000-1) C-face on the (a) (c) seed crystal and grown crystal with (b) pure Si and (d) Si-5at%Ti solvent respectively

Fig. 4.6 shows (a) Normaski image and (b) topographic image at the identical position of grown crystal with Si-5at%Ti solvent. The step flow direction is from upside to down side. The horizontal black line contrasts indicated by black arrow were contrasts caused by macrosteps. Defects on basal plane converted from TSD in seed crystal were observed as indicated by red arrows in Fig. 4.6 (b). Contrasts of defects on basal plane terminated at the edge of steps which indicated that TSDs in seed crystal were converted by macrosteps. Meanwhile white circle contrasts corresponding to TSDs propagated from seed crystal indicated by yellow circles were observed. Unlike Si face growth, the TSD conversion ratio is not 100% on C face crystal grown with Si-5at%Ti solvent. We counted the numbers of defects on basal plane which converted from TSDs in seed crystal and divided it by the total numbers of TSDs in seed crystal. Here we could obtain the TSDs conversion ratio on C face crystal with Si-5at%Ti solvent is 10%.

In this section, TSD conversion ratio increased 0 to 10% with 5at%Ti addition into the solvent. However the conversion ratio is still lower than that on Si face even the steps height is much higher. The possibility would be investigated in section 4.3.3.

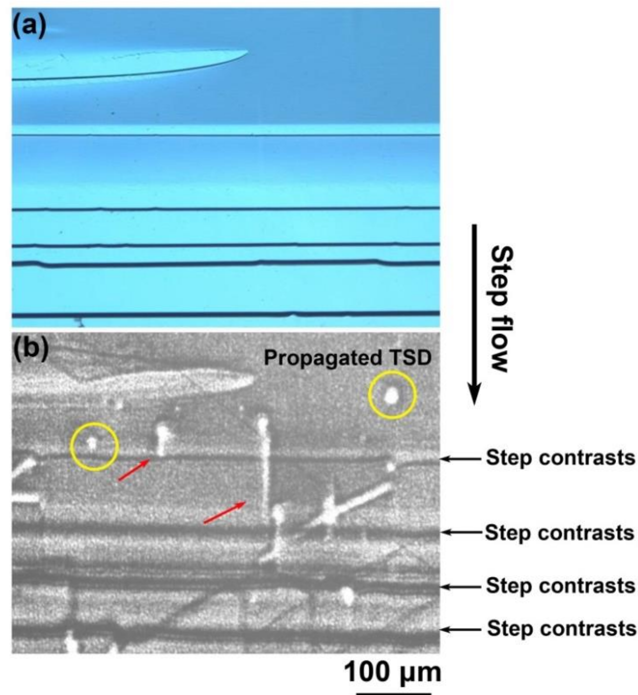


**Fig. 4.6** (a) Normaski image and (b) topographic image at the identical position of grown crystal with Si-5at%Ti solvent. The horizontal black line contrasts indicated by black arrow were contrasts caused by macrosteps. The knife shaped contrasts corresponding to defects on basal plane are indicated by red arrows and yellow circles indicated TSDs propagated from seed crystal in (b).

### 4.3.3 Characterization of step structure

According to literature 4-7 the step height is attributed to the TSD conversion behavior. The step height on crystal grown from Si-5at%Ti solvent is much higher than that on crystal with pure Si. However the conversion ratio on Si face is 100% comparing that on C face crystal with Si-5at%Ti growth is 10%.

Cross-sectional TEM observation was conducted to investigate the step structure on each sample. Steps on Si and C face of crystal grown with pure Si and C face crystal grown from Si-5at%Ti solvent were investigated by STEM.

Fig. 4.7 shows the cross-section TEM images of step structures on (a) C-face grown crystal using pure Si solvent and (b) Si-5at%Ti solvent and (c) Si-face grown crystal with pure Si solvent respectively. It should be noted that the scale bars are different in Fig. 4.7.

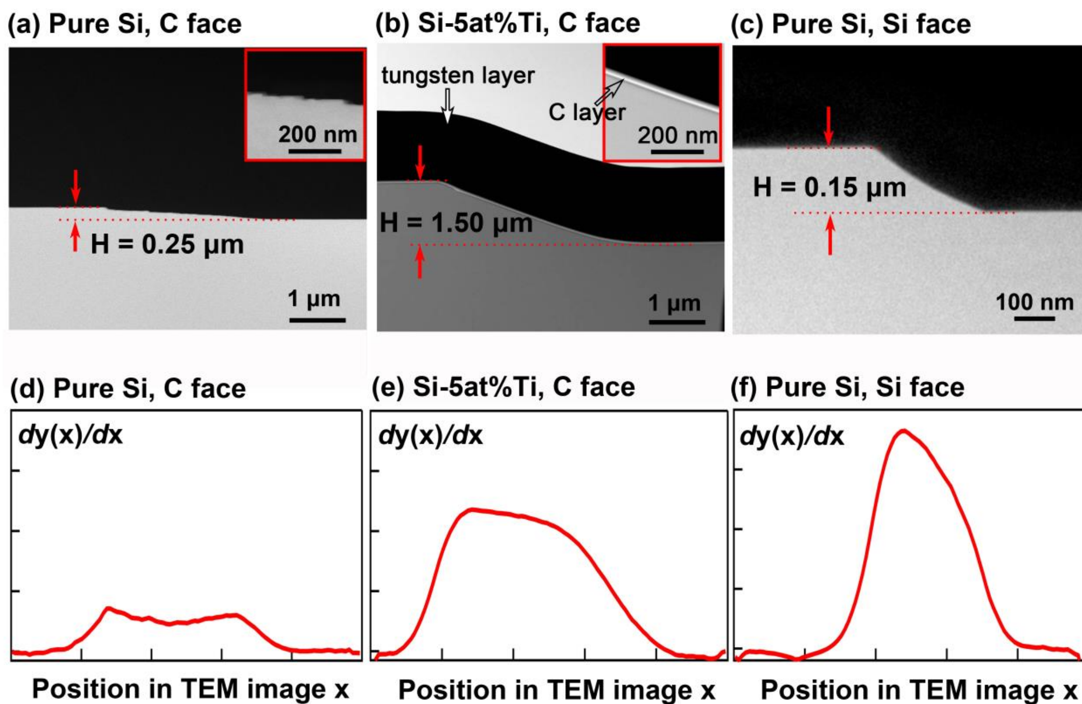


**Fig. 4.7** Cross-section TEM images of step structures on C-face grown crystal using (a) pure Si solvent and (b) Si-5at%Ti solvent and (c) Si-face grown crystal with pure Si solvent; [4-10] (a) and (c) are dark-field images; (b) is bright-field image; Insets show the magnification of corresponding step facet in (a) and (b) respectively. The (x, y(x)) is the coordinate of step profile in each TEM image. (d) (e) (f ) The derivation of step profile corresponding to steps in Fig.3 (a), (b) and (c) respectively. The scales of vertical axis in (d) (e) (f ) is the same.

The step height "H" was evaluated from cross-sectional TEM images of the macrosteps in the manner illustrated in Fig. 4.7 (a). The step height on C face grown crystal without and with 5at%Ti addition solvent was 120 nm and 1.5 μm as shown in Fig. 4.7 (a) and (b) respectively. The step bunching is promoted with the addition of 5at%Ti. In Fig. 4.7 (a) many small steps were found distributed on the facet as shown in the inset. On the contrary, the facet of macrostep in Fig. 4.7 (b) was relatively smooth and no obvious small steps were observed according to the inset. The brighter oblique line in the inset as indicated by the arrow was C coating layer. The results convinced us that the step height was crucial for the TSD conversion ratio which was consistent with the previous results.[4-7] Meanwhile the small step with several nanometer heights distributing on the facet probably also influenced the TSD conversion behavior. On the other hand, the step height was 0.15 μm on Si-face grown crystal by using pure Si solvent.

It is noted that the TSD conversion ratio of C-face grown crystal using Si-5at%Ti solvent was lower than that of Si-face grown crystal from pure Si solvent as mentioned above even though the step height in Fig. 4.7 (b) was ten times higher than that in Fig. 4.7 (c). The result above indicated that besides step height there should be some other factors influenced the TSD conversion behavior. Fig. 4.7 (d) (e) and (f) show the derivation of each step profile corresponding to steps in Fig. 4.7 (a) (b) and (c) respectively. The (x, y(x)) is the coordinate of step profile in each TEM image. The derivation curves could reflect the slope of every spot on each step. The comparison of curves in Fig. 4.7 (d) (e) and (f) demonstrated the slope of step on C-face was gentler than that on Si-face crystal using pure Si solvent. Considering the TSD conversion ratio and step slope of each sample, the results showed that the gentle slope hardly makes TSDs conversion comparing to the steep slope. The gentler slope on C-face crystal may result in the low conversion ratio. Therefore, we concluded that the TSD conversion behavior was not only influenced by the step height but also the slope of step.

### 4.3.4 The effect of step structure on TSD conversion ratio

The discussion has been made from elastic energy aspect for the influence of step angle $\theta$ on TSD conversion behavior. It is well known that a dislocation will proceed into a newly grown layer in a direction that the elastic energy of dislocation per unit growth length is minimum. [4-11] As shown in Fig. 4.8 (a), if the TSD propagates into a newly grown layer with x thick the energy of the newly elongated dislocation line is written as:

$$W_p = \frac{E_t x}{\cos\theta} \tag{3.1}$$

where $E_t$ is the energy per unit length of TSD and $\theta$ is the angle between facet and basal plane. Similarly, according to Fig. 4.8 (b) if TSD convert to the defects on the basal plane the energy of the elongate dislocation line is given as

$$W_c = \frac{E_s x}{\sin\theta} \tag{3.2}$$

where the $E_s$ is the energy per unit length of the SF. By comparing the value of Eqs. (3.1) and (3.2), the TSD conversion behavior could be determined. When the TSD converted, $W_p > W_c$ and there is:

$$\tan\theta > \frac{E_s}{E_t} \tag{3.3}$$

In other words, the value of $\frac{\mathrm{E_s}}{\mathrm{E_t}}$ could be seen as a threshold for TSD conversion. When inequality (3.3) is satisfied by $\theta$ the TSDs would convert to SFs in thermodynamics. The value of $\tan\theta$ increases with $\theta$. Therefore, it is easier for the steep step (large $\theta$) to convert TSDs to SFs.

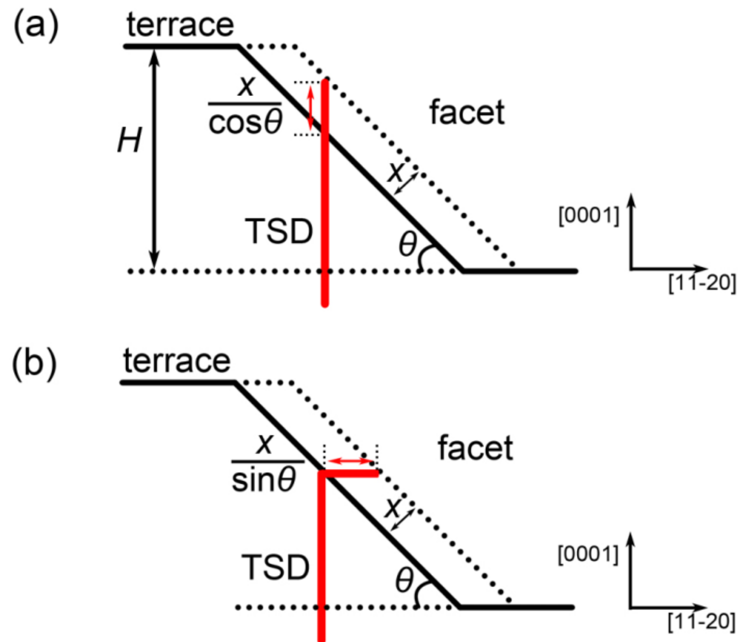


**Fig. 4.8** Illustration of the influence of $\theta$ on the TSD conversion behavior. The $\theta$ is identified as the angle between basal plane and facet. (a) TSD propagates and (b) converted to SF with the $x$ thick newly grown layer.

Taking into account the elastic anisotropy of crystals, the value of $\frac{E_s}{E_t}$ could be calculated.[29] Then, the value of $\theta$ as threshold for TSD conversion could be obtained according to (3). We name this threshold value for TSD conversion as $\theta_{\text{critical}}$. When $\theta$ is greater than $\theta_{\text{critical}}$ TSD conversion happens and vice versa. In 4H-SiC crystals, the value of $\frac{E_s}{E_t}$ is about 1.6 and the $\theta_{\text{critical}}$ is calculated as 58°. However, the calculation threshold $\theta_{\text{critical}}$ (58°) is larger than our experiment result. The inconsistency of the calculation and experiment results indicates that the dissociation of defects on basal plane should be considered. The dissociation of defects on basal plane would decrease the value of $E_s$. The reduction of $E_s$ of defects on basal plane results in the decrease of $\theta_{\text{critical}}$. The dissociation of defects on basal plane could explain our experiment result that TSD conversion happens even though $\theta$ is smaller than 58°.

### 4.3.5 Partial dislocations in crystal grown from Si-5at%Ti solvent

From the topography images of crystal grown from Si-5at%Ti solvent unidentified black line contrasts indicated by red arrow in Fig. 4.9 were often observed under **g**= 11-28 condition. This kind of lines contrasts were not caused by surface morphology by comparing it with the Normaski image. They are rare in samples grown from pure Si solvent. Some of the black line contrasts were pinned by TSD (as indicated by red circles). In order to identify this kind of black line contrasts (indicated by red arrow in Fig. 4.9), topographic contrasts analysis was conducted.

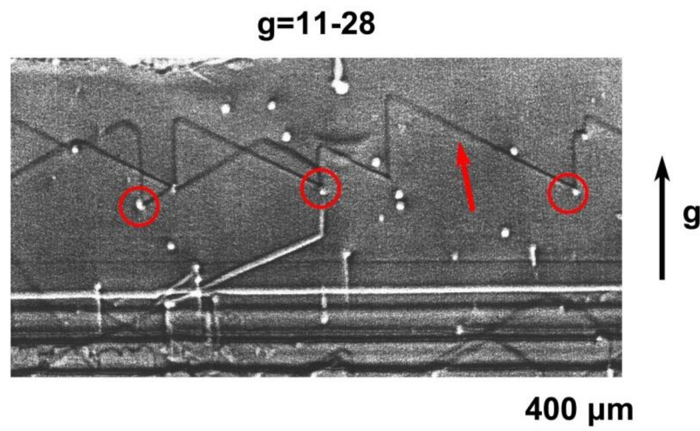


**Fig. 4.9** The in-plane X-ray topography of C-face crystal grown from Si-5at%Ti solvent with **g**=11-28 diffraction condition. The red arrow indicates black zig-zag contrasts which pinned by TSDs indicated by red circles.

Fig. 4.10 shows in-plane X-ray topographic images recorded in grazing incidence (a) **g**= 11-28, (b) **g**= -12-18 and (c) **g**= 2-1-18 directions from C face crystal grown from Si-5at% solvent at the identical position. The black arrows on the right side indicate projected directions of the vectors of incident X-ray on the crystal surface. Black line contrasts indicated by red arrows are visible under all diffraction conditions.

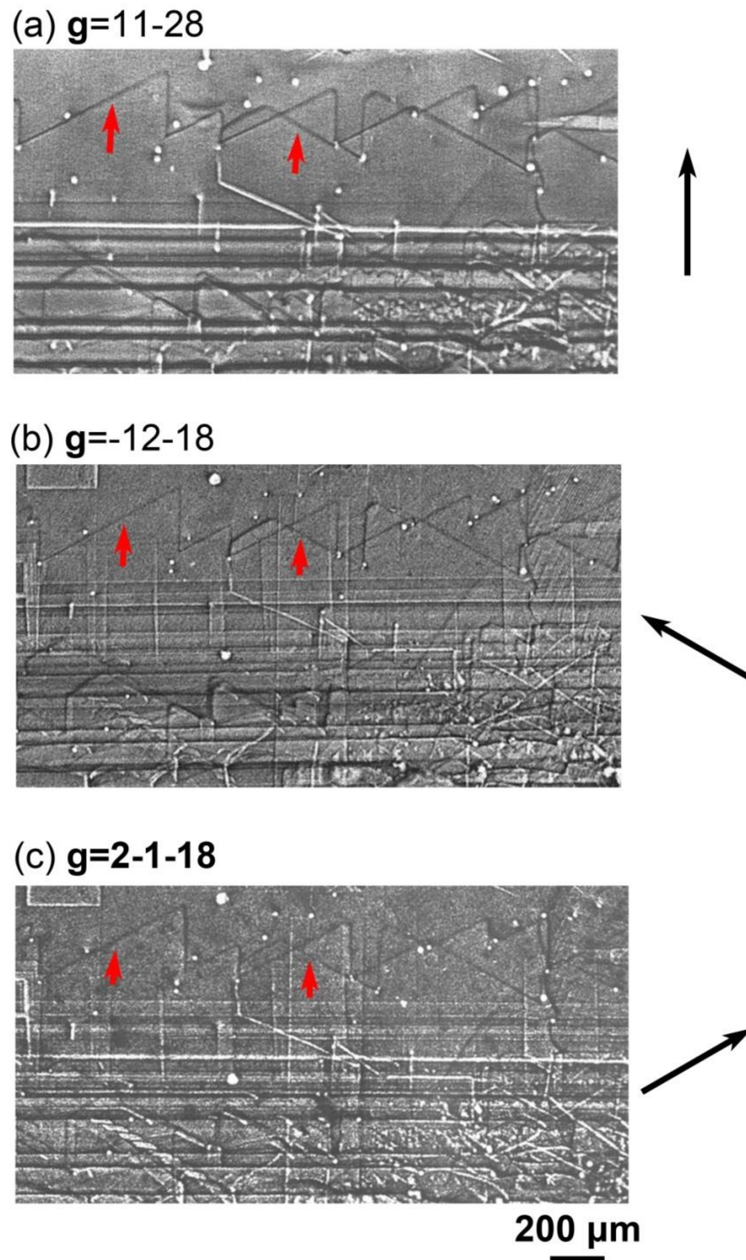


**Fig. 4.10** The in-plane X-ray topography of C-face crystal grown from Si-5at%Ti solvent with (a) **g**=11-28 (b) **g**=-12-18 and (c) **g**=2-1-18 diffraction condition respectively. The black zig-zag contrasts indicated by red arrows are visible under all diffraction condition. The black arrows at right side indicate projected directions of the vectors of incident X-ray on the crystal surface.

Fig. 4.11 shows in-plane X-ray topographic images recorded in grazing incidence (a) **g**= 11-28 and transmission X-ray topographic images recorded under (b) **g**= 1-100 and (c) **g**= 0-110 conditions at the same position with Fig. 4.10. Black arrows at right side indicated projected direction of the vectors of incident X-ray on the crystal surface. Black line contrasts appearing under **g**= 11-28 condition became invisible under transmission condition (**g**= 1-100 and **g**= 0-110). In (b) and (c) gray area circled by red dash lines could be observed. According to the transmission topography contrasts analysis, the gray areas correspond to Shockley stacking faults. Shockley stacking faults have Burgers vectors **b**=1/3<1-100>. Thus the Shockley partial dislocations could be observed under **g=** (1-100).

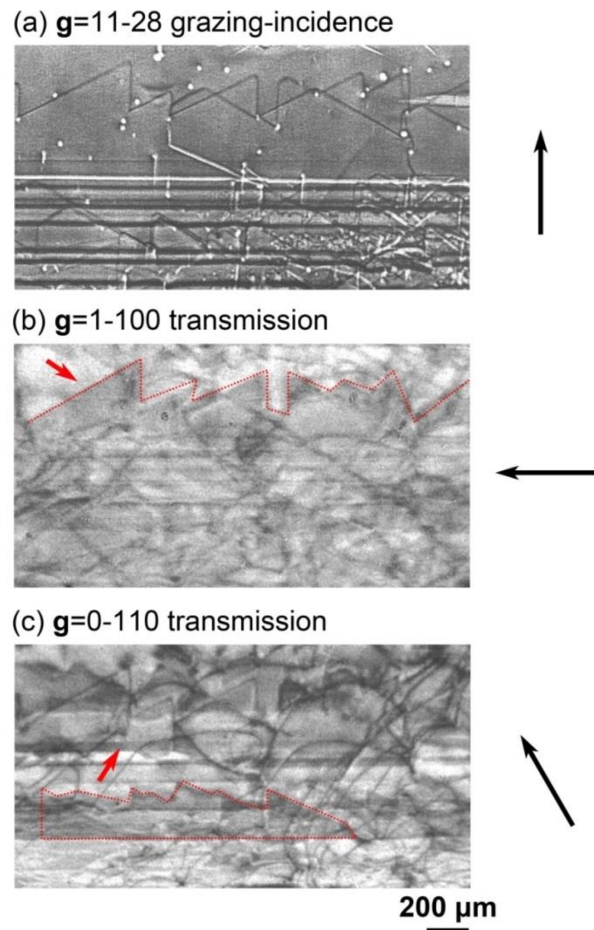


**Fig. 4.11** The in-plane X-ray topography of C-face crystal grown from Si-5at%Ti solvent with (a) **g**=11-28 and (b) **g**=1-100 and (c) **g**=0-110 transmission diffraction condition respectively. The gray area indicated by red arrows and circled by red ash line are Shockley partial dislocations which has Burgers vectors b=1/3<1-100>**.** The black arrows at right side indicate projected directions of the vectors of incident X-ray on the crystal surface.

Fig. 4.12 shows transmission X-ray topographic images recorded under (a) g= 11-20, (b) g= -12-10 and (c) g= 2-1-10 reflection conditions. The visible black line contrasts indicated by red arrows in Fig. 4.12 (a) became invisible under g= -12-10 diffraction direction. That indicated that Burgers vector b of the black line contrasts indicated by red arrows in Fig. 4.12 (a) was b= ± [-1010]. The visible black line contrasts indicated by yellow arrows in Fig. 4.12 (a) became invisible under g= 2-1-10 diffraction direction. That indicated that Burgers vector b of the black line contrasts indicated by yellow arrows in Fig. 4.12 (a) was b= ± [0-110]. They are Shockley partial dislocations with Burgers vector ± [0-110].

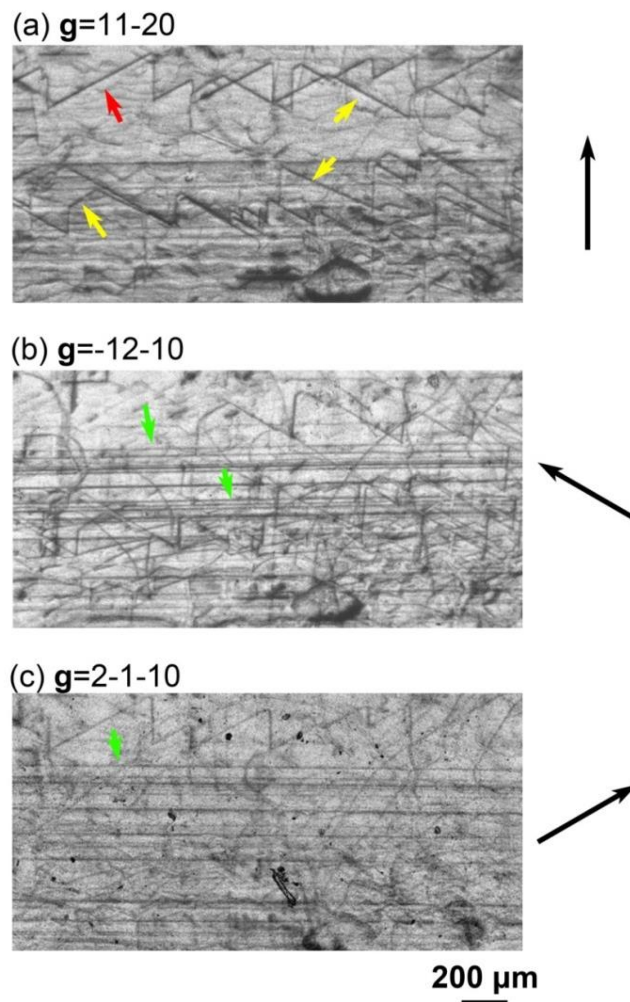


**Fig. 4.12** Transmission X-ray topographic images recorded under (a) g= 11-20, (b) g= -12-10 and (c) g= 2-1-10 reflection conditions. The visible black line contrasts indicated by red arrows in Fig. 4.12 (a) become invisible under g= -12-10 diffraction direction. Black arrows at right side indicated projected direction of the vectors of incident X-ray on the crystal surface.

The formation mechanism of the partial dislocations is still unknown. We assume that the $N_2$ doping from back ground results in the Shockley type stacking fault and partial dislocation since the addition of Ti would increase the $N_2$ doping concentration. The detail would be discussed in section 5.4 in Chapter 5.

## 4.4 Conclusion

In this chapter, the TSD conversion behavior was realized on C face growth by the addition of Ti which had been proved can promote step bunching process. Meanwhile, the effect of step structure on TSD conversion behavior was investigated by cross-sectional TEM observation.

- Macrosteps were observed on crystals grown by Si-5at%Ti solvent.
- TSD converted to defects on basal plane on 4H-SiC C-face crystal grown with Si-5at%Ti solvent during solution growth.
- Synchrotron X-ray topography revealed the TSD conversion ratio increased from 0 to nearly 10% after 5at%Ti addition into the solvent.
- The gentle slope of macrostep was attributed to the low TSD conversion ratio comparing to Si face steps. This result also convinced us that not only step height but also the step shape could affect TSD conversion behavior.
- The realization of TSDs conversion on C face was supposed to be beneficial to the reduction of TSD density on 4H-SiC C face growth.
- Black zig-zag line contrasts were observed on in-plane incidence topography images. By transmission topography contrasts analysis they were proved to be Shockley partial dislocations. The formation mechanism probably related to $N_2$ doping concentration.

# Reference

[4-1] Kojima, K.; Okumura, H.;Kuroda, S.; Arai, K.; Ohi, A.; Akinaga, H., Mater. Sci. Forum 2005, 483, 93-96.

[4-2] Tanaka, Y.; Fukuda, K.; Arai, K.; Kojima, K.; Suzuki, T.; Yatsuo, T., Appl. Phys. Lett. 2004, 84, 1774-1776.

[4-3] Fukuda, K.; Senzaki, J.; Kojima, K.; Suzuki, T., Mater. Sci. Forum 2002, 433, 567-570.

[4-4] Kusunoki, K.; Kamei, K.; Seki, K.; Harada, S. and Ujihara, T., J. Cryst. Growth., 2014, 392, 60-65.

[4-5] Mitani, T.; Komatsu, N.; Takahashi, T.; Kato, T.; Fujii, K.; Ujihara, T.; Matsumoto, Y.; Kurashige, K. and Okumura, H., J., Cryst. Growth., 2014, 401, 681-685.

[4-6] Daikoku, H.; Kado, M.; Seki, A.; Sato, K.; Bessho, T.; Kusunoki, K.; Kaidou, H.; Kishida, Y.; Moriguchi, K. and Kamei, K., Cryst. Growth and Design. 2016, 16, 1256-1260.

[4-7] Yamamoto, Y.; Harada, S.; Seki, K.; Horio, A.; Mitsuhashi, T.; Ujihara, T., Appl. Phys. Express 2012, 5, 115501.

[4-8] Komatsu, N.; Mitani, T.; Okamura, M. Takahashi, T.; Kato, T.; Ujihara, T.; Matsunomto, U.; Kurashige, K. Research on solvent composition for supression of macroscopic surface defects in 4H-SiC solution growth. Presented at the 22nd Meeting on SiC and Related Semiconductors, Saitama Japan, December 9-10, 2013.

[4-9] Harada, S.; Yamamoto, Y.; Seki, K.; Horio, A.; Mitsuhashi, T.; Tagawa, M.; Ujihara, T., APL Mater. 2013, 1, 022109.

[4-10] Harada, S.; Yamamoto, Y.; Xiao, SY.; Tagawa, M.; Ujihara, T., Mater. Sci. Forum. 2014, 778, 67-70.

[4-11] Klapper H.; Küppers, H., Acta Cryst. 1973, A 29, 495-503.

# Chapter 5 Increase TSD conversion ratio on C face growth

## 5.1 Introduction

In order to improve the quality of C face grown crystal, the TSD conversion ratio should be increase. In pure Si solvent, the conversion ratio of TSDs increased with growth thickness in crystal grown from pure Si solvent.[5-1] Therefore it occurred us that the TSDs conversion ratio on C face probably would increase with the growth thickness. Moreover, 3 arms holder is not appropriated for long time growth which means that the seed should be mounted to rod directly. However, the topography images became blurred with the growth time and the attachment way of seed and rod. In this chapter the reason and solutions of blurred topography images was investigated. By conducting several methods to decrease $N_2$ doping concentration from background, clear topography images were obtained. According to the results of topography, the TSD conversion ratio on C face grown crystal with Si-5at%Ti solvent increased from 10% to about 70% with extending growth time.

## 5.2 Experiment

### 5.2.1 Growth

The crystal growth was conducted with induction-heating furnace (NEV-SC35 Nisshin-Giken) as shown in section 2.4.1. Off-axis 4H-SiC (000-1) C-face (10 mm ×10 mm) crystals were used as seeds. The off cut angle was 2°and the off direction was [11-20]. Solvent pure Si and Si-5at%Ti were used as solvents respectively. Graphite crucibles were used to contain the solvent and as carbon source. The temperature at the seed crystal and the bottom of the crucible was measured by thermal couples as described in section 2.4.3. The growth temperature gradient was controlled by the relative position of crucible and the heat coil. The temperature gradient distribution was the same as in Fig. 4.1. Growth experiments were performed by keeping the seed crystal at 2 mm below the solvent surface under a high-purity (>99.9999 vol%) helium gas flow, where the temperature was at 1750 °C and the temperature gradient was about 20 °C /cm. The

growth time was 1 hour and 2 hours. The seed crystal was inserted into the 3 arms holder and attached to the end of a graphite rod. Seed crystal was dipped in solvent in a graphite crucible. The growth procedure is the same as shown in Fig. 4.2. The crucible was maintained at 1750 °C for 1h to homogenize the raw material with the rotation of crucible. The crucible rotation speed was 20rpm. The seed crystal was dipped into the solvent and keep at 10 mm under solvent surface to conduct the melt back process. After 10 min melt back process, the seed crystal would be pulled up to the position 2 mm under the solvent surface. The growth was conducted at 1750°C. The accelerated crucible rotation technique (ACRT) was used. Both the rotation speed of upper rod and crucible was 20rpm. After growth, the upper rod would be pulled up until disconnecting to the solvent. The temperature would decrease to 700°C in 1 hour and then cooling down to room temperature. The residual solvent was removed in HF and $HNO_3$ solution (HF: $HNO_3$ = 1: 2).

### 5.2.2 Characterization

Synchrotron X-ray topography was carried out at the high-resolution X-ray diffraction station BL3C in the Photon Factory at the High-Energy Accelerator Research Organization and BL8S2 in Aichi Synchrotron Radiation Center, Japan. The monochromatic X-ray wavelength was 1.50 Å and the applied **g** vectors were 11-28. The topography images were recorded on Ilford L4 nuclear emulsion plates. Specimens for cross-sectional TEM were prepared by ion milling except the crystal from Si-5at%Ti solvent which is not appropriate for ion milling due to the relatively low step density on the surface. The specimen for cross-sectional TEM observation was fabricated by the Focus Ion Beam (FIB).

## 5.3 Blurred topography images

### 5.3.1 The effect of growth time on topography images on C face growth crystal with Si-5at%Ti solvent

Fig. 5.1 shows the topography images of each sample and corresponding cross-sectional TEM images. Fig. 5.1 (a) shows the topography image of crystal grown from pure Si solvent. The topography image is clear and easy to recognize. The cross-sectional TEM image shows that there is no defect in the crystal. On the other hand, according to Fig. 5.1 (b) and (c), the topography images of crystal grown from

Si-5at%Ti solvent becomse blurred with the growth time. When the growth time achievs to 2h there is no valid information can be identified from the topography image as shown in Fig. 5.1 (c). By cross-sectional TEM observation, SFs corresponding to line contrasts are observed in crystal grown with Si-5at%Ti solvent and the density increases with the growth time. The density of SFs in crystal grown from (d) pure Si (1h), (e) Si-5at%Ti (1h) and (f) Si-5at%Ti (2h) is 0 $cm^{-1}$, $1.41\times10^4$ $cm^{-1}$ and $8.34\times10^4$ $cm^{-1}$. Kusunoki et al. reported that the impurity nitrogen in the Si-Ti solvent would inevitably increase because Ti has a high affinity with nitrogen. They also mention that SFs are abruptly generated above a nitrogen concentration of $3.0\times10^{19}$ $cm^{-3}$.[5-2] The high-magnification TEM observation was conducted to study the SF structure.

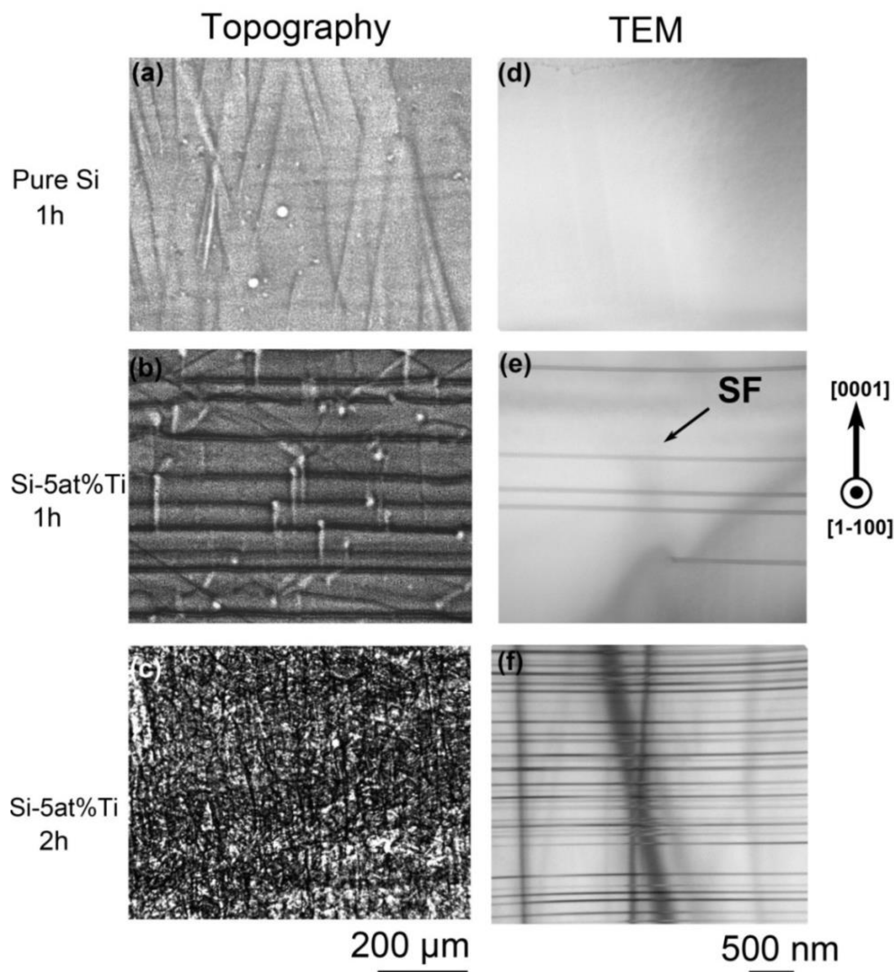


**Fig. 5.1** The in-plane X-ray topography of C-face crystal grown from (a) pure Si for 1h; (b) Si-5at%Ti solvent for 1h and (c) 2h growth with g=11-28 diffraction condition. (d), (e) and (f) are the cross-sectional TEM images corresponding to grown crystals (a) (b) and (c) respectively. The black line contrasts correspond to stacking faults as black arrow indicated.

Fig. 5.2 shows high-resolution cross-sectional TEM image of SFs in crystal grown from Si-5at%Ti solvent. Si atoms are indicated by white spots. The TEM image revealed that SFs generated in crystal grown from Si-5at%Ti solvent are double Shockley-type SFs, which consist of six Si-C bilayers stacked in the cubic sequence. This result is consistent to Ref 5-2.

Moreover, we found that crystal grown with $N_2$ doping also has the similar blurred topography images with that in our case as shown in Fig. 5.3.

Therefore we deduce that the blurred topography images are caused by $N_2$ doping from background. In order to obtain clear topography images, it is necessary to decrease the $N_2$ doping concentration from background. It should be noted that the $N_2$ doping concentration is higher than the detection limit of Raman. Thus we cannot measure the $N_2$ concentration in crystal by Raman.

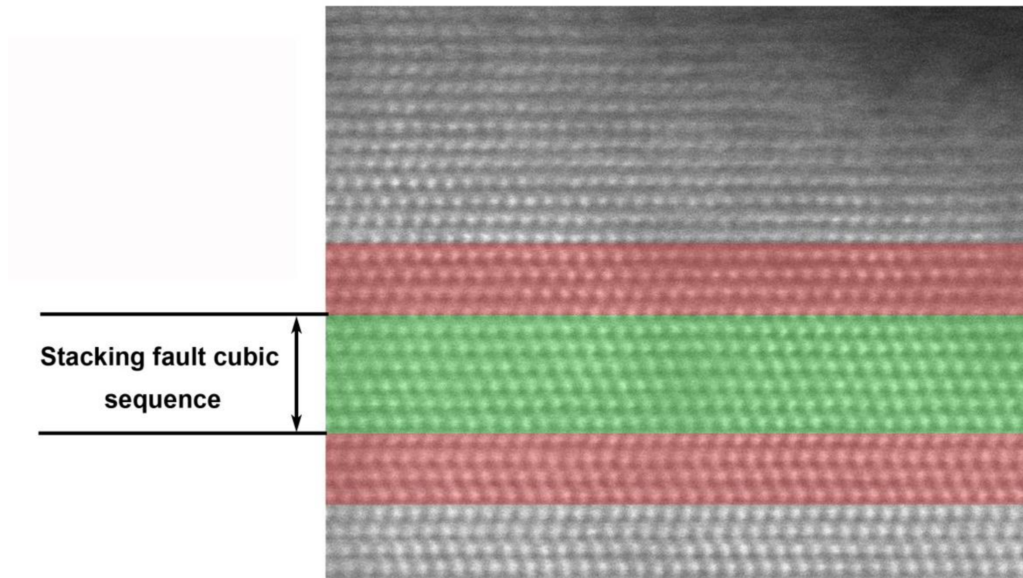


**Fig. 5.2** High-resolution cross-sectional TEM image of SFs in crystal grown from Si-5at%Ti solvent. Si atoms are indicated by white spots. The TEM image revealed that SFs generated in crystal grown from Si-5at%Ti solvent are double Shockley-type SFs, which consist of six Si-C bilayers stacked in the cubic sequence.

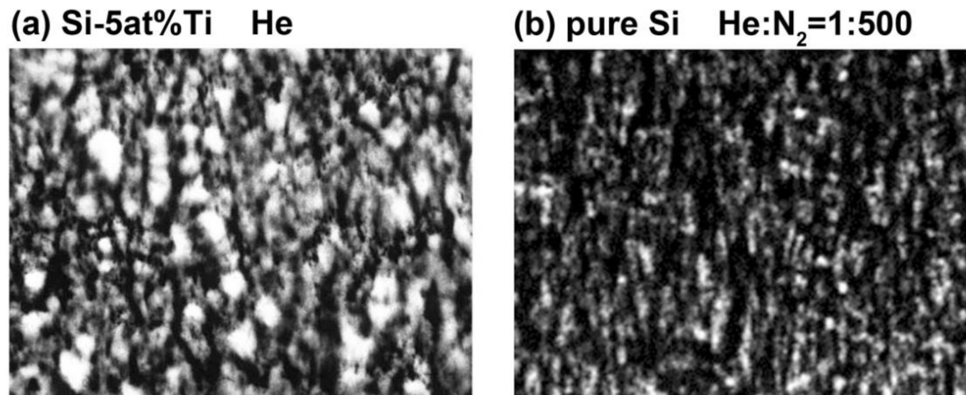


**Fig. 5.3** In-plane X-ray topography images of C-face crystal grown from (a) Si-5at%Ti solvent with He gas flow and (b) pure Si solvent with He: $N_2$ =1: 500 gas flow.

### 5.3.2 The effect of holding seed method on topography images on C face growth crystal with Si-5at%Ti solvent

It is necessary to change the way of holding seed crystals from 3 arms holders to mount them directly on the rod, since 3 arms holders are not suitable for bulk growth. The groove for inserting seed crystal would limit the thickness of grown crystals. However, the topography images become blurred when the way of holding seed crystals changed to attach to rod directly as shown in Fig. 5.4 (b). Both the two samples were grown at the same condition for 1h except the way of holding seed crystals.

According to Fig. 5.4 the topography images became hard to identify when the seed was attached to rod directly. There were many contrasts that cannot be identified and no useful information can be obtained from the topography images. On the other hand, the topography image of crystal growth by using 3 arms holder could be clearly observed. We assumed that the strain on crystal when the seed was attached directly on rod is greater than that when 3 arms holder was used. The strain probably causes the valid topography images. Considering annealing could be helpful to realize strain in crystals, annealing was conducted at 1800 °C for 1h under Ar flow.

Fig. 5.5 shows the Topo images before and after annealing of crystal grown from Si-5at%Ti solvent for (a) 2h and (b) 5h respectively. By comparing the topo images before and after annealing, the effect of annealing was not obvious. The topography images are still blurred. The reason is still open. However considering the seed attachment method changed, the growth condition is needed to be considered again.

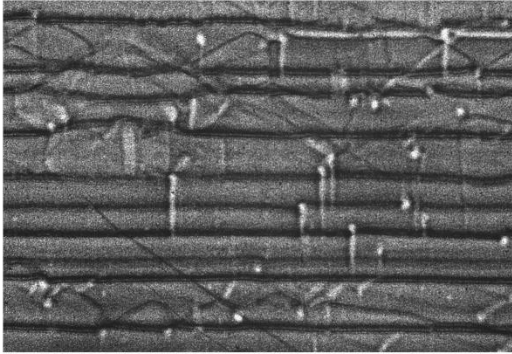


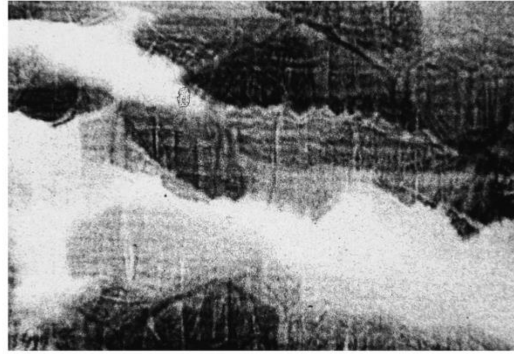


**Fig. 5.4** In-plane X-ray topography images of C-face crystal grown with (a) 3 arms holder and (b) attached seed crystal directly to rod.

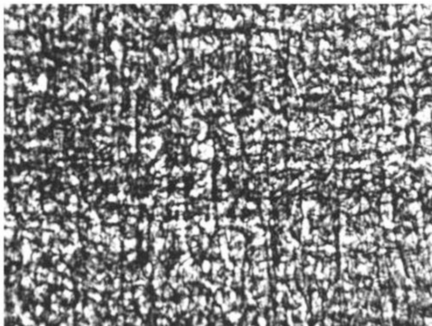

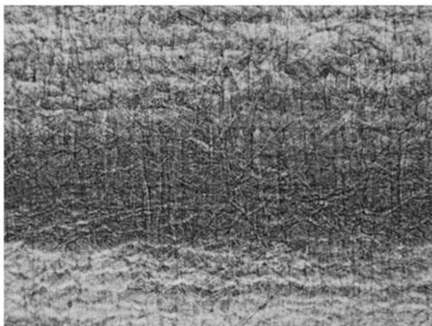


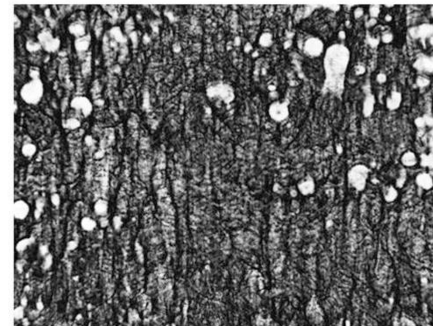

**Fig. 5.5** In-plane X-ray topography images before and after annealing of crystal grown from Si-5at%Ti solvent for (a) 2h and (b) 5h respectively.

## 5.4 Reduction of $N_2$ doping concentration from background during growth

According to our discussion in last section, in order to obtain clear topography images $N_2$ doping concentration from background during growth should be reduced. We took several measures as follow:

① Pre-baking: Pre-vacuum is conducted before growth. The pre-vacuum procedure is as follows. At first, put crucible, raw materials and rods into furnace NEV-SC35 Nisshin-Giken and NEV-SC100XY Nisshin-Giken). Then increase the temperature to 1800 °C and keep it for 1h. It should be noted that during pre-baking the furnace should be kept vacuum.

② High temperature: The growth temperature increase from 1750 °C to 1900 °C. High temperature could prevent polytype change and decrease the $N_2$ doping concentration.[5-2]

③ Zirconium (Zr) or Hafnium (Hf): According to Ellingham diagrams, Zr and Hf which have higher affinity with nitrogen than Ti were putted in outer crucible to absorb $N_2$ during growth. The illustration is shown in Fig. 5.6. In Fig. 5.6 (a), the doulble crucible system (as shown in Fig. 5.6 (a)) is used. Crucible with solvent is putted in the center of outer crucible. The bottom of crucible well matches the susceptor at the center of outer crucible. Zr of Hf is located in the outer crucible. Fig. 5.6 (b) is the illustration of the inside vies of furnace with double crucible system.

④ No He flow: The atmosphere changed from He flow to just filling He before growth.

Since the growth system is different before in this section, the appropriate temperature distribution should be investigated again. The changed growth condition is shown in Fig. 5.7. The method to hold the seed crystal was changed from 3 arms holders to mount them directly to the rods. The induction-heating furnace (NEV-SC100XY Nisshin-Giken) was used to conduct the growth experiment. The growth time extended from 1h to 5h and the temperature distribution at the growth position is changed from 20 °C to 5 °C. The growth rate increased from about 9 μm/h to about 13μm/h. The growth thickness of crystals in section 5.4 was about 65μm.

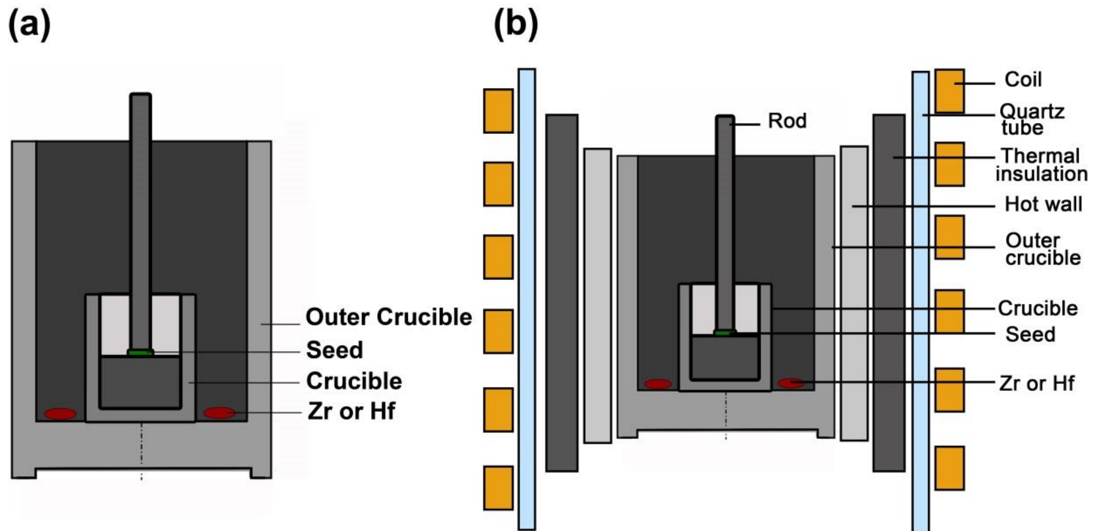


**Fig. 5.6** The illustration of (a) double crucible system which used to decrease the $N_2$ doping concentration and (b) the illustration of the inside view of furnace with double crucible system.

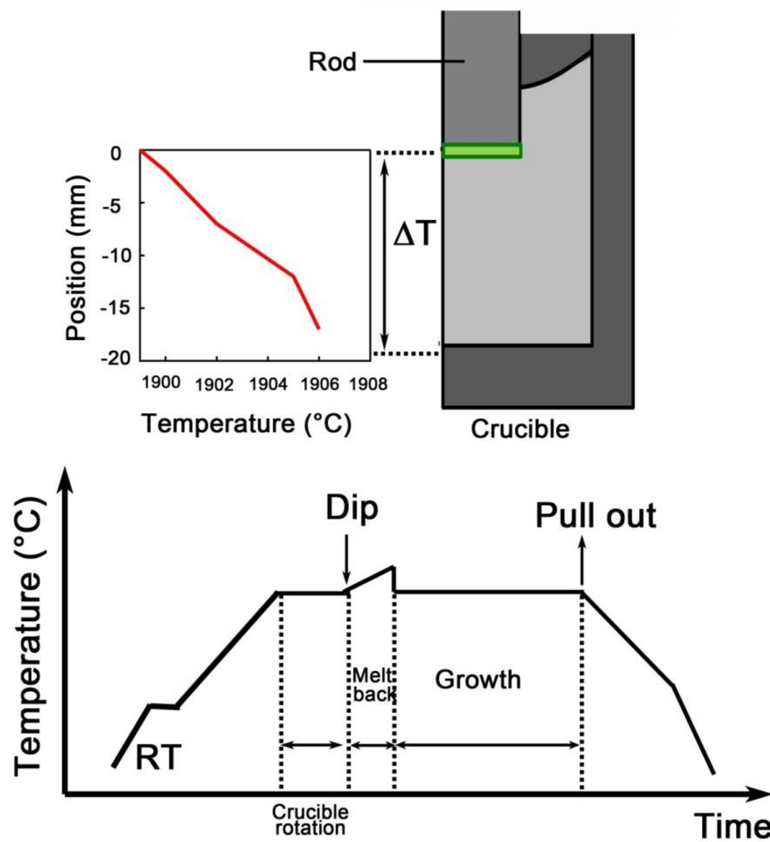


**Fig. 5.7** The illustration of (a) temperature distribution and (b) the growth procedure of experiments in this section.

Finally, after adjusting the growth condition (temperature, temperature gradient and so on) topography images were taken (a) before and (b) after growth of the crystal as shown in Fig. 5.8. Fig. 5.8 (c) shows surface morphology at the identical position of topography images. Clear topography images indicated that the measures we took were effective for reducing $N_2$ doping concentration. In Fig. 5.8 (b) defects could be well identified and TSDs conversion could be clearly observed. By a comparison of Fig. 5.8 (a) and (b) the TSDs conversion behavior was confirmed. TSD in red circle converted to TSDs after growth. On the other hand, TSDs in yellow circles propagated from seed crystal. Moreover, the surface morphology became different from Fig. 4.3 (c) in chapter 4 since the adjustment of growth condition. The step wandered instead of appearing horizontal lines. Many small steps with several μm width were observed distributed all over the terrace as show in Fig. 5.8 (d) which is the magnification image of terrace.

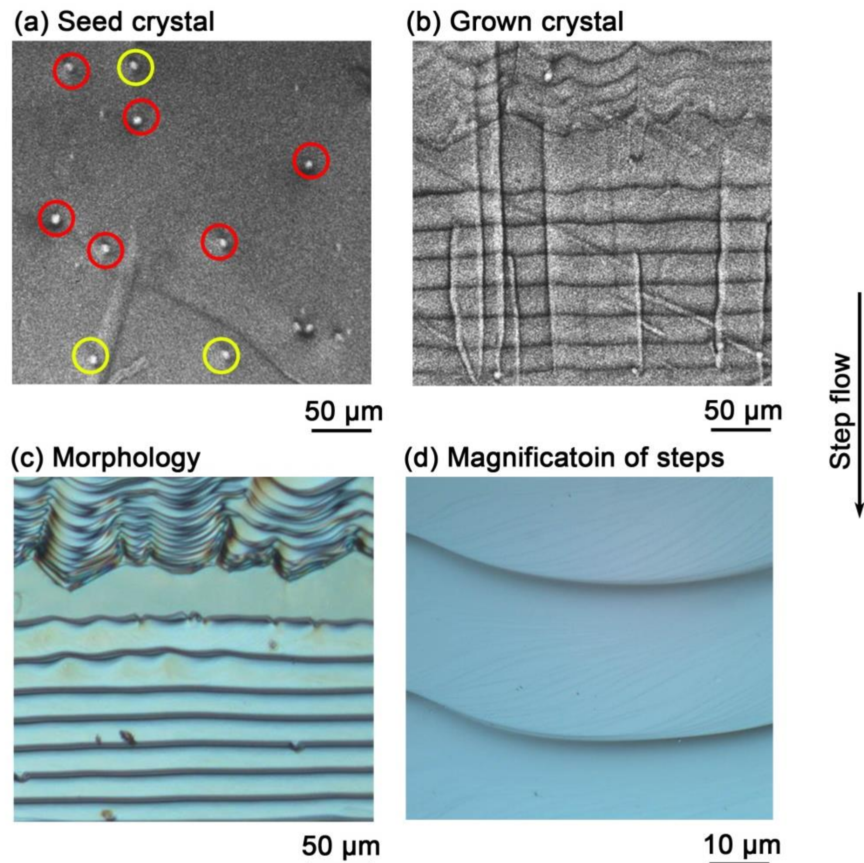


**Fig. 5.8** The in-plane topography images (a) before and (b) after growth with Si-5at%Ti solvent. Red circles indicated TSDs in seed crystals which converted to defects on basal plane. Yellow circles indicated TSDs propagated to grown crystal. (c) The morphology surface at the identical position with (a) and (b). (d) The magnification image of step.

## 5.5 The TSD conversion ratio dependence of growth thickness

We counted the numbers of TSDs in seed crystal and converted TSDs in grown crystal. The TSD conversion ratio increased from 10% (1h growth) to 70% (5h growth) as shown in Fig. 5.9. Fig. 5.9 revealed the TSD conversion dependence of crystal growth thickness. TSD conversion ratio increased with the growth thickness.

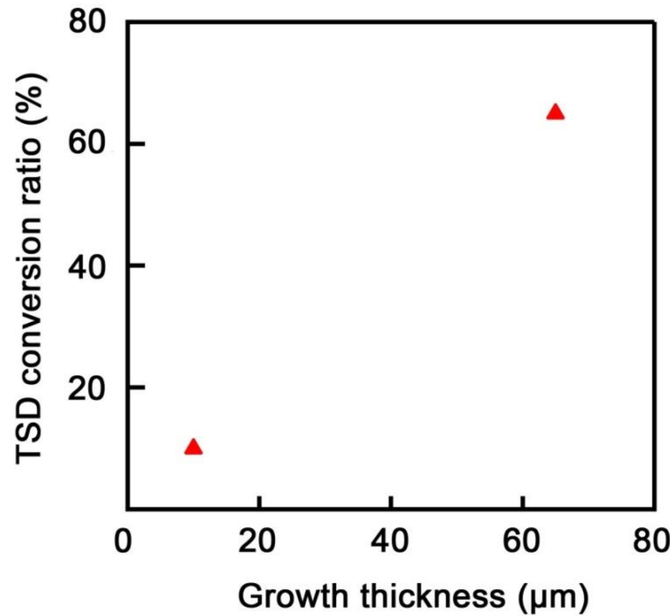


**Fig. 5.9** TSD conversion ratio dependence of growth thickness.

## 5.6 Conclusion

In this chapter, TSD conversion ratio on C face growth is raised by increasing growth thickness.

- $N_2$ doping from background probably results in the blurred topography images which hamper the characterization of defects behavior.
- Pre-baking, high temperature growth without He flow and Zr or Hf are used to obtain clear topography images for grown crystal.
- The TSD conversion ratio on C face growth increase from 10% to about 70% with the growth thickness increased from 10 μm to 65 μm.

# Reference

[5-1] Harada, S.; Yamamoto, Y.; Seki, K.; Horio, A.; Mitsuhashi, T.; Tagwa, M. and Ujihara, T., APL Mater., 2013, 1, 022109.

[5-2] Kusunoki, K.; Kamei, K.; Seki, K.; Harada, S. and Ujihara, T., J. Cryst. Growth., 2014, 392, 60-65.

# Chapter 6 High quality 4H-SiC C face grown crystals

## 6.1 Introduction

Bulk growth is crucial for obtainment of high quality 4H-SiC crystal. Because during solution growth, the defects on basal plane could be excluded from crystal unless grown crystal reached certain thickness. Moreover, in order to satisfy the application for semiconductor power devices, SiC bulk growth is also essential. In chapter 4 we mention that C face growth has great advantages in polytype stability than Si face growth. Meanwhile, the properties of C face grown crystal are different from Si face in many aspects. [6-1, 2, 3] Therefore it is important to realize high-quality SiC bulk growth on C face.

In chapter 4 and 5, we have realized the TSD conversion behavior on C face growth by using Si-5at%Ti solvent. However there are two weak points for C face bulk growth by using this method we should notice. One is the low growth rate. The growth rate for C face grown crystal is about 10-14 μm/h which is not good for the bulk growth. The other weak point is that giant macrosteps formed during growth. The giant macrosteps are undesirable for polytype stability and trench elimination. In another word, macrosteps is desirable for converting TSD but undesirable when conducting long time growth. That indicates that macrosteps should be controlled.

In this chapter, we realized the high-quality 4H-SiC C face growth by utilizing two-step growth (morphology control). Chrome (Cr) was used to increase growth rate and aluminum (Al) were used to keep smooth growth surface and prevent trench formation.

## 6.2 Two-step growth

The conception of two-step growth is illustrated as Fig. 6.1. The purpose for the first step growth with Si-5at%Ti solvent is to make TSDs in seed crystal convert to defects on basal plane. In order to prevent the low growth rate and rough morphology, the grown crystals obtained from the first step growth are used as substrate for the second step growth. Si-39at%Cr-2at%Al solvent is used as solvent in the second time growth. The purpose for the second step growth is to increase the growth speed by the addition of Cr and keep smooth surface morphology by Al addition. The defects on basal plane

would be excluded with the growth process. High quality SiC grown crystal on C face would be obtained.

**(a) Seed crystal**

**(b) 1st step growth (Si-5at% solvent)**
**Purpose: Realize TSDs conversion on C face grwoth**

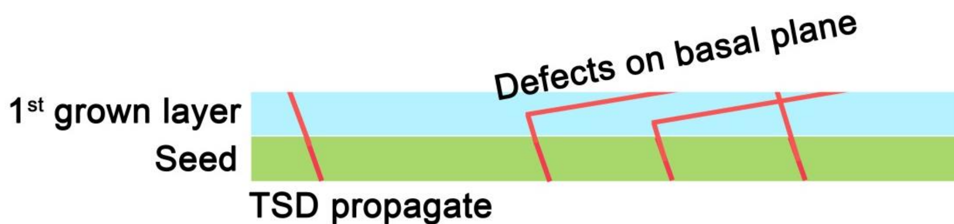


**(c) 2nd step growth (Si-39at%Cr-2at%Al solvent)**
**Purpose 1: Increase growth speed (Cr addition)**
**Purpose 2: Keep smooth morphology (Al addtion)**

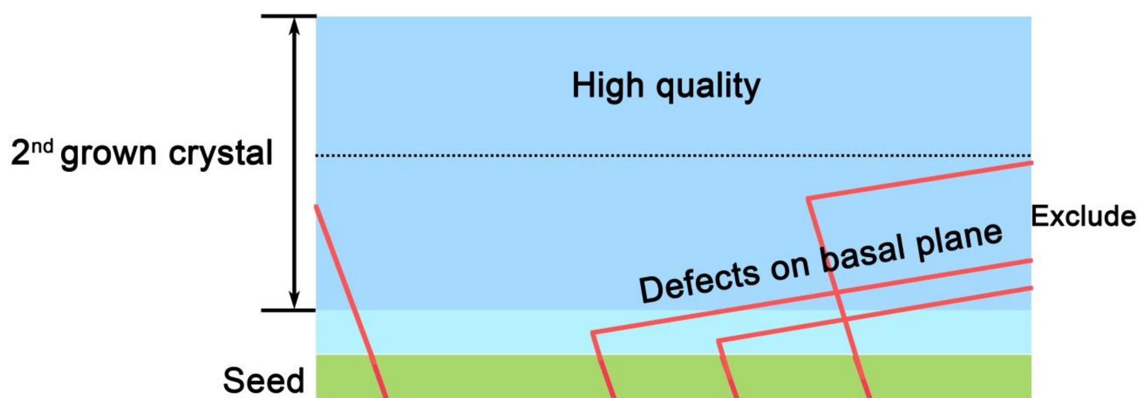


**Fig. 6.1** The conception of two-step growth method. (a) Seed crystal with TSDs (b) The purpose for the first step growth with Si-5at%Ti solvent is to make TSDs in seed crystal convert to defects on basal plane. (b) In order to prevent the low growth rate and rough morphology, the grown crystals obtained from the first step growth were used as substrate for the second step growth. Si-39at%Cr-2at%Al solvent was used as solvent in the second time growth. The

purpose for the second step growth is to increase the growth speed by the addition of Cr and keep smooth surface morphology by Al addition. The defects on basal plane would be excluded with the growth process and high quality SiC grown crystal on C face would be obtained.

## 6.3 Experiment

### 6.3.1 Growth

#### 6.3.1.1 First step growth

The first step growth was conducted in induction-heating furnace (NEV-SC100XY Nisshin-Giken) with double crucible setting as Fig. 5.6 (b). Off-axis 4H-SiC (000-1) C-face (10 mm ×10 mm) crystals were used as seeds. The off angle was 2°and the off direction was [11-20]. Solvent Si-5at%Ti was used. A graphite crucible was used to contain the solvent and as carbon source. The temperature at the seed crystal and the bottom of the crucible was measured by thermal couples. The growth temperature gradient was controlled by the relative position of crucible and the heat coil. The temperature distribution in crucible and growth procedure was the same with Fig. 5.7. Before growth, pre-baking was conducted as described in section 5.4. Growth experiments were performed by keeping the seed crystal at 2 mm below the solvent surface under a high-purity (>99.9999 vol%) helium gas without flow, where the temperature was at 1900 °C and the temperature gradient is about 5 °C /cm. The growth time is 5h. The seed crystal was attached to the end of a graphite rod.

Before the second step growth, surface morphology was observed and in-plane incident topography images were recorded before and after growth to reveal the defects behavior. The rod should be removed from the crystal. The grown crystal should be cleaned as section 2.4.4.1 described.

#### 6.3.1.2 Second step growth

The second step growth was conducted in induction-heating furnace (NEV-SC35 Nisshin-Giken). The seed crystals were crystals grown from Si-5at%Ti solvent in the first step growth. The seed crystals were attached directly on the graphite rods. Si-39at%Cr-2at%Al was used as solvent in the second time growth. The growth temperature was 1850 °C and temperature gradient was 6 °C/cm as shown in Fig. 6.2. The growth procedure was illustrated as Fig. 6.3. Growth experiments were performed

by keeping the seed crystal at 2 mm below the solvent surface under a high-purity (>99.9999 vol%) helium gas flow.

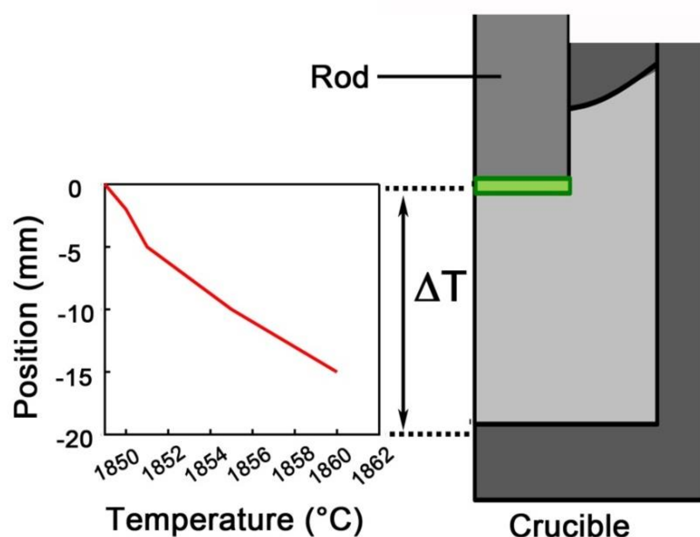


**Fig. 6.2** The illustration of temperature distribution of experiments in this section.

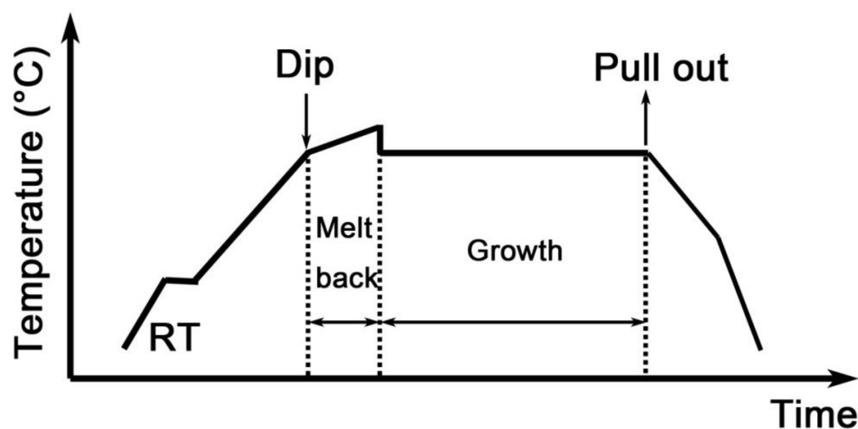


**Fig.6.3** The growth procedure of experiment in this section**.**

## 6.3.2 Characterization

In-plane incident topography images were recorded before and after growth to reveal the defects behavior. Synchrotron X-ray topography was carried out at the BL8S1 in Aichi Synchrotron Radiation Center, Japan. The monochromatic X-ray wavelength was 1.50 Å and the applied **g** vectors were 11-28. The topography images were recorded on Ilford L4 nuclear emulsion plates. Polytype was determined by Raman spectra. The

morphology of grown crystal morphology was observed by DIC microscopy.

## 6.4 Results and discussion

### 6.4.1 Grown crystal after the first step growth

The surface morphology and in-plane incident x-ray topography image of grown crystal are shown in Fig. 6.4 (a) and (b) respectively. The grown morphology is consistent to the results in section 5.5. Macrosteps were distributed nearly all the grown crystal surface. The mark of residual Si solvent was indicated in Fig. 6.4 (a) and (b).

Magnification images of topography images before and after growth and morphology at the identical position are shown in Fig. 6.5 (a), (b) and (c) respectively. TSDs in seed crystal indicated by red triangles convert to knife shape contrasts corresponding to defects on basal plane. We calculate the TSD conversion ratio and it is about 70%. Comparing Fig. 6.5 (b) and (c) the horizontal wave lines are caused by the macosteps.

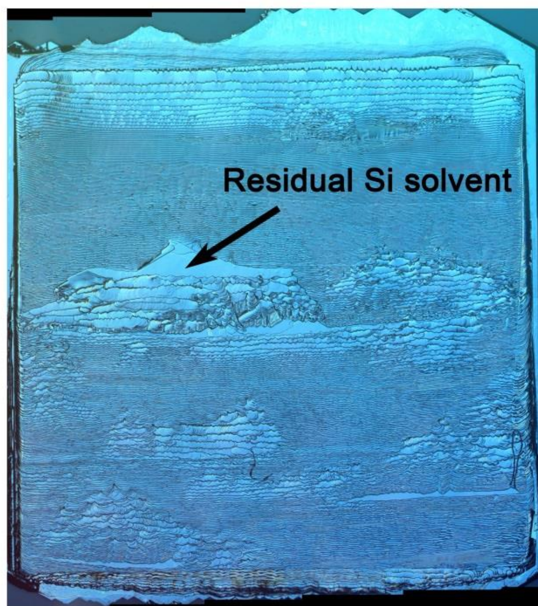


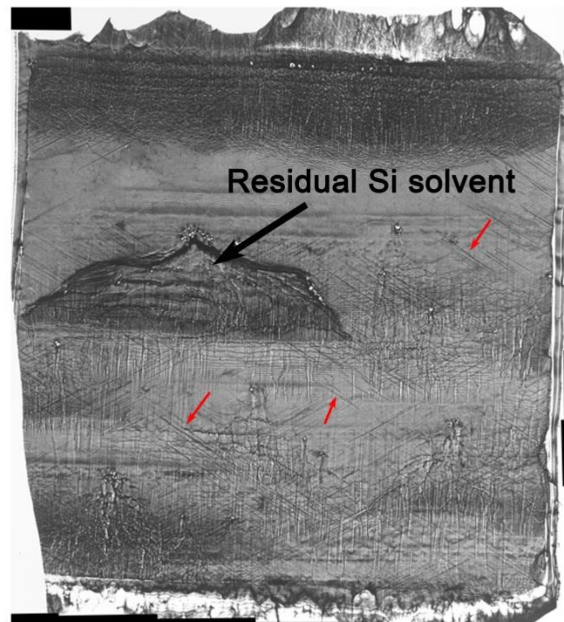


**Fig. 6.4** The mapping of Nomarski image and in-plane topography image of grown crystal grown from Si-5at%Ti solvent for the first time growth. Oblique black line contrasts are indicated by red arrows.

The magnification of We also noted that there are many oblique black line contrasts from the topography images as red arrows indicated in Fig. 6.4 (b). In order to investigate this kind of black line contrasts topography contrast analysis was conducted under **g**= 11-28 and **g**= 1-108 respectively. The results are shown in Fig. 6.6 (a) and (b). The oblique line contrasts in Fig. 6.6 (a) indicated by red arrows become invisible under the **g**= 1-108 diffraction condition. Therefore the Burgers vector of defects corresponding to the black line contrasts is parallel to ± [11-20] direction. The angle between the line contrasts and step flow probably caused by the $N_2$ doping from back ground which is consistent to ref. 6-4. Moreover the knife shaped contrasts corresponding to defects on basal plane are still visible as white arrow indicated in Fig. 6.6 (a).

(a) Seed crystal

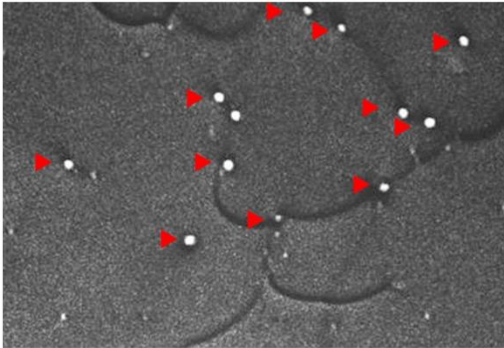

(b) Grown crystal

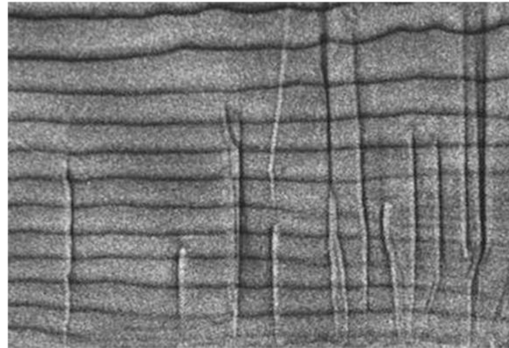

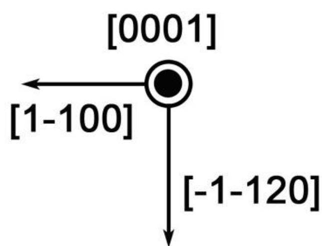


(c) Normaski image

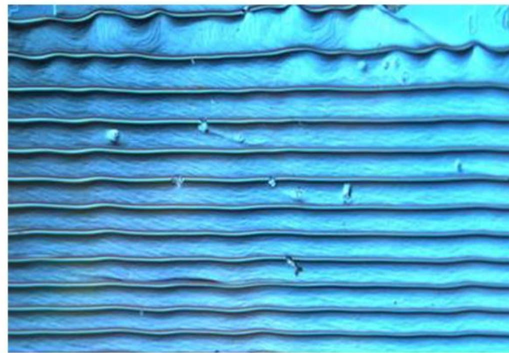


**Fig. 6.5** Magnification images of topography images before and after growth and morphology at the identical position are shown in Fig. 6.5 (a), (b) and (c) respectively. Red triangles indicate TSDs converting to defects on basal plane.

(a) **g**= 11-28

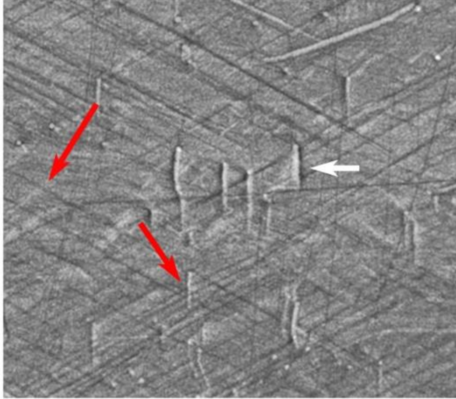

(b) **g**= 1-108

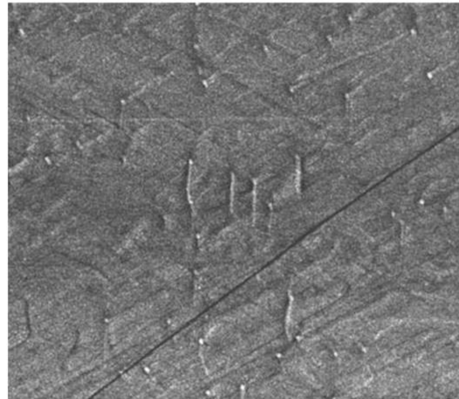

**Fig. 6.6** X-ray topography images of the grown crystal C-face with Si-5at%Ti solvent taken at Bragg conditions: (a) g= 11-28 and (b) 1-108. The oblique line contrasts in Fig. 6.6 (a) indicated by red arrows become invisible under the g= 1-108 diffraction condition.

## 6.4.2 Grown crystal after the second step growth

As described in section 6.3.1.2 the seed crystal of second step growth is the grown crystal from the first step growth. The growth condition and procedure is described in section 6.3.1.2. The grown crystal morphology and topography image at the identical position are shown in Fig. 6.7 (a) and (b) respectively. In Fig. 6.7 (a), no TSD could be observed. TSD density in the grown crystal after the second step growth is below 8 $cm^{-2}$ which is three orders of magnitude lower than that of seed crystal (2000 $cm^{-2}$). Therefore, the reduction of TSD on C-face growth is achieved. Meanwhile BPDs are rarely observed in grown crystal. High quality 4H-SiC grown crystal is obtained by two-step growth. The investigated area was 12 $mm^2$. From Fig. 6.7 (b), steps could be observed which indicated that the step flow growth proceeded.

By a comparison of the topography image and Nomarski image, the black spot in Fig. 6.7 (a) is caused by the morphology. On the other hand, small white circle contrasts are often observed from the topography images as indicated by red arrows in Fig. 6.7 (a). That probably cause by the mismatch between the seed crystal and the grown crystal. The seed crystal is n-type since the use of Ti addition would increase the $N_2$ doping concentration during the first step growth. However, the addition of Al in the solvent during the second time growth results in P-type doping. Therefore, TEDs could still be observed in the grown crystal. How to realize the mismatch phenomenon between n-type seed crystal and p-type grown crystal and realize the reduction of TEDs would be

our future work.

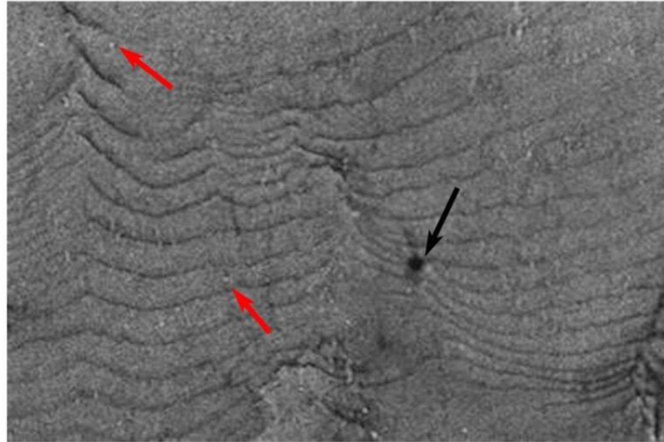


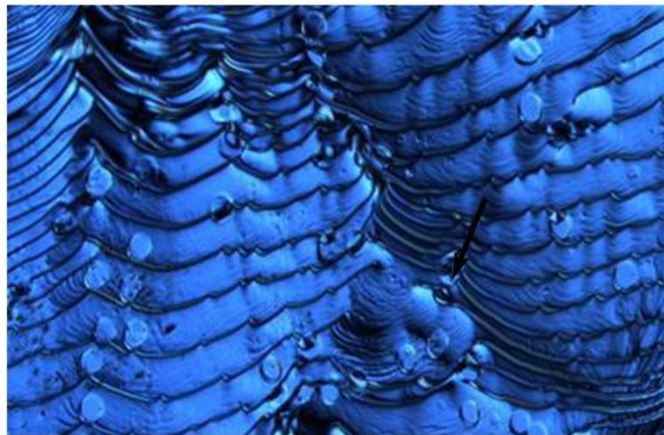


**Fig. 6.7** (a) In-plane topography image and (b) morphology image of the second step grown crystal at the identical position. The red arrow indicates TED and the black arrow indicates morphology (b) causing black spot contrast in (a).

## 6.5 Conclusion

In this chapter, in order to overcome the weak point of growth with Si-5at%Ti solvent and obtain high quality SiC C face grown crystals, two-step growth with different solvent was proposed.

- High quality 4H-SiC C-face grown crystal was realized by controlling morphology (two-step growth with different solvent).

- The TSD density of C-face grown crystal decreased from 2000/cm$^2$ to below 8/cm$^2$ which is three orders of magnitude lower than that of seed crystal.

# Reference


[6-1] Matsunami, H.; Kimoto, T., Mater. Sci. Eng. R. 1997, 20, 125-166.

[6-2] Nakamura, D.; Gunjishima, I.; Yamaguchi, S.; Ito, T; Okamoto, A.; Kondo, H.; Onda, S.; Takatori, K., Nature 2004, 430, 1009-1012.

[6-3] Miyazawa, T.; Tsuchida, H., ECS J. Solid State Sci. Technol. 2013, 2, N3036-N3040.

[6-4] Kusunoki, K.; Kamei, K.; Seki, K.; Harada, S. and Ujihara, T., J. Cryst. Growth., 2014, 392, 60-65.

# Chapter 7 Conclusion

In this study, we discovered a new kind of unidentified defects during SiC Si face growth. The defects exhibit V-shaped contrasts from in-plane topography images. Their apexes located at the upper-step site and V opened up toward down-step direction. According to topography contrasts analysis, the V-shaped defects were identified as pairs of defects generated simultaneously with Burgers vectors parallel to [11-20] direction during growth. TEM observation confirmed the topography conclusion. The V-shaped defects generation has been discussed. 2D nucleation was attributed to the formation of V-shaped defects. On Si-face growth, 2D islands were often observed than C face. We concluded C face growth could restrain the generation of V-shaped defects.

In order to obtain high-quality SiC crystals on C face growth. We investigated solvent component for the formation of macrosteps. TSD conversion ratio increased from 0 to 70% by the addition of 5%Ti addition. The influence factors of TSD conversion were discussed from energy aspect. We concluded that the conversion ratio was affected not only by step height but also the angle between facet and basal plane. The steep steps resulted in higher TSD conversion ratio.

In order to overcome shortcomings of growth with Si-5at%Ti solvent (low growth rate and poor morphology), two-steps growth (controlling surface morphology during growth) was conducted. Si-5at%Ti solvent was used to convert TSDs in seed crystals. The grown crystals obtained from the first step growth were used as seed crystal for the second step growth. We used Si-39at%Cr-2at%A solvent to increase growth rate and keep surface morphology smooth. Finally, TSD density decreased from 2000/cm$^2$ to below 8/cm$^2$ by utilizing two-step growth.

Here, the knowledge obtained in each chapter is summarized below. The Chapter 1 provided the background of this study. In Chapter 2, details of experiments and characterization were introduced.

In Chapter 3, a kind of newly generated defects during Si face SiC growth is studied and their generation mechanism was discussed.

- The V-shaped defects are comprised of a pair of dislocations on the basal plane. Each pair of dislocations with the opposite Burgers vector parallel to [11-20] direction is proved to generate simultaneously.
- They are different from the V-shaped defects in CVD growth.

- A mechanism of generation of the V-shaped defects is proposed on a basis of the 2D nucleation islands on terrace.
- So far they only can be observed on Si face grown crystal during solution growth. Therefore, the C face growth can restrain the generation of V-shaped defects.

In chapter 4, the TSD conversion behavior is realized on C face growth by the addition of Ti which have been proved can promote step bunching process. Meanwhile, the effect of step structure on TSD conversion behavior is investigated by cross-sectional TEM observation.

- Macrosteps are observed on crystals grown by Si-5at%Ti solvent.
- TSDs convert to defects on basal plane on 4H-SiC C-face crystals grown with Si-5at%Ti solvent during solution growth.
- Synchrotron X-ray topography reveals the TSDs conversion ratio increases from 0 to nearly 10% after 5at%Ti addition into the solvent.
- The gentle slope of macrosteps is attributed to the low TSD conversion ratio comparing to Si face steps. This result also convinces us that not only step height but also the step shape could affect TSD conversion behavior.
- The realization of TSDs conversion on C face is supposed to be beneficial to the reduction of TSD density on 4H-SiC C face growth.
- Black zig-zag line contrasts are observed on in-plane incidence topography images. By transmission topography contrasts analysis they are proved to be Shockley partial dislocations. The formation mechanism probably relates to $N_2$ doping concentration.

In chapter 5, TSD conversion ratio on C face growth is raised by increasing growth thickness.

- $N_2$ doping from background probably results in the blurred topography images which hampered the characterization of defects behavior.
- Pre-baking, high temperature growth without flow and Zr or Hf is used to obtain clear topography images for grown crystal.
- The TSD conversion ratio on C face growth increases from 10% to about 70% with the growth thickness increased from 10 μm to 65 μm.

In Chapter 6, in order to overcome the weak point of growth with Si-5at%Ti solvent and obtain high quality SiC C face grown crystals, two-step growth with different

solvent is proposed.

- High quality 4H-SiC C-face grown crystal is realized by controlling morphology (two-step growth with different solvent).
- The TSD density of C-face grown crystal decreases from 2000/cm$^2$ to below 8/cm$^2$ which is three orders of magnitude lower than that of seed crystal.

## Acknowledgment

First I would like to give my deep and sincere gratitude to Prof. Toru Ujihara, my Ph. D. advisor, for providing me this opportunity to work in the SiC crystal growth and characterization field. His wide knowledge and helpful guidance have been of great value for me. His understanding, encouragement and personal guidance have provided an excellent basis for my Ph. D. research. Without a doubt his contributions have helped me to obtain my Ph. D. degree.

Second, I owe to thank Dr. Shunta Harada for his instructive discussions regarding both experiment and theory. I also thank him for his help in doing the topography and TEM experiments.

I would like to thank Prof. Noritaka Usami, Prof. Toshiuki Koyama, Prof. Kenji Shiraishi and Prof. Kenji Ueda for being my dissertation committee members and their valuable advice.

I would also like to thank my colleagues: Dr. Kenta Aoyagi, Dr. Kenta Murayama, Dr. Ichihashi Fumiaki, Dr. Takumi Isogai, Dr. Tomonori Umezaki, Dr. Can Zhu. Dr. Ryota, Murai, Dr. Kenji Hanada, Dr. Daishi Shiojiri, Yukihisa Takeuchi, Tomoko Shoji, Yukako Iwase, Kenji Shibata, Sangil Lee, Daiki Koike, Mingyu Chen, Masashi Nagaya, Kenji Nishitani, Takuya Muto, Shota Yamamoto, Kohei Ishikawa, Sakiko Nagada, Ayano Nakamura, Natsumi Hara, Shota Watanabe, Zhenjiang Wang, Masaki Matsumoto, Shizuki Okajima, Yoske Tsunooka, Xingyu Dong, Makoto Hayashi, Tsukasa Hori, Naoya, Yoshida, Penglei Chen, Akito Inoue, Hayato Sumi, Hiroshi Saitou, Gouki Hatasa, Nobuhiko Kokubo, Fumihiro Fujie, Xingbo Liu.

I would like to thank the funding and chance offered by CSC from Chinese government. It makes possible for me to study abroad.

At last I would like to thank my family. Without them, I would not have been able to study in Japan and obtain so many results.

# Presented papers

## Paper

[1] **Shiyu Xiao**, Natsumi Hara. Shunta Harada, Kenta Murayama, Kenta Aoyagi, Takenobu Sakai and Toru Ujihara, "Research on solvent composition for different surface morphology on C face during 4H-SiC solution growth", Mater. Sci. Forum, 821-823, pp. 39-42, 2015.

[2] **Shiyu Xiao,** Shunta Harada, Kenta Murayama, Toru. Ujihara, "Characterization of V-shaped defects formed during the 4H-SiC solution growth by transmission electron microscopy and X-ray topography analysis", Crystal Growth & Design (*Accepted*) 2016.

[3] **Shiyu Xiao,** Shunta Harada, Kenta Murayama, Miho, Tagawa, Toru. Ujihara, "Conversion behavior of threading screw dislocations on C face with different surface morphology during 4H-SiC solution growth", Crystal Growth & Design (*Submitted*).

## Meeting and poster

[1] **SY. Xiao**, N. Hara, S. Harada, T. Sakai, T. Ujihara, “Threading screw dislocations conversion behavior on C face with different surface morphology during 4H-SiC solution growth”, European Conference on Silicon Carbide and Related Materials 2014 (ECSCRM2014), TuP-16, Grenoble, France, September, 2014

[2] **肖 世玉**, 原 奈津美, 原田 俊太, 宇治原 徹, “The investigation of step structure with different TSDs conversion behavior during 4H-SiC solution growth”, 2014 年秋第 75 回秋季応用物理学関係連合講演会, 17A-a17-3, 北海道大学, 2014 年 9 月.

[3] **Shiyu Xiao**, Shunta Harada, Toru Ujihara, “Investigation of defects generated during solution growth of silicon carbide”, International Union of Materials Research Societies (IUMRS), A11-O29-015, Fukuoka University, August, 2014.

[4] **<u>肖 世玉</u>**, 原 奈津美, 原田 俊太, 宇治原 徹, “SiC 溶液法 C 面成長における TSD 変換”, 2014 年春 第 61 回春季応用物理学関係連合講演会, 17p-E5-9, 青山学院, 2014 年 3 月.

[5] **<u>肖 世玉</u>**, 原田 俊太, 宇治原 徹, “Observation of newly generated basal plane dislocations during solution growth of 4H-SiC”, 第 22 回 SiC 及び関連ワイドギャップ半導体講演会, A-8, 埼玉会館, 2013 年 12 月.

[6] **<u>Shiyu Xiao</u>**, Shunta Harada, Toru Ujihara, “Observation of Basal Plane Dislocations Generated during Solution Growth in 4H-Silicon Carbide”, International Symposium on EcoTopia Science '13 (ISETS), Nagoya University, November, 2013.

[7] **<u>肖 世玉</u>**, 朱 燦, 原田 俊太, 宇治原 徹, “SiC 溶液成長過程における基底面転位の形成”, 2013 年秋第 74 回秋季応用物理学関係連合講演会, 18a-B3-3, 同志社大学, 2013 年 9 月.